AEROSPIKE ROCKET MOTOR STRUCTURAL WEBBING

A Thesis

presented to

the Faculty of California Polytechnic State University,

San Luis Obispo

In Partial Fulfillment

of the Requirements for the Degree

Master of Science in Mechanical Engineering

by

Andrew Brock

February 2015

COMMITTEE MEMBERSHIP

TITLE:	Aerospike Rocket Motor Structural Webbing
AUTHOR:	Andrew Brock
DATE SUBMITTED:	February 2015
COMMITTEE CHAIR:	Dr. William R. Murray Professor of Mechanical Engineering
COMMITTEE MEMBER:	Dr. J. Scott Patton Associate Professor of Mechanical Engineering
COMMITTEE MEMBER:	Dr. Joseph Mello, Professor of Mechanical Engineering

ABSTRACT

Aerospike Rocket Motor Structural Webbing

Andrew Brock

A labscale hybrid rocket motor test stand has been developed for research at Cal Poly. The primary focus of research using this rig has been the development of regenerative cooling techniques using nitrous oxide as coolant and oxidizer, as well as validation of technologies relating to the annular aerospike nozzle. In order to prevent undesirable deflection of the cantilevered spike, a structural stiffening web, referred to as "The Spider," is proposed. The Spider resembles a three-spoked wheel, with the aerospike held by the inner hub and the chamber walls abutting the outer radius.

The Spider, placed upstream of the nozzle, is subject to thermal loads due to radiation and convection from the gases, and conduction from the outer annulus, as well as mechanical loads from thermal expansion and gas flow. Simulation tools are developed in three phases to produce an accurate model of the spatio-temporal distribution of these loads.

A prototype of the Spider instrumented with thermocouple probes is designed, manufactured, and subjected to a series of hotfire tests. Results from three experimental runs are gathered and compared to simulated results. Good agreement is shown for the most part between the two datasets, with a single noticeable discrepancy for one measured temperature location. The high fidelity in the mean rate of temperature change for all stations indicates that the convective heat load is accurately modeled.

The simulation results, confirmed by experiment, indicate that in order for the Spider to survive in the steady-state during an actual burn, an active cooling strategy is necessary. Two actively cooled concept designs are presented and discussed, and future avenues of research are suggested.

ACKNOWLEDGMENTS

It is beyond the capacity of these few words to fully express my sincere and honest thanks to the myriad friends who made possible this odyssey, but I shall do my best. To Dr. Murray, who led me to the water, to Jim Gerhardt, who presented me the keys to the kingdom of hardware, to Dr. Patton, who passed down the Great Works of fluid dynamicists past, and to Dr. Mello, who provided valuable material insight. To my family, for whom I am never sufficiently grateful. And, most importantly, to Chris D'Elia, whose tireless insistence on accepting nothing less than perfection has opened more doors than I can possibly count.

TABLE OF CONTENTS

Page

LIST OF TABLES

Table Page

LIST OF FIGURES

Figure Page

I. INTRODUCTION

Hybrid rocket motors make use of a solid fuel grain with a liquid or gaseous oxidizer. As opposed to chemically noxious and extremely dangerous hypergolic propellants such as N_2O_4, hybrid rocket fuel is typically easy to manufacture, chemically inert, safe to store, and often less costly than its solid or liquid counterparts[1]. The fuel is commonly made from polymers such as acrylic, Hydroxyl-Terminated PolyButadiene (HTPB), or paraffin wax. Combustion of hybrid rocket motors requires the propellants to be combined and ignited by an external source such as a sparkplug or plasma igniter, which means that it is possible to deactivate and reignite the motor while in flight; the flowrate of the oxidizer can also be modulated to control the combustion ratio as desired[2].

The aerospike nozzle is a class of altitude compensating nozzle that is designed to perform with optimal efficiency at a wider range of altitudes than traditional bell nozzles[3]. The spike, which has a specially designed contour, sits in the throat of the nozzle and modulates the expansion of the exhaust such that the change in ambient pressure does not effect a thrust reduction as would be observed for an uncompensated nozzle.

A labscale hybrid rocket motor test stand has been developed for research at Cal Poly. The primary focus of research using the hybrid rocket test rig has been the development of regenerative cooling techniques using nitrous oxide (N_2O) as both coolant and oxidizer[4] [5]. Previous work has produced the detail design of a reusable cooled aerospike and nozzle, which make use of phase-change cooling to maintain acceptable device surface temperatures, reducing the likelihood of erosion or ablation and extending part life significantly[6]. Using N_2O as a coolant is advantageous for several reasons. N_2O can function as both coolant and oxidizer, making recirculation possible, and the high vapor pressure of gaseous N_2O removes the need for external pumps. Properly designing regenerative cooling systems requires in-depth understanding

of the two-phase nitrous oxide flow and heat load to the actively cooled device; underestimating the cooling capacity of a particular configuration can overheat the fluid and cause a catastrophic runaway exothermic decomposition. Characterization of the cooling capacity of two-phase flow of nitrous oxide is the subject of several related Cal Poly projects that have yet to bear a fully validated model.

In addition to developing cooling techniques, prior research at Cal Poly has focused on developing and validating technologies related to the aerospike nozzle[7][8][9]. The spike is subject to high thermal loads that necessitate an active cooling strategy. Because the spike is typically cantilevered out from the main support (15" in the Cal Poly labscale hybrid rocket motor), the potential for undesirable deflection and vibration exists. In order to prevent undesirable deflection, a structural stiffening member, henceforth referred to interchangeably as the "structural webbing" or "The Spider," is proposed. The Spider resembles a three-spoked wheel, with the aerospike held by the inner hub and the chamber walls abutting the outer radius.

The Spider, placed upstream of the nozzle, is subject to thermal loads due to radiation and convection from the gases[10][11], and conduction from the outer annulus, as well as mechanical loads from thermal expansion and gas flow. In order to prevent overheating in burns of useful duration, the Spider will need to be actively cooled, likely using the same two-phase flow strategy developed for the regeneratively cooled spike. This project seeks to provide simulation tools to characterize these loads, empirically validate the simulations, and provide a concept design for an actively cooled Spider. Completion of the cooled Spider detail design will require a validated model of two-phase N_2O flow, and is thus not yet feasible.

Determination of the observed structural and thermal loads is split into two separate problems: that of conduction within the webbing, and that of heat transfer from hot gases at the webbing

surface. For a “solid” webbing design—that is, one without any internal passages or other features—the conduction problem can be modeled with a high degree of accuracy. More complex geometries necessitate more in-depth modeling and the use of simulation tools, but results can still be obtained with great accuracy, even in the face of nonlinear phenomena such as surface-to-surface contact and temperature dependent material properties. The problem of heat transfer from the gases, however, is far less easily solved, and is the focus of most of the following modeling efforts.

The physics of gas flow in hybrid rockets involves a number of fluid, thermal, and chemical phenomena. The flow regime at the webbing consists of multiple species[12], has a transient period before it reaches steady-state, is fully turbulent, and is typically subsonic, though depending on the permitted flow area, (specifically the constriction ratio) transonic flow may occur. Heat transfer occurs in the form of convection and radiation. The driving chemical phenomenon is fuel-rich incomplete combustion. Auxiliary phenomena include the regression of the fuel grain[13][14], vibration of the assembly due to internal oscillations that may result in combustion instabilities[15] and geometric changes in the test stand due to thermal expansion.
To fully analyze and simulate the complete spectrum of multiphysics is beyond the scope of this project. The phenomena which bear the most significance on the induced heat load must thusly be identified and appropriately simplified. For this analysis, thermal expansion and vibration of the test rig are assumed negligible.

Though all of the hot-fire tests are performed fuel-rich, the model does not simulate this incomplete combustion, instead relying on a stoichiometric approximation with a correction factor based on the ratio of observed to theoretical specific impulse. In order to determine the properties of the gases, the NASA Chemical Equilibrium with Applications (NASA-CEA)[16] program is used in conjunction with the data gathered on a range of tests. In addition, the lack of

an experimental method for examining the relative concentrations of the products of combustion makes multispecies flow simulation difficult. Assuming fully-efficient turbulent mixing allows the gas to be modeled as homogenous, and the associated multispecies dynamics are accordingly assumed to have a negligible effect on the surface heat transfer.

Though the flow exists in a transient state for a finite period of time, there are several barriers to producing a time-variant simulation. The variation of the most relevant boundary conditions and material properties is not directly measured, and their time variation is difficult to estimate. The foremost source of uncertainty on this front stems from the manually-controlled ignition sequence. As transient flow effects are most dominant at the start of the test, accurately modeling these effects becomes difficult and largely unverifiable. The time to steady state is thusly assumed to be small in comparison to the duration of the test. The properties from the NASA-CEA analysis are assumed to be constant, as are the boundary conditions and flow simulation results. Though the flow dynamics are only modeled in the steady state, the conduction is modeled as time variant with constant boundary conditions.

Convection is assumed to be the dominating mode of heat transfer. Extant literature[1] and analyses previously performed at Cal Poly[4] suggest that for Oxidizer to Fuel (O/F) ratios typically used for testfires on the labscale rocket motor, radiative heat transfer observed by the nozzle is several orders of magnitude below the convective load. Radiation to the webbing is, by extension, also assumed negligible. The convection problem consists of determining the surface heat transfer coefficient, also known as the film or convection coefficient, the surface temperature, and the fluid temperature[17][18][19]. As the surface temperature is determined through the conduction analysis and the fluid temperature is a function of the flow dynamics and properties given by NASA-CEA, most effort is spent determining the spatial variation of the convection coefficient on the surface of the webbing.

The flow kinematics are of middling complexity, consisting of an upstream stagnation point[20], the development of thermal and momentum boundary layers over the surface of the webbing[21], separation, and downstream vortices in the wake, all fully turbulent and in three dimensions. Compressibility comes into play for certain designs, especially those with greater flow restriction, and therefore increased Mach numbers. Fortunately, these conditions are common enough that a wide range of solutions, both analytical and semi-empirical, have been developed. Additionally, the advent of Computational Fluid Dynamics (CFD) tools has provided a method for direct simulation of the Reynolds-Averaged Navier-Stokes equation and the energy equation even for complex geometric cases. CFD tools make possible the complete modeling of the exact geometry of interest [22].

This analysis takes place in three phases. Phase 1, presented in Section III, makes use of semi-empirical correlations and an integral analysis to develop a 1-D model, implemented in MATLAB, from which the spatial distribution of film coefficients is calculated and exported to a defeatured 3-D webbing model in ABAQUS, wherein the transient conduction analysis is conducted.

In Phase 2, presented in Section IV, ANSYS FLUENT is used to perform a 2-D CFD analysis of the flow over the cross-section of a single spoke of the webbing, assuming that the presence of the upstream stagnation point makes this particular section of the geometry most likely to overheat, allowing for neglect of the rest of the structure. The resulting heat transfer coefficients are compared against the results of Phase 1, then mapped to a homogenous cross-section using the PDE toolbox in MATLAB in order to analyze the conduction. Several geometries are compared, and the qualitative results are used to aid in experimental design.

In Phase 3, presented in Section V, the 2-D FLUENT analysis is extended to a cyclically symmetric fully 3-D simulation. The fully-featured model of the webbing iteration used for empirical validation is then simulated in ANSYS FEA with the applied heat load calculated in FLUENT. This model phase also accounts for the insulating effect of soot deposits that result from fuel-rich and incomplete combustion, as well as the thermal contact resistance of the interface between the temperature probes and the body of the experimental prototype.

In Section VI, the design, manufacture, and testing of an experimental prototype is presented. The experimental prototype features an iteration of the webbing with embedded thermocouples that allow for active temperature measurement during a hotfire test. Data gathered using this prototype is used to validate the simulated model.

In Section VII , the results of the hotfire tests are presented and compared to the simulation. Discrepancies and their sources are identified and discussed, and recommendations for further testing are made.

In Section VIII, a concept design for an actively cooled spider is detailed, providing a method for designing and constructing internal recirculating cooling passages using manufacturing techniques available through the Cal Poly facilities. This design approach avoids the need for additive or hybrid manufacturing methods as might otherwise be used to produce such passages.

In the final section, Section IX, concluding remarks are made and avenues for future research are suggested.

II. BACKGROUND

The primary purpose of the fluid dynamics simulation detailed in this report is to determine the spatial variation of the convective heat load on the structural webbing. The thermodynamic principle that describes the rate of heat transfer from a fluid to a surface is Newton's Law of Cooling:

$$q" = h(T_\infty - T_s)$$

where $q"$ is the surface heat flux, h is the film coefficient, T_∞ is the fluid total temperature, and T_s is the surface temperature. The film coefficient is a function of a wide variety of variables, making its determination difficult to perform solely through analysis. A number of application-specific semi-empirical correlations have been developed to simplify this estimation. The correlation used most commonly to determine heat flux in rocket nozzles is provided by Bartz[23] in axisymmetric form:

$$h_g = \frac{C}{D^{0.2}}\left(\frac{D_*}{r_c}\right)^{0.1}\left(\frac{\mu_0^{0.2} c_p}{\mathrm{Pr}^{0.6}}\right)(\rho U)^{0.8}\left[\left(\frac{\rho_{ref}}{\rho}\right)^{0.8}\left(\frac{\mu_{ref}}{\mu_0}\right)^{0.2}\right]$$

where h_g is the film coefficient, C is a dimensionless parameter typically set to 0.026, D is the nozzle diameter at the axial point of interest, D_* is the throat diameter, r_c is the radius of curvature at the throat, μ is the kinematic viscosity, c_p is the specific heat at constant pressure, Pr is the Prandtl number, ρ is the fluid density, and U is fluid mean velocity. The $_o$ and $_{ref}$ subscripts refer to properties evaluated at stagnation and reference conditions, respectively. The reference temperature at which $_{ref}$ properties are evaluated, also called the film temperature, is defined as the arithmetic mean temperature of the wall temperature and the local free-stream static temperature.

Prior work at Cal Poly has focused on the development of aerospike thrust vectoring and regenerative structure cooling using N_2O as both a coolant and an oxidizer. The structural webbing was first conceptually presented by Browning[7] in 2007, where it was envisioned as a graphite insert between the liner of the nozzle and the outer lining of the fuel grain chamber.

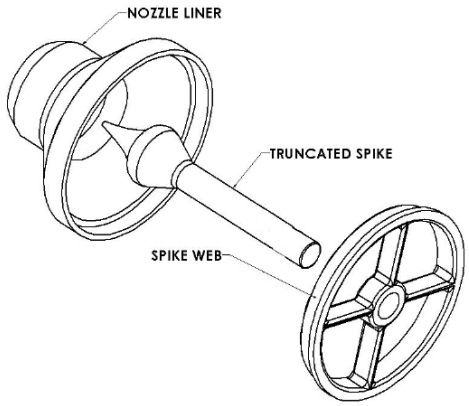

Figure 1: The Webbing, as presented by Browning

The analysis performed by Browning only considered static structural loads, and will thus be neglected for purposes of the work contained herein. Grieb[6] performed a thermomechanical finite element analysis on an actively cooled aerospike, making use of CFD analysis provided by Rolling Hills Research Corporation[24][25][26] to estimate the convective heat load on the spike surface and a simplified model of the coolant. Efforts to model the behavior of two-phase nitrous-oxide flow for application as a regenerative coolant began with the work of Nelson[4], and are still the ongoing subject of a parallel set of projects.

III. MODEL PHASE 1

The closed-form heat transfer correlation provided by Bartz is most frequently used to estimate convective heat load on nozzle surfaces. As the structural webbing is directly in the exhaust flow, this correlation does not provide a realistic approximation of the loading.

The flow, which is presumed turbulent and incompressible, is modeled as consisting of two distinct regions: an upstream stagnation point, where the flow impinges the structure and heat transfer is highest, and an intermediate region along the length of the structure where the boundary layer develops. The stagnation point and trailing edge film coefficients are approximated using semi-empirical correlations, and linked using an integral solver that describes the growth of the thermal and momentum boundary layers.

The stagnation point heat transfer is calculated using the incompressible correlation given by White[27]. Though flow in the nozzle is subject to compressibility effects, it is assumed that the structural webbing is far upstream of the throat and does not constrict the flow in any considerable way, meaning that in this domain the Mach number will be low and compressibility effects will be negligible.

A method for calculating the growth of boundary layers in rocket nozzles is presented by Bartz[28]. The equations are modified as shown in Appendix A to convert from the axisymmetric to the cyclically symmetric case. The primary change is that the local radius variable is removed and replaced with a local cross-sectional area variable in the governing equation. The remaining relations are re-derived following the substitution of variables.

The Bartz Solver

The boundary layer integral solver, referred to as the Bartz Solver, is implemented in MATLAB, the code for which is available in Appendix B(i-iii). Initial solver validation was performed using the flow parameters provided by Bartz. In order to better approximate the actual observed flow regime, flow parameters were gleaned from data collected during previously performed hotfire tests on the Cal Poly hybrid rocket test stand. These data, which were processed using NASA-CEA calculator, are organized and accessed using the CEASE .mfile, which is available in Appendix B(vi).

Flow parameters are selected for the burn with what would presumably be the highest magnitude of heat transfer to the webbing, were it present for said burn, assuming a stoichiometric combustion ratio and equilibrium reactions. In the context of the experiments performed for validation, these assumptions are inaccurate, but highly conservative. The selected run, number 86, was performed using HTPB fuel, as opposed to the acrylic used in the webbing experiments. HTPB tends to produce significantly hotter exhaust than does acrylic, and the actual combustion ratio tends to be fuel-rich, which results in a cooler burn than a stoichiometric ratio. These flow parameters are used in the first two phases of the model, and are indicative of the environment the experimental apparatus is designed to survive. This highly conservative case was selected based on the reasoning that the experimental burns will likely be significantly cooler than predicted, providing a comfortable safety factor for the length of burn the apparatus can withstand without suffering permanent damage in the form of erosion, ablation, or melting.

The Bartz Solver consists of several subroutines. First, the flow parameters and global variables are declared and given values. Second, the BartzGeometry function is called. This function parameterizes the three-dimensional spider geometry and returns the relevant spatial parameters, such as cross-sectional flow area at each axial station, for a given set of radii and desired cross-

sectional spoke shape. The subroutine accepts any cross-section as a set of discrete x-y points. For the first model phase, the cross section shape is an NACA 64-008A airfoil 1" in length.

After the BartzGeometry function is called, the derivative of several axially varying flow parameters is calculated using a piecewise polynomial approximation. Following this, the BartzStartz function is called to implement the stagnation point solution. BartzStartz is used to determine the axial location at which the thickness of the theoretical flat-plate boundary layer, approximated using the $1/7^{th}$ power law correlation derived by Von Karman[27][17], coincides with the constant boundary layer thickness calculated using the stagnation point solution. The film coefficients and other relevant parameters for the flow regime up to this station are passed back to the main routine, and set as initial conditions.

The integral solver is then called within a loop; as the solver is only capable of calculating the variation of film coefficients in the axial direction, it must be called repeatedly at each surfacewise station around the inner edge of the exposed wall of the cyclically sectioned spider. The three dimensional effects are deemed negligible for a sufficiently high surfacewise spatial resolution in order to avoid adding the complexity associated with such a case.

The solver is implemented as described in the original JPL paper[28] and Appendix B(i-iii) with several slight modifications to the solver architecture in addition to the re-derived equations. Most notably, the integrals presented in the original paper are solved using the trapezoidal rule rather than Gaussian quadrature. Though quadrature lends itself well to the rapid calculation of polynomial integrals, the quadrature coefficients are dependent on the limits of integration. In applications such as finite element analysis where the limits of integration are normalized and constant, quadrature is an ideal solution; however, the limits of integration vary, if only slightly, based on the current solution state. It becomes necessary, then, to decide whether to neglect this

variation and assume constant coefficients, or to calculate the new coefficients for every integral. Calculating these coefficients, while algorithmically possible, is algebraically intensive and requires significant runtime. The trapezoidal rule provides an excellent alternative to either of these methods, accurately approximating the integral without compromising runtime. Switching from successive coefficient recalculation to the trapezoidal rule cut runtime for a single surfacewise station solution from 30 minutes down to *three seconds*. Given the need to acquire solutions at a large number of surfacewise stations, runtime reduction is extremely valuable.

With the film coefficients calculated, data may be processed using several subroutines. The first, BartzDataComparison, presents a series of graphs comparing the calculated data to a set of reference data, which by default are the data given for the case in the original JPL paper[28]. Second, Bartzmesh produces a 3-dimensional mesh of the analyzed webbing geometry, which may be colormapped based on the calculated convection coefficient at each node. Finally, BartzToAbaqus gathers, interpolates, and exports the film coefficients into a formatted file to be read into ABAQUS.

ABAQUS: Thermomechanical Finite Element Analysis

A fully-coupled thermomechanical FEA model is implemented in ABAQUS[29], using the convective heat load prescribed using the MATLAB numerical solver. This load is mapped to a defeatured model of the structural webbing. Defeaturing was motivated by the desire to make use of hexahedral elements, which offer better fidelity and faster convergence for mechanical stress analysis. Though meshing the fully featured geometry with hexahedral elements was deemed possible, it required the use of a bottom-up meshing strategy, severely increasing the time required to examine new geometries. Were this analysis to solely consider uncoupled heat transfer, tetrahedral elements would be acceptably accurate and have the added benefit of being

more robust in their capacity to fill complex geometries, but the need to calculate mechanical stress lessens this advantage.

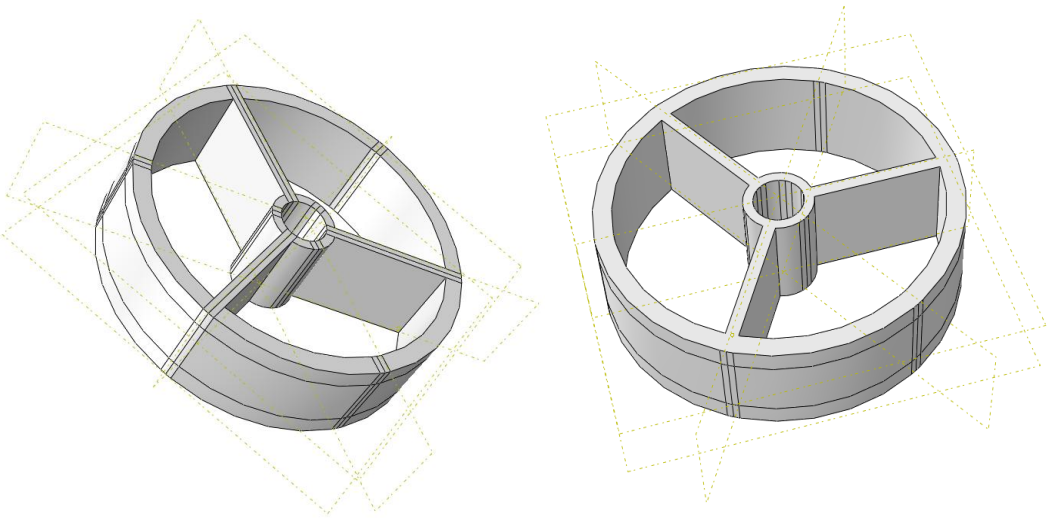

Figure 2: Partitioned, Defeatured Model

Despite defeaturing, the model required significant partitioning to make hexahedral swept meshing possible. In addition to the defeatured Spider model, a defeatured section of the aerospike and canister were added to the assembly to simulate the mechanical boundary conditions. An initial model convergence study was performed with the uniform film coefficient calculated using the closed-form Bartz equation and the outer and inner edges fully encastered. This preliminary analysis indicated that encastering the nodes that interface these two devices was an unrealistically stiff constraint. In reality, the deformation of the aerospike and canister provide some degree of stress relief to the webbing. Furthermore, it is possible that the thermal expansion of the canister will be greater than that of the spider, resulting in a gap between the structures rather than stress-inducing interference. The defeatured aerospike and canister are modeled as 304 stainless steel and constrained to the Spider using tie constraints, which allow for both conductive heat transfer and mechanical load transfer. These models were always meshed

with a 25% greater mesh density than the spider to avoid errors inherent in use of the tie constraints.

Mesh Development and Convergence

Several convergence studies were performed for this analysis. For each convergence study, the analysis was run to 1 second and contained a single coupled temperature-displacement step. The first simulation was used to validate the hand calculations[30]. The first simulation served as a reference for later convergence studies and was not intended to indicate true mesh convergence. In the first study, the average stress of the nodes of an element in the middle of one spoke was examined, and the elemental stresses were compared to the stresses predicted by the hand calculations at a given temperature.

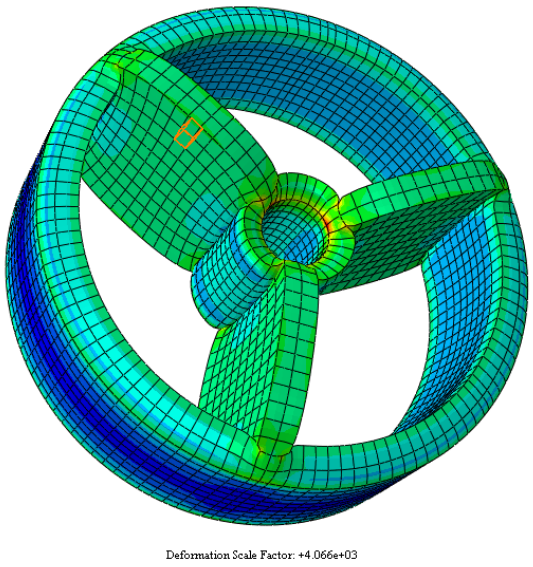

Figure 3: Element used for Convergence Studies

Table 1: Hand Calculation Comparison Study

Seed Size, in	Von Mises Stress, [psi]	T_{nodal}, [°R]	Analytical Stress, [psi]	% Difference
0.25	10800	577	13000	16.92307692
0.2	10300	572	12519	17.72505791
0.15	10000	573	11196	10.68238657
0.1	9800	570	10500	6.666666667

Next, convergence was examined for the Spider with the Bartz Solver calculated film coefficient and only constraints on the internal ring where the aerospike would sit. The purpose of this study was to determine the feasibility of this simplification by comparing the simplified model to the more in-depth models that include the spike and canister geometries. Stresses were examined in the same nodes as for the first convergence study, and are shown in Figure 4. Note that the film coefficients calculated using the Bartz equations are less than those predicted using the numerical integral method, and the resulting thermal loads are not the same as those seen in the first convergence study. Reduced integration was used for each seed size.

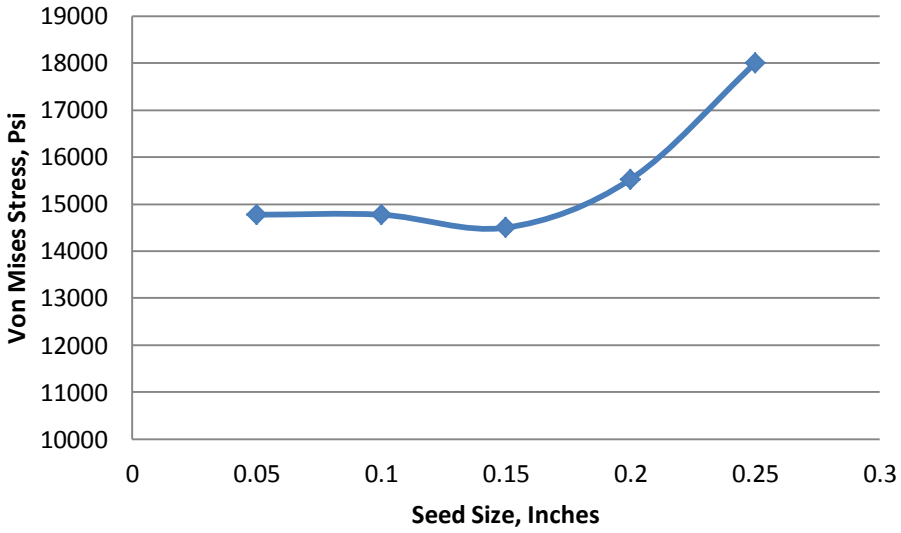

Figure 4: Convergence Study, Center Encaster BC

As shown in Figure 4, convergence was achieved for a seed size of 0.15". Further increases in mesh density yielded a negligible change in observed stress. At convergence, the stress in the chosen element was $14.775*10^3$ psi, and the nodal temperature is 964 °R. Interestingly, the variation in stress as a function of seed size was greater than the equivalent variation in node temperature. This result will later be compared to the complete model to determine the feasibility of this simplification.

The third and fourth convergence studies were performed on the full assembly model, which is shown in Figure 5. This model features the defeatured aerospike and canister models constrained to the structural webbing with a tie. Reduced integration was used for the third study, and full integration was used for the fourth study. For these studies, seed sizes as small as 0.05" were examined, though the restrictive computational intensity of this level of mesh density prohibited further use of these models. A single analysis conducted on a Lenovo T440p with a Haswell generation i7 processor and 16GB RAM required over 24 hours to run!

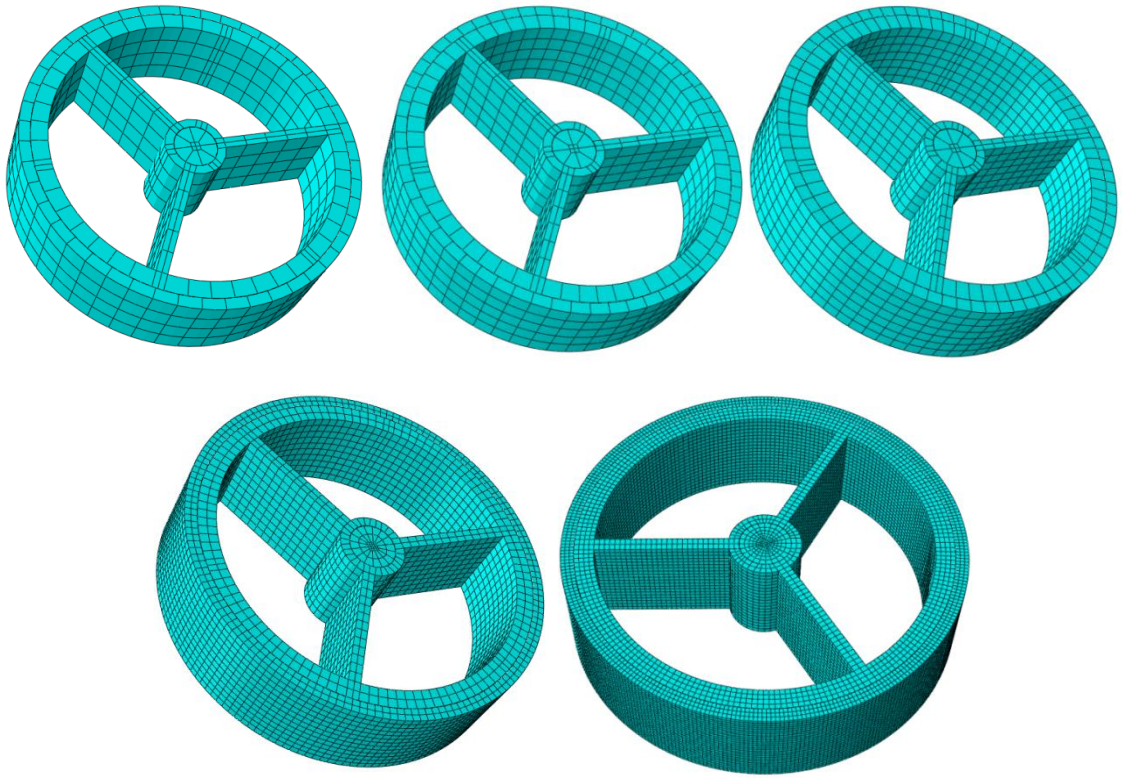

Figure 5: Mesh Density Progression

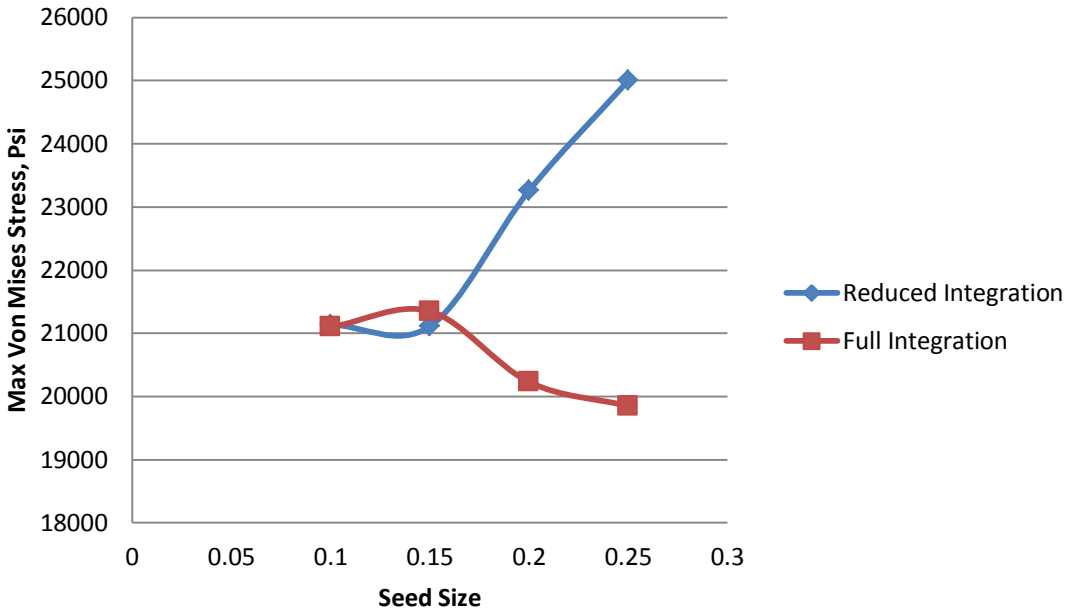

Figure 6: Full Assembly Convergence Plot

As shown in Figure 6, convergence was achieved at a seed size of 0.15" for both reduced and full integration for the full assembly. Past this point, results change by less than 1% for further increases in mesh density. Given that both forms of integration converged to the same result, reduced integration was chosen for future modeling as it is less computationally intensive. Thus, the final element chosen was C3D20RT, a 20-node thermally coupled brick, with triquadratic displacement, trilinear temperature distribution, and reduced integration.

Table 2: Element Quality Criteria

	Seed Size [in]	# of Elements	Average Aspect Ratio	Worst Aspect Ratio	Average Min Angle [°]	Average Max Angle [°]
Spider	0.25	408	2.97	4.8	75.18	104.76
	0.2	600	2.29	3.41	86.56	93.12
	0.15	1134	2.06	3.31	70.82	109.29
	0.1	3480	1.33	2.27	87.55	92.45
	0.05	22000	1.15	1.89	87.9	92.13
Spike	0.1875	60	4	4	82.5	120
	0.15	84	3.62	4	82.5	120
	0.1125	432	3.58	4.44	82.31	106.11
	0.075	624	2.89	4	82.31	106.11
	0.0375	4212	1.82	2.89	80.58	102.62
Can	0.1875	315	1.6	1.6	88.57	91.43
	0.15	546	1.25	1.25	88.5	91.15
	0.1125	936	1.14	1.14	89.13	90.87
	0.075	4082	1.24	1.24	89.14	90.86
	0.0375	25434	1.13	1.15	89.52	90.48

	Seed Size [in]	# of Elements	Worst Min Angle [°]	Worst Max Angle [°]	Geometric Deviation Factor
Spider	0.25	408	69.86	112.24	2.05E-07
	0.2	600	69.86	112.24	2.11E-07
	0.15	1134	65.49	114.51	2.83E-07
	0.1	3480	76.43	107.06	3.71E-07
	0.05	22000	73.65	106.42	1.50E-06
Spike	0.1875	60	78.75	135	3.10E-08
	0.15	84	78.75	135	3.19E-08
	0.1125	432	68.67	135	5.18E-08
	0.075	624	68.67	135	7.40E-08
	0.0375	4212	64.26	135	1.27E-07
Can	0.1875	315	88.57	91.43	2.63E-07
	0.15	546	88.5	91.15	3.96E-07
	0.1125	936	89.13	90.87	4.86E-07
	0.075	4082	88.85	91.15	5.98E-07
	0.0375	25434	89.43	90.57	1.17E-06

Element quality was evaluated at each seed size and tabulated in Table 2. For the 0.15" seed size, the elements had an average aspect ratio of 2.06 and an average minimum angle of 70.82°, while for the 0.1" seed size the aspect ratio was 1.33 and the minimum angle was 87.55°. It is of interest that convergence is achieved for the 0.15" seed size, which has a notably lower element quality, especially when the 0.1" seed size approaches an almost perfect aspect ratio (unity is desirable) and an equally excellent minimum angle (90° is desirable). Nonetheless, absolute element perfection is not necessary to achieve correct results, and the 0.15" seed size is thus the mesh of choice. For this mesh, the final number of elements was 2,502, with 56,371 degrees of freedom.

Using the fully converged model as described in the Mesh Convergence section, an analysis was run for 30 seconds and the time history of the temperatures of several nodes examined.

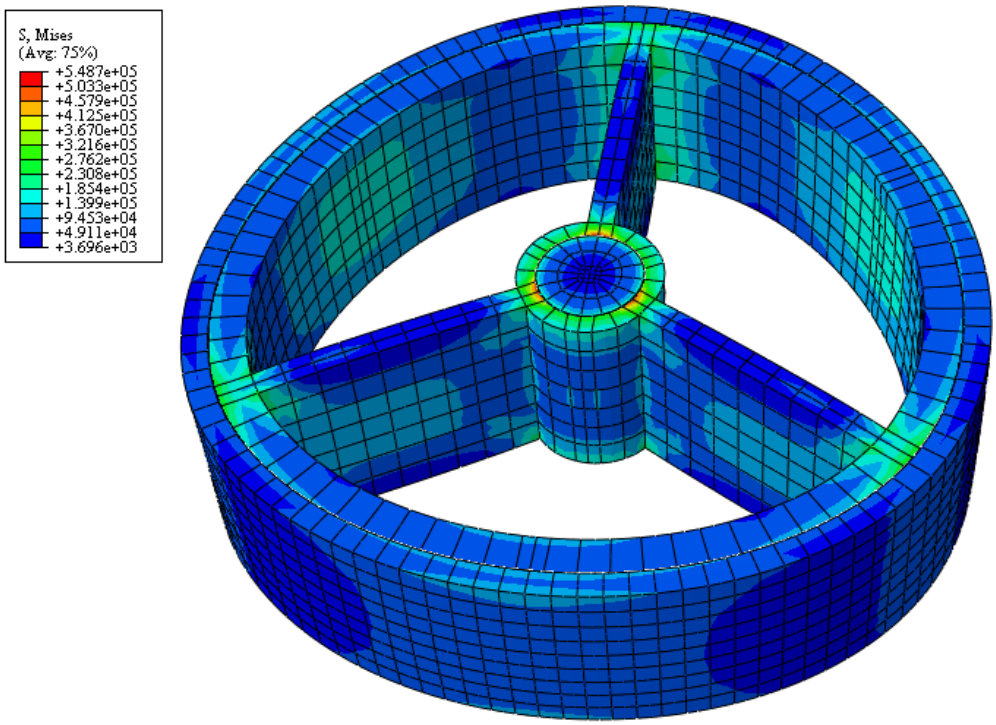

Figure 7: Stress Contour of 30-second run. Deformation scale factor 9.773

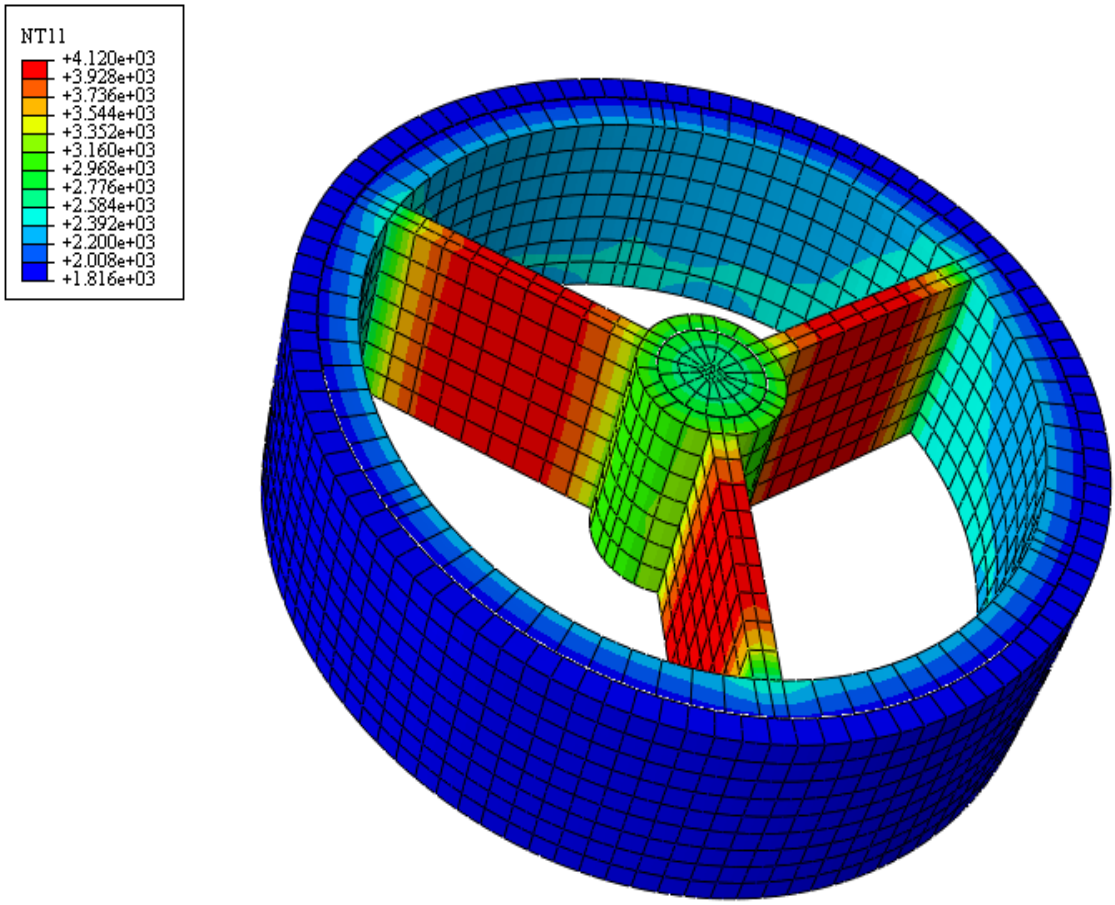

Figure 8: Temperature Contour of 30-second run. Deformation scale factor 2.30

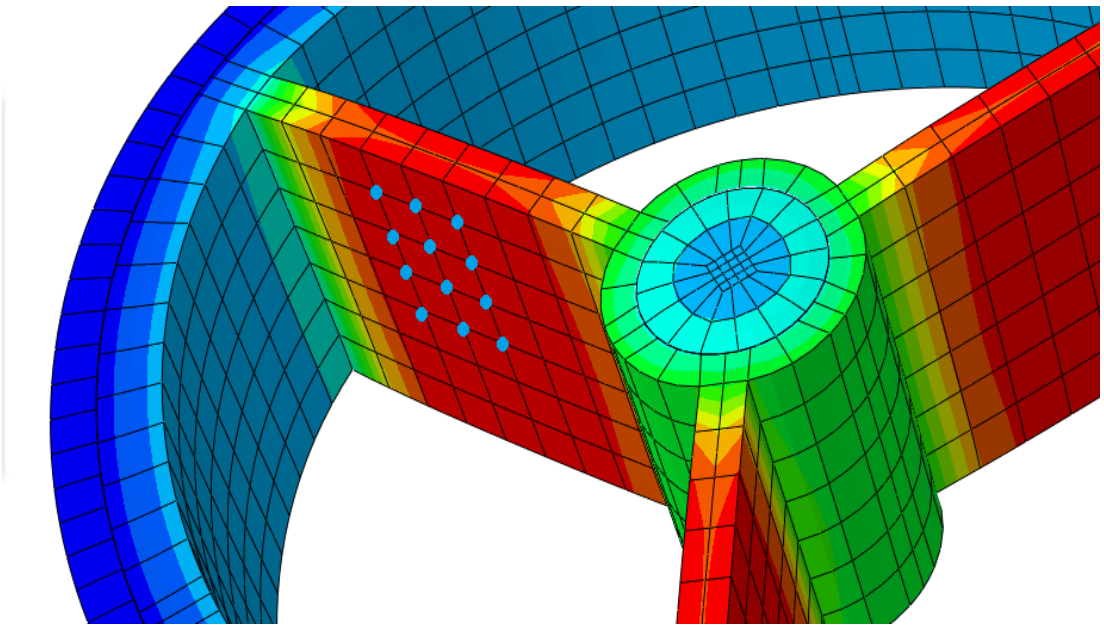

Figure 9: Examined Nodes

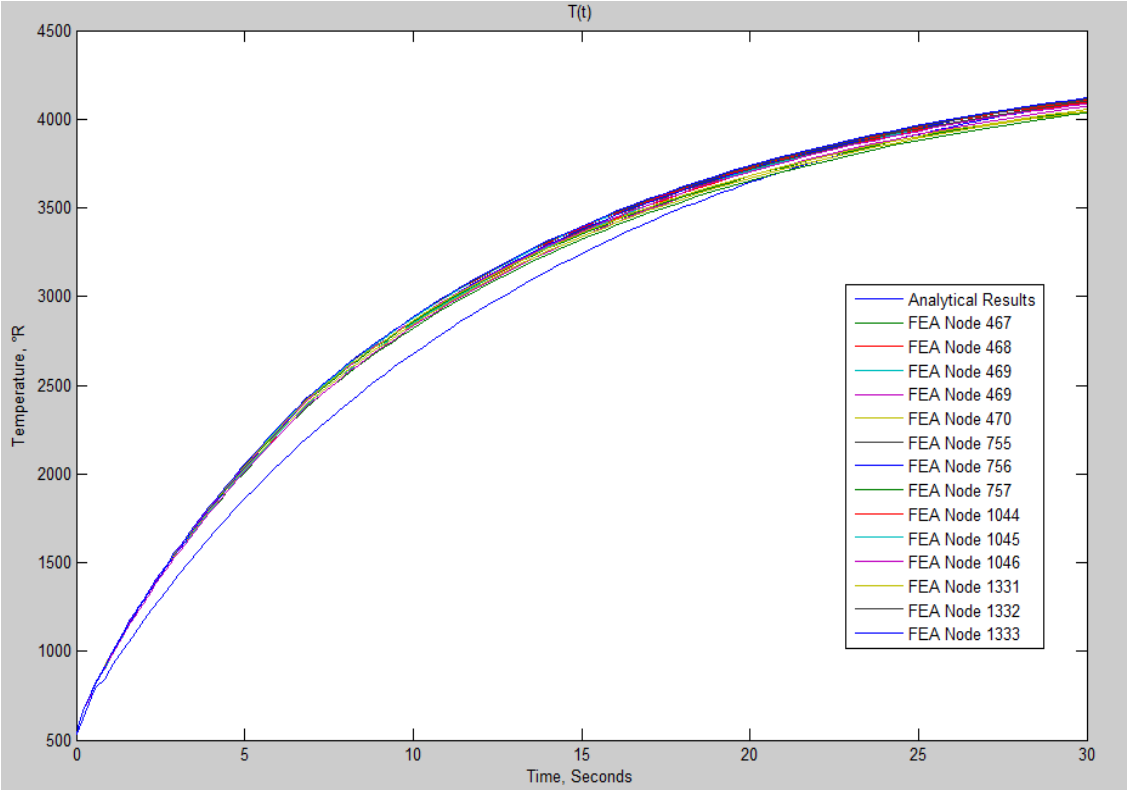

Figure 10: Nodal Temperature as a Function of Time

As shown in Figure 10, the hand calculations slightly underpredict the nodal temperatures. Interestingly, despite the distribution of film coefficients, no significant temperature gradient develops on the webbing surface until around 20 seconds into the simulation..

Model Phase 1 Conclusion

With respect to particular results, all finite element models are shown to be within a tolerable margin of error of the analytical results, indicating the validity of the models. For the basic stress calculations using fully encastred boundary conditions on the inner and outer surfaces, agreement with hand calculated estimation of stress developed in the webbing was achieved to within 7%. As shown in Figure 10, the time-based solution agreed with the corresponding analytical result with a maximum of 8.39% discrepancy.

The analysis indicates that the stress that develops in the webbing is negligible. Other than the values of 10^6 psi that develop at stress concentrations where the spider interfaces the aerospike, stress values are in the realm of $5\text{-}10^3$ psi in the webbing, which is well within the acceptable range of stress. The primary mode of failure will most likely be melting or ablation due to excessive surface temperatures, or other temperature-based defects such as deformation due to high-temperature material softening. Thus, the models for phases 2 and 3 only consider thermal effects.

IV. MODEL PHASE 2

This phase of the model involves a 2-D CFD analysis using ANSYS FLUENT to simulate flow over the cross-section of a single spoke of the webbing, then analyzes conduction within the cross-section using the PDE Toolbox in MATLAB[31].

The problem is modeled in a 2D planar domain as an NACA 64-008A airfoil of 1" length suspended in a 3" wide duct. The inlet and outlet boundaries are placed 5" from the leading edge of the airfoil, as shown in Figure 11.

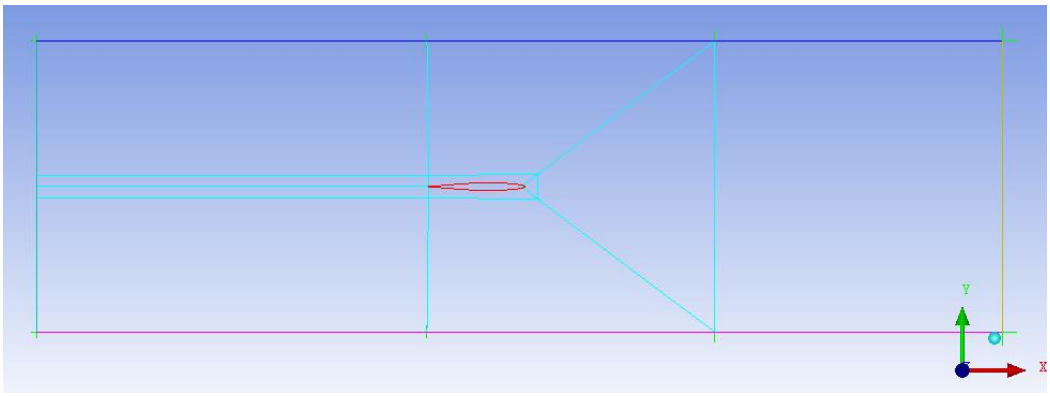

Figure 11: Problem Domain. Note that the Cyan lines represent blocking.

Fluid Properties

The fluid properties vary with O/F ratio and with flow conditions. The temperature dependence of viscosity is computed using a three-coefficient power law method, and thermal conductivity is calculated from this viscosity assuming constant specific heat and Prandtl number. The inflow conditions are determined using the NASA-CEA program, which calculates the necessary gas parameters based on a given nozzle-pressure ratio (NPR) and OF/Ratio data. The flow parameters for each case using frozen reactions are presented in Table 3.The fluid properties are based on the results for runs 91-93 of the hybrid rocket test stand.

Table 3: Phase 2 Fluid Properties

Case	1	2	3
O/F Ratio	2.396	3.897	5.67
Stagnation μ, 10-6 lbf-s/ft2	1.667	1.731	2.028
Stagnation Temperature, °R	4567.9	4976.5	5899.7
Prandtl Number	0.5207	0.3935	0.4304
Specific Heat, BTU/lbm-°R	0.4062	0.4055	0.3869
Chamber Pressure, PSIA	282.5	182.8	305.6
Ratio of Specific Heats	1.245	1.239	1.168
Molecular Weight, lb/lbmol	23.492	22.496	25.308

Flow Physics

The free stream Mach number is estimated, based on the results of the Bartz solver from Phase 1, to be 0.03, indicating that compressibility effects are negligible. The flow Reynolds number based on chamber diameter is on the order of magnitude of $Re_D=10^5$,which is consistent with the expectation that the flow will be fully turbulent upon entrance.

The primary output of interest is the film coefficient along the airfoil. Because of the possibility of ablation and erosion, the goal of the design of the Spider, as suggested by the parametric study presented later in this paper, is to maximize the available thermal capacitance such that heat can be conducted away from the surface where such phenomena will first occur, while minimizing both the surface film coefficient and the restriction of the flow. The stagnation point at the leading edge is the primary area of interest, as incompressible semi-empirical correlations used in Phase 1 indicate that the heat transfer at the leading edge is almost an order of magnitude greater than that along the airfoil. The surface Nusselt number at the stagnation point is estimated to be

on the order of 10^5, while the Nusselt number is expected to be on the order of 10^4 along the body.

Boundary Conditions

Velocity and temperature are specified at the upstream inlet. A no slip condition and constant surface temperature of 540 °R are prescribed for the airfoil and duct surfaces. The outlet specifies atmospheric gauge pressure, and the operating pressure is set to the determined value of chamber pressure for each case.

Grid

The surface heat transfer coefficient along the airfoil was compared for three separate grids to examine the effects of mesh refinement. Though the use of y^+-insensitive wall functions makes it possible to use coarse grids such that the wall adjacent cell does not necessarily lie within the viscous sublayer, the computational results best resembled the analytical results when such a mesh was used, as was the case for grid 3. The y^+ value for this grid was calculated using the skin friction coefficients produced by the Bartz solver, and the recommended relation in the FLUENT documentation[22].

Using blocking techniques in the ICEM mesh creation program, the rectangular domain was divided into an h-grid configuration with a collapsed trailing edge, which was subsequently fit to the airfoil. Though a c-grid or y-grid configuration might be appropriate for other airfoil-type analyses (such as an airplane wing or series of turbine blades), the presence of the duct prevented the use of the far-field pressure boundary condition, and necessitated the aforementioned techniques. Several scripts were also produced to allow for rapid examination of a variety of airfoil profiles, though for the purposes of this project only a single profile was examined. The geometric2 bunching law was subsequently used to select node spacing and produce a premesh, which was then converted to an unstructured mesh for use in FLUENT. The edge parameters used

are presented in Table 4. “Radial Nodes” refers to the number of nodes placed outward from the airfoil in the inner block, while “Nodes at Nose” and “Nodes at Body” refer to the surfacewise number of nodes at those respective sections.

Table 4: Grid Parameters

Grid	First Cell y^+ (in)	Radial Nodes	Nodes at Nose	Nodes on Body
1	0.05	10	25	100
2	0.05	20	25	100
3	0.0001	80	250	250

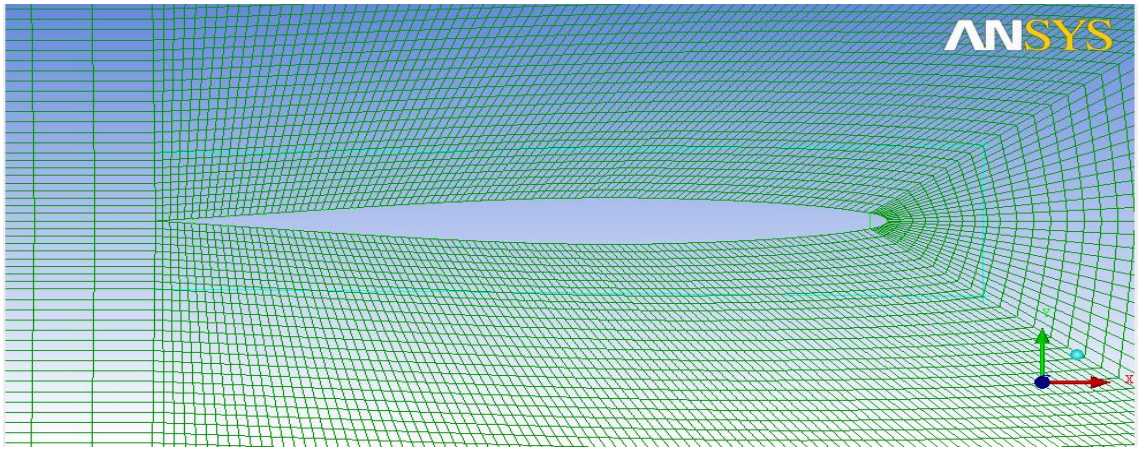

Figure 12: Grid 1. Note the increased bunching near the nose.

Case Setup

Using the conditions described in section three, the FLUENT case was set up. Three runs were made for case one (with an O/F ratio of 2.396) with three separate grids, and then two subsequent runs were made for cases two and three.

Calculation

Though density was assumed to be constant, better convergence was achieved using the density-based solver, as solution steering with Full Multi-Grid initialization provided a robust method and reduced sensitivity to the selected Courant number and under-relaxation factors. For the viscosity model, both k-ε with enhanced wall functions and k-ω (SST) with compressibility effects were compared, with little difference in yielded results. k-ε was chosen as the solver for the following

analyses, as it was shown to converge quicker than k-ω (SST) while yielding the same results. The implicit formulation with Roe-FDS flux was used, with second order upwinding schemes selected for all solution methods due to the improved accuracy associated with this discretization

.

The density of the fluid was set to "Ideal Gas," though density should largely be constant as compressibility effects are negligible. As is consistent with the assumptions outlined by Bartz, specific heat and Prandtl number were assumed constant, but viscosity (and by extension thermal conductivity) were assumed to vary by a power-law profile, necessitating the creation of a user-defined function for thermal conductivity, bartzTCF.c. Results from FLUENT were imported into MATLAB and compared against the analytical results achieved using the Bartz solver.

Grid Independence Study

For Case 1, the three grids outlined in section 4 were run and the resulting fields of film coefficients along the airfoil were compared to the Bartz results. As shown in Figure 13, grids 1 and 2 overpredict the film coefficients along the body by around 30%, but underpredict the heat transfer at the stagnation point. Grid 3 slightly overestimates the solutions throughout the domain, but generally shows good agreement with the Bartz results.

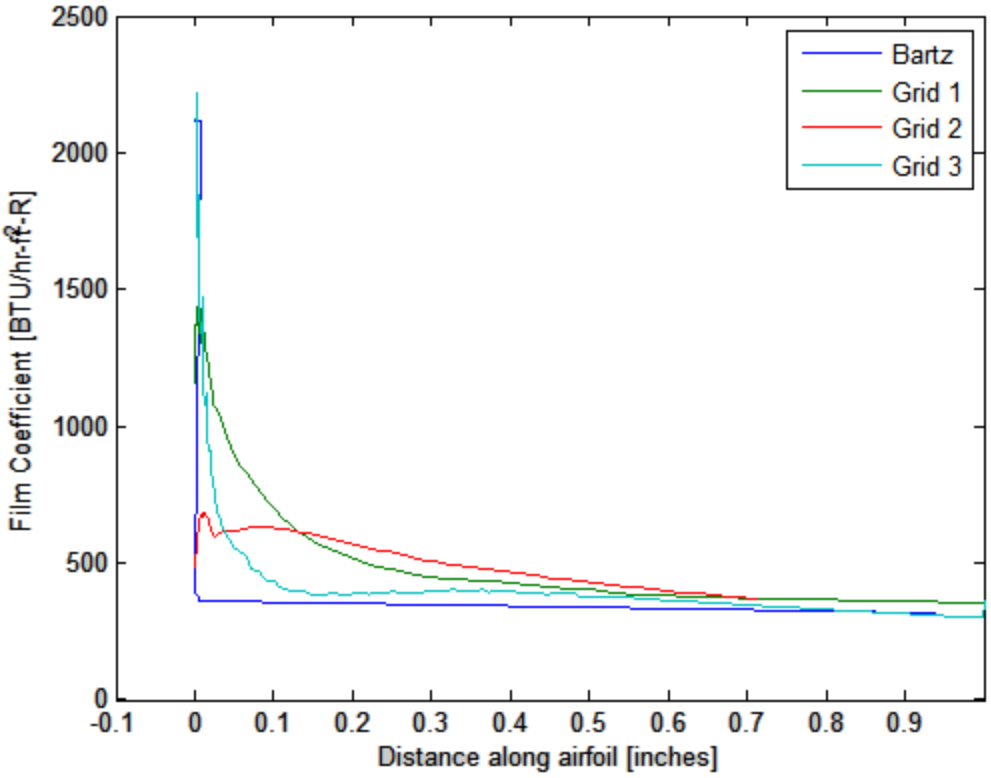

Figure 13: Mesh Convergence Study

The primary difference between cases is the value of the film coefficient at the forward stagnation point. FLUENT showed excellent agreement with the incompressible correlation in this region; however, for case 1 it returned slightly higher values over the body, and lower values over the body for cases 2 and 3. Shown in Figures Figure 14 through Figure 16 are graphs comparing computational and analytical results for each case. Case 3 (O/F Ratio of 5.67) resulted in the greatest film coefficients, both at the stagnation point and over the airfoil. This result is consistent with what has been observed experimentally: the test stand is typically run fuel-rich in order to reduce ablative effects, so for a case with higher oxidizer content, the resulting heat transfer should be proportionally higher.

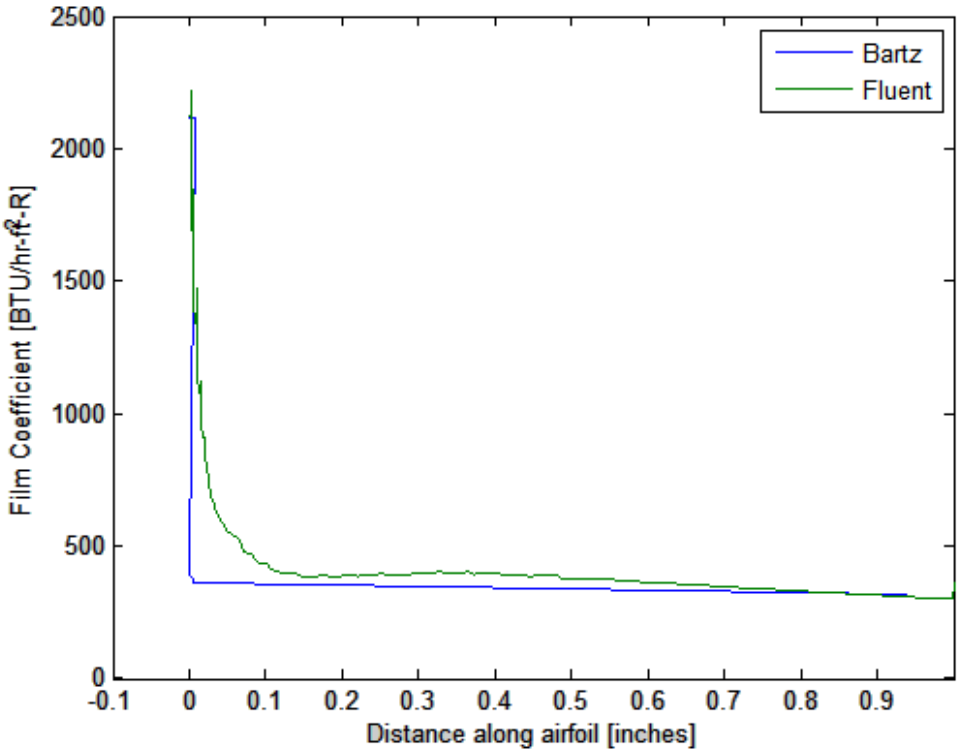

Figure 14: Analytical and Computational Film Coefficient Distribution, Case 1

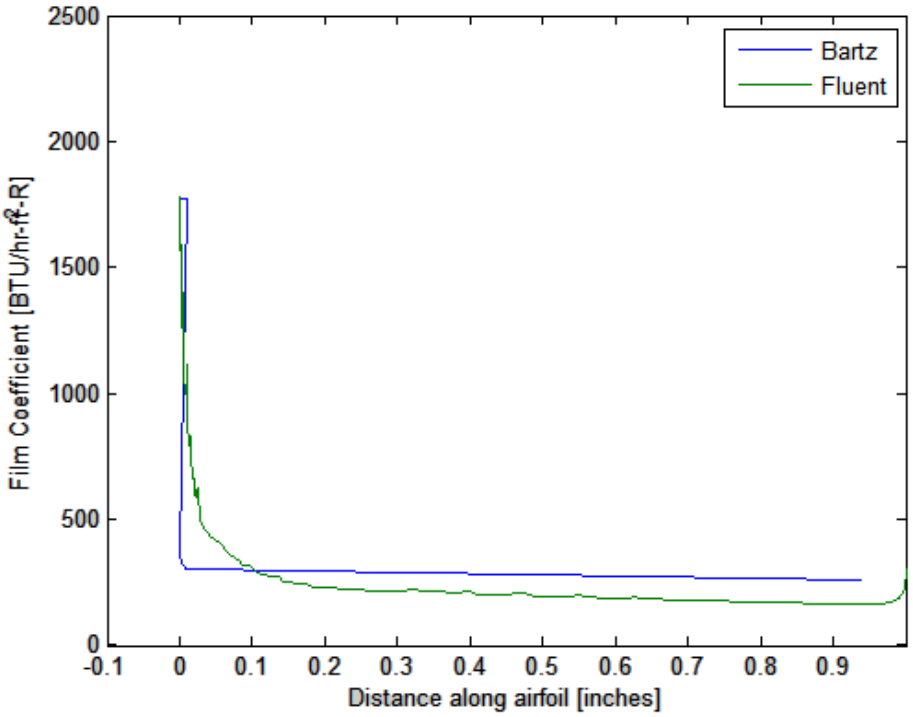

Figure 15: Analytical and Computational Film Coefficient Distribution, Case 2

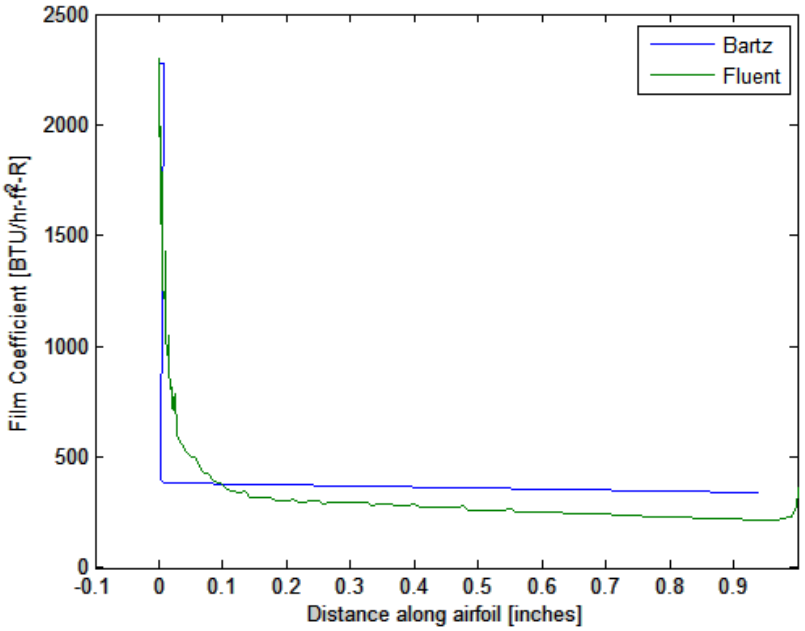

Figure 16: Analytical and Computational Film Coefficient Comparison, Case 3

The variation of the computed stagnation point film coefficient as a function of the oxidizer to fuel ratio is shown in Figure 17. While it is expected that a higher O/F ratio would yield greater heat transfer, for case 2 (O/F=3.897) the chamber pressure is significantly lower than for the other cases, so the result is not necessarily indicative of the general trend.

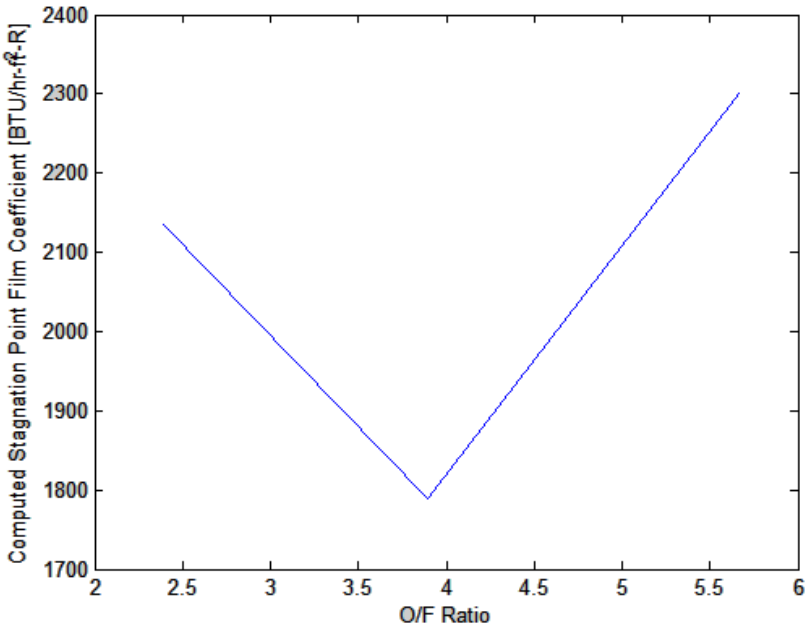

Figure 17: Stagnation h_g as a function of O/F Ratio

Additionally, shown in Figure 18 and Figure 19 are the contours of static pressure and velocity vectors (colored by temperature) at the leading edge in order to aid flow visualization.

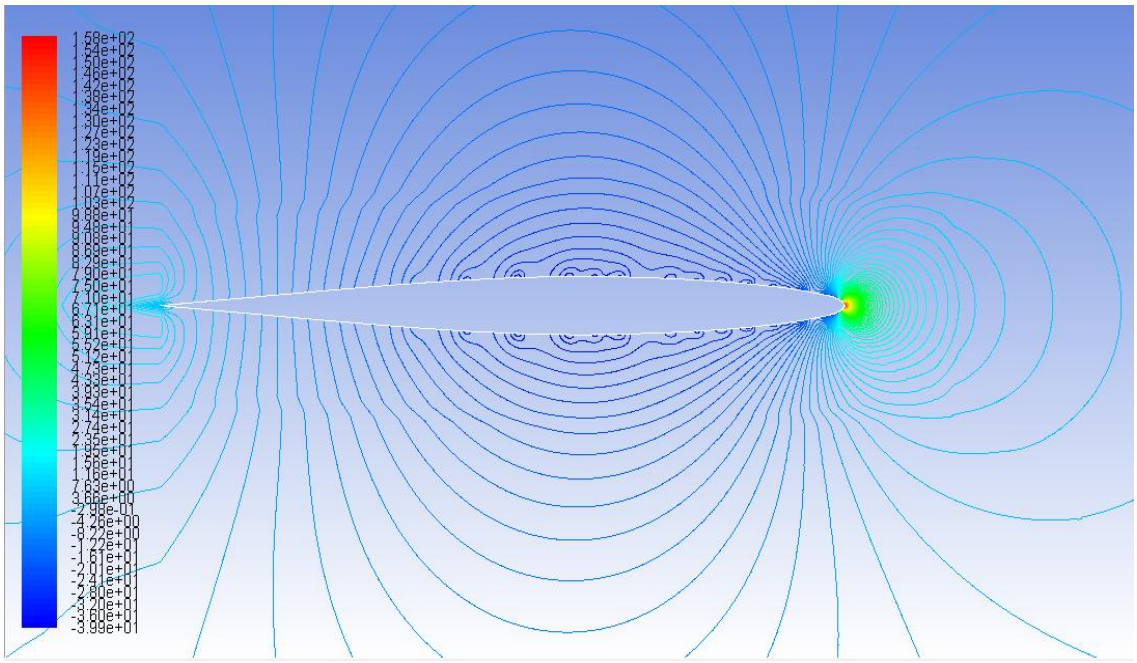

Figure 18: Contours of Static Pressure. Note the singularity at the leading edge.

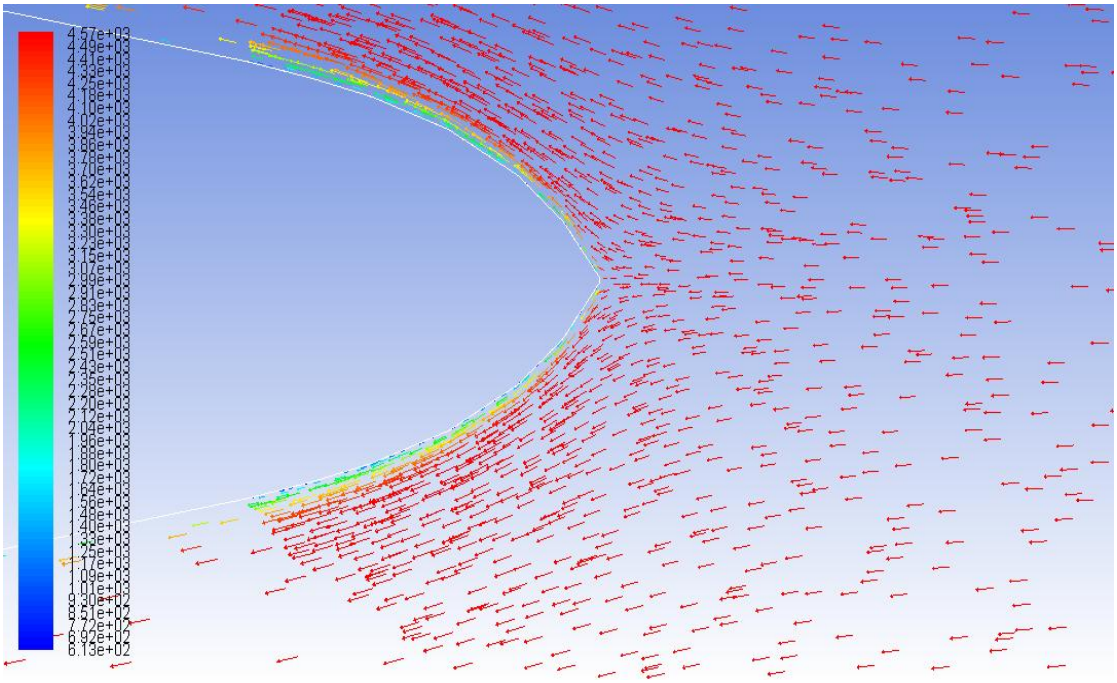

Figure 19: Stagnation Point Velocity Vectors colored by Temperature

Parametric Study

A parametric study, motivated by the need for quantitative data usable in experimental design, was performed to determine what cross-sectional geometry would result in the greatest device lifetime. Using the data from Runs 86 and 91, the variation in heat load and part life were examined as a function of nose radius, axial length, and material choice. ANSYS FLUENT was used for the CFD analysis and conduction within the part was simulated using MATLAB's PDE toolbox. The thermophysical properties of the solid domain were those of 304 stainless steel.

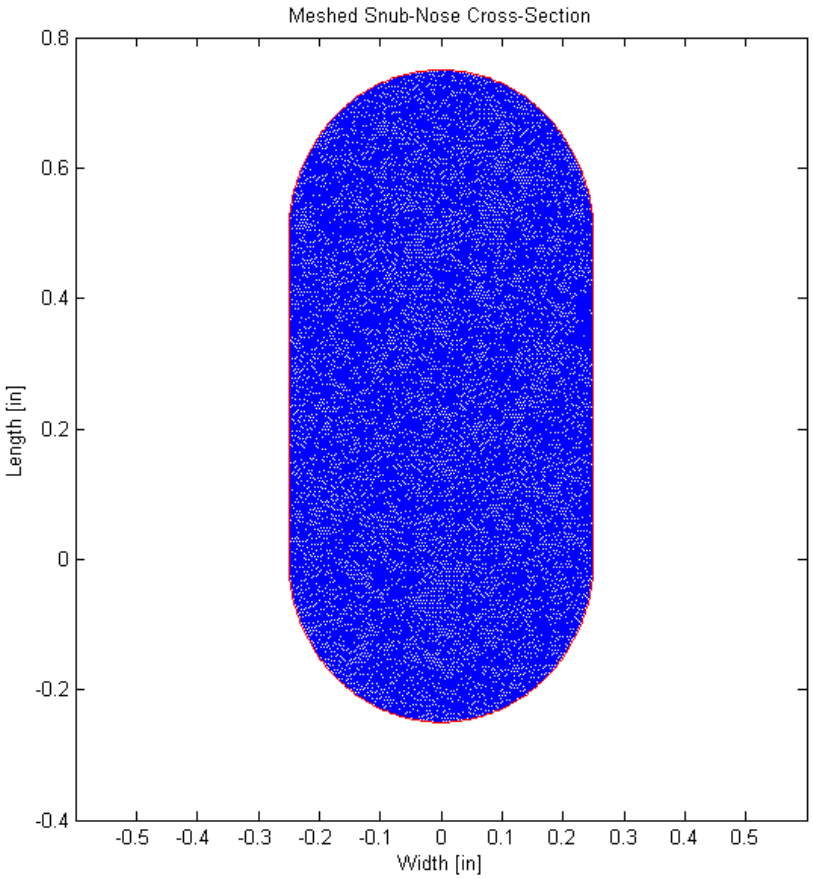

Figure 20: Meshed Snub-Nose Cross-Section

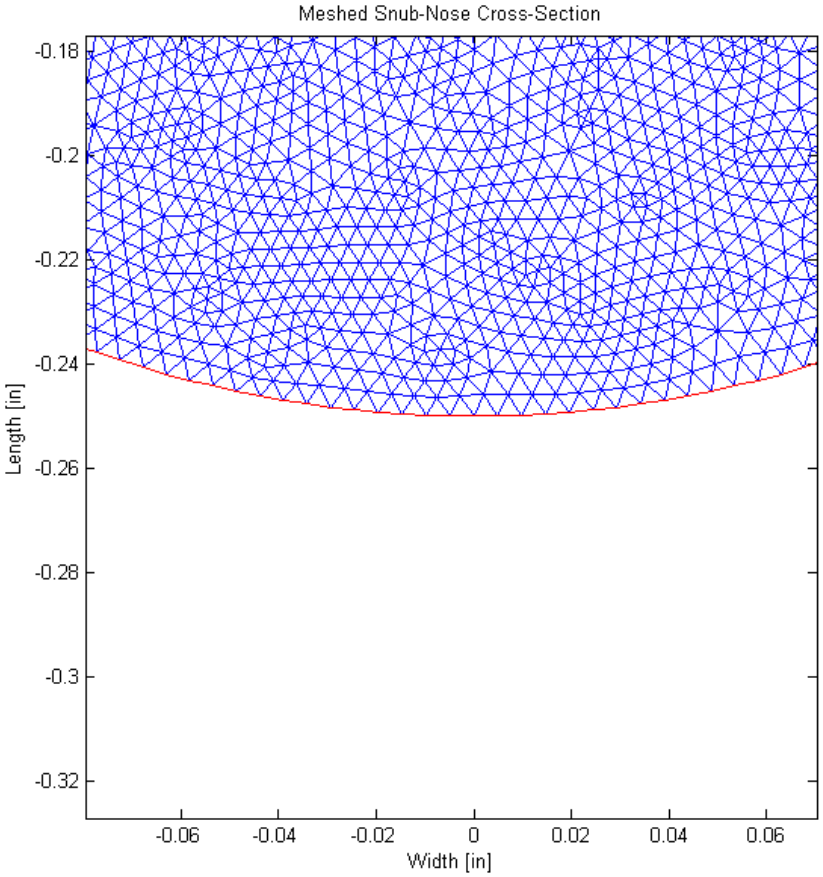

Figure 21: Leading Edge Mesh Detail View

For each configuration, mesh convergence was obtained for both the FLUENT and the PDETOOL case. Table 5 summarizes the results of the first portion of the parametric study. For this section, the nose radius was varied and the resulting total heat flux and max film coefficient were plotted against the variation in radius, exposed surface area, and volume.

Table 5: Parametric Study Parameters

Nose Radius [in]	Length [in]	Exposed Area [in^2]	Volume for 3-in spoke [in^3]	Max Film Coeff. [10^3 BTU/h-ft^2-°R]	Heat Flux [10^3 BTU/h]
0.0625	0.375	0.5713	0.1774	1.35	28.049
0.125	0.5	0.8927	0.5222	1.00	38.415
0.25	0.5	1.2854	1.3390	0.80	53.887
0.375	0.5	1.6781	2.4504	0.75	70.351

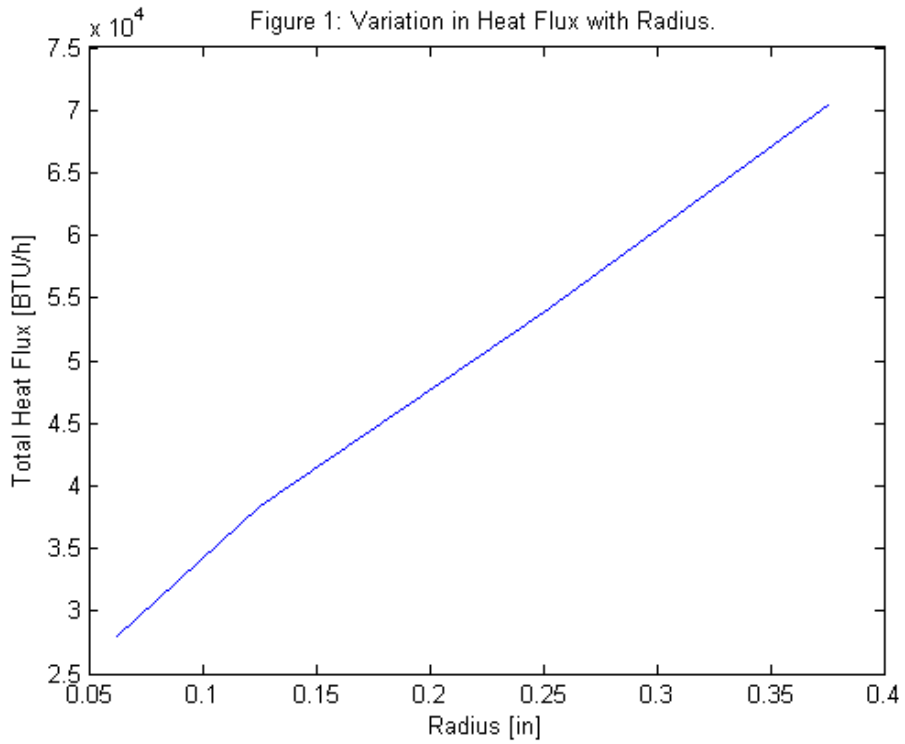

Figure 22: Total Heat Flux as a Function of Spoke Radius

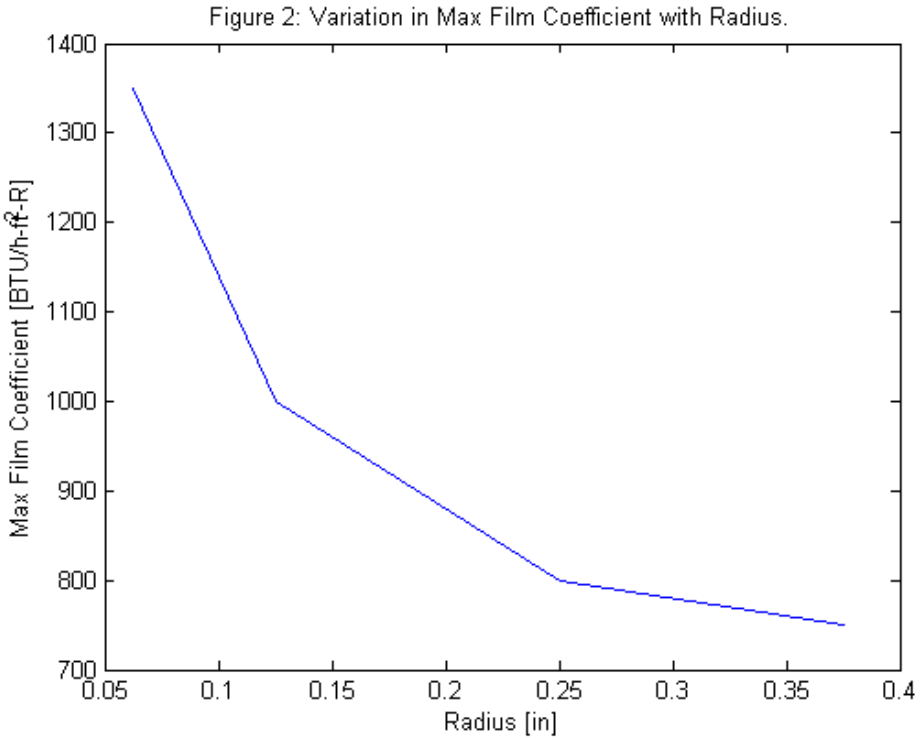

Figure 23: Max Film Coefficient as a Function of Spoke Radius

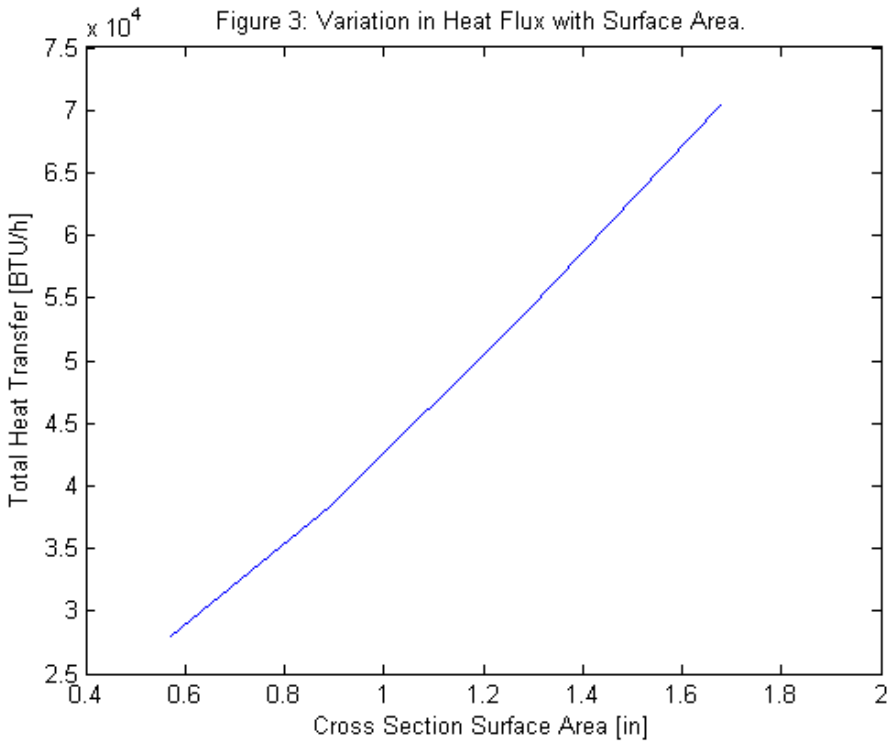

Figure 24: Total Heat Transfer as a Function of Surface Area

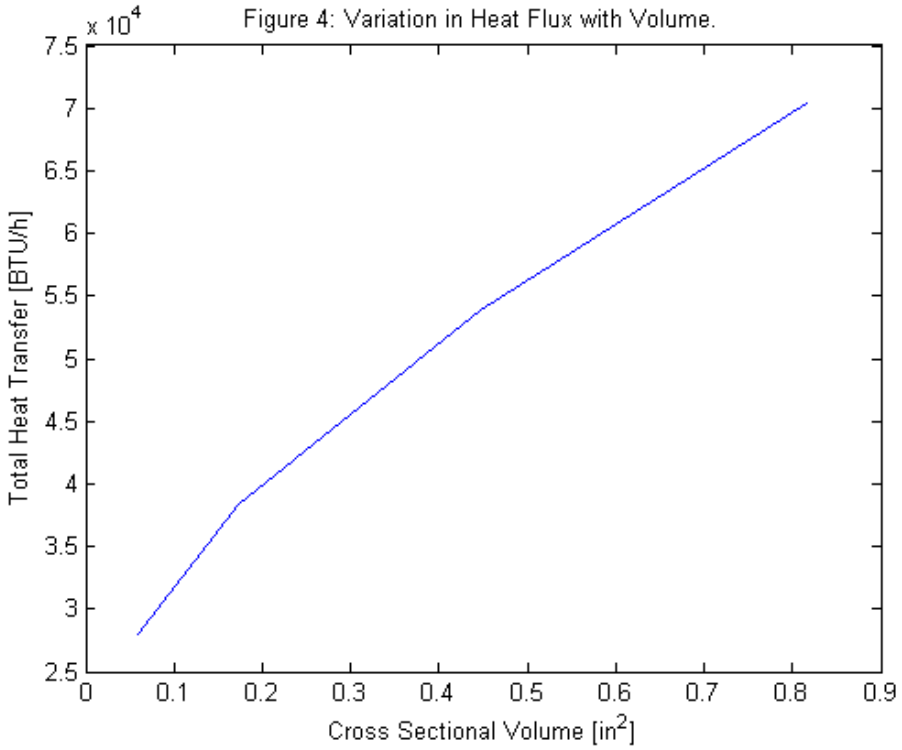

Figure 25: Total Heat Transfer as a Function of Cross Sectional Volume

The second portion of the convergence study consisted of a transient analysis with the fully converged meshes for a 0.5" diameter spoke of 0.5" and 1.0" length, as well as a 0.375" diameter spoke of 0.5" length. For each configuration, the maximum surface temperature and several internal temperatures of interest are plotted against time.

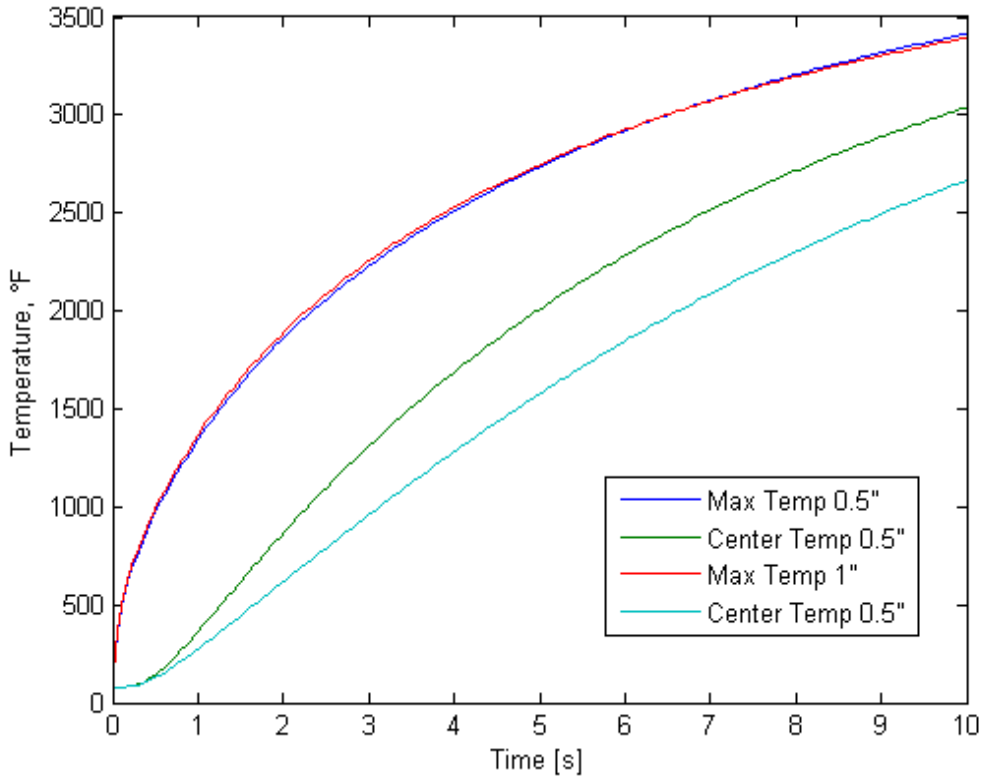

Figure 26: Maximum and Center Temperature, 0.5" Diameter Spoke

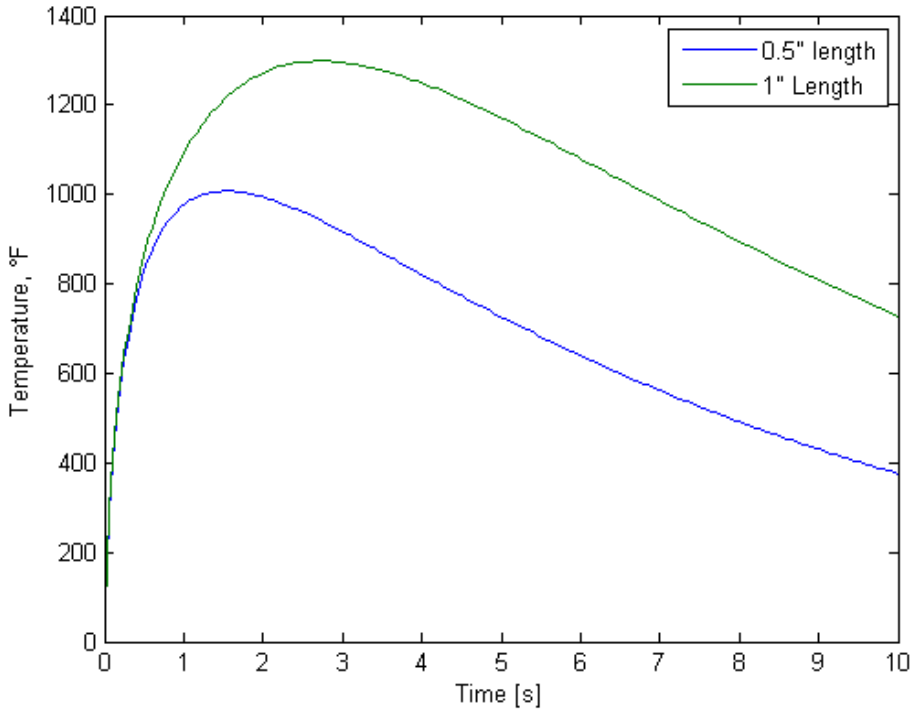

Figure 27: Difference between Max Surface Temp and Center Temp for 0.5" radius

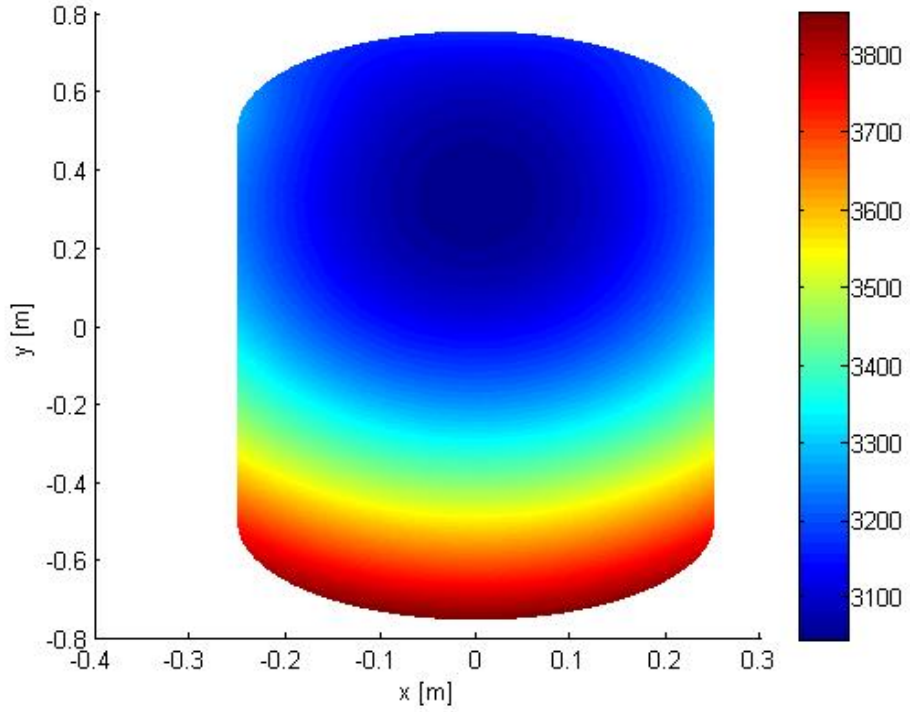

Figure 28: Temperature Distribution in 0.5" Diameter, 1" Long Spoke at t=10s

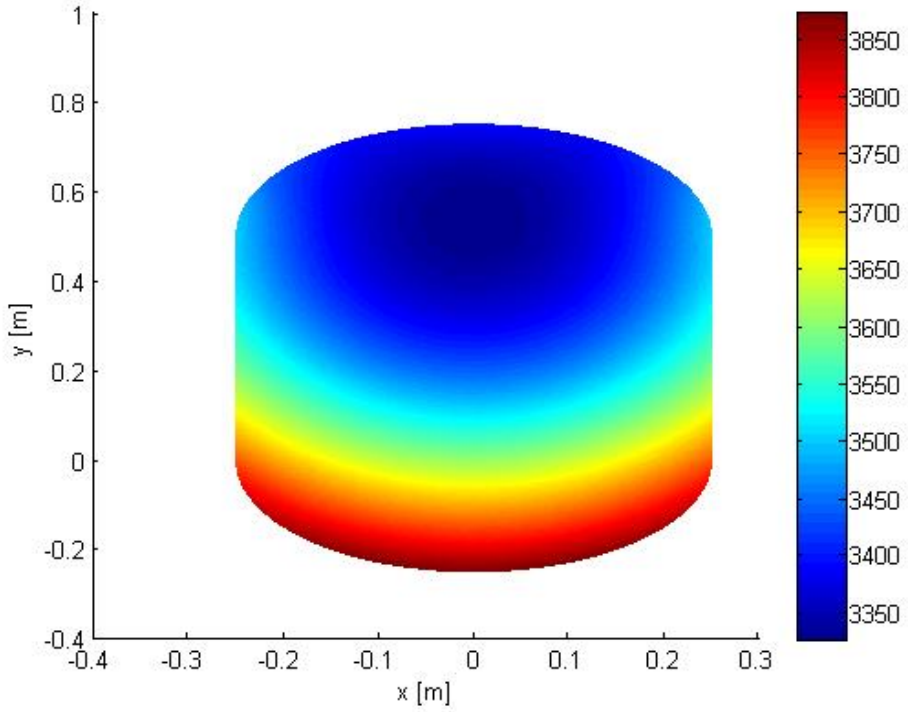

Figure 29: Temperature Distribution in 0.5" Diameter, 0.5" Long Spoke at t=10s

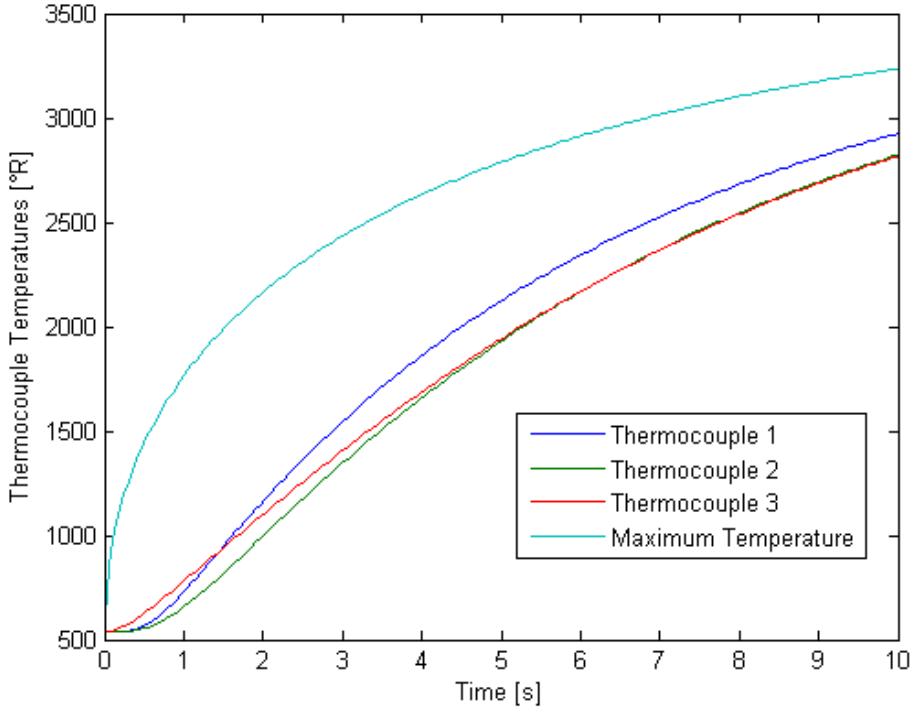

Figure 30: Transient Temperatures for 0.375" Diameter, 0.5" Length Spoke

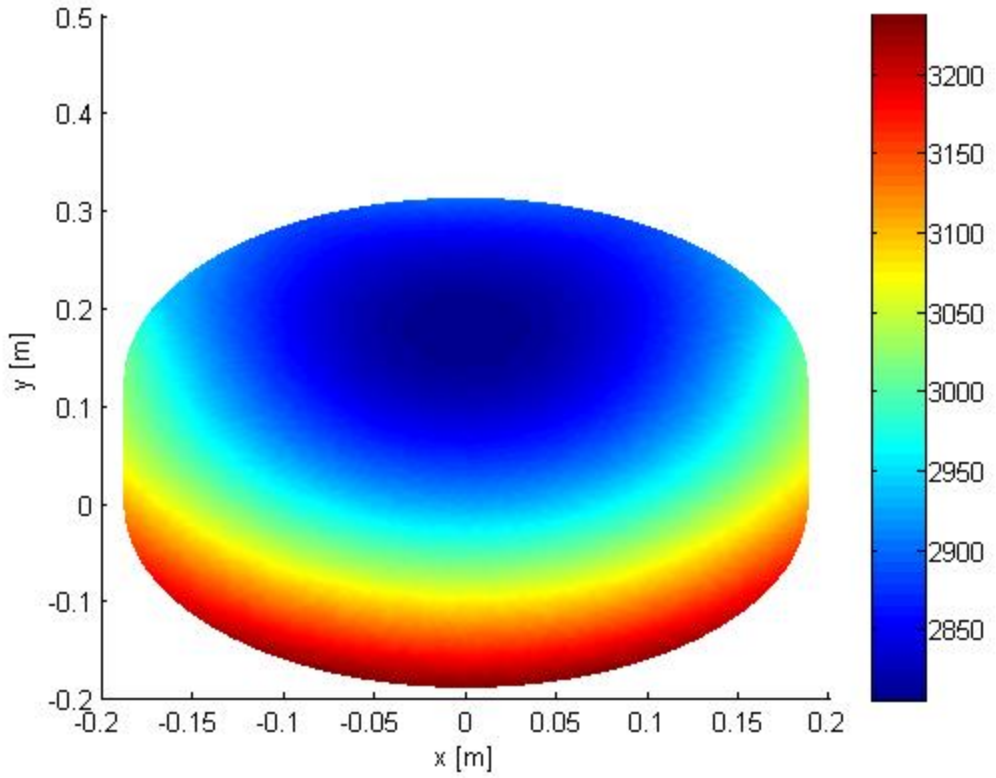

Figure 31: Temperature Distribution in 0.375" Diameter, 0.5" Length Spoke at t=10s

The parametric study imparted some valuable qualitative understanding used in the successful design of the experimental rig that would later be used to validate the third phase of the model. It is important to consider that the Spider is designed to enter an environment where it cannot possibly survive. As such, rather than designing to ensure. The most important revelation is that part life is best extended by maximizing the amount of thermal capacitance available at the stagnation point by selecting a wide, rounded profile, as opposed to a thin knife-edge. This is contrary to what intuition might have suggested, which was that minimizing the surface area at the stagnation point would reduce the heat transfer and improve part life. While it is true that a knife-edge profile reduces the local heat flux, the transient domain must be considered in order to fully understand what factors affect part life. The goal is not to minimize heat flux, but to keep the maximum temperature below a threshold value for as long as possible. Because of the extreme external temperatures, were the metal surface to be directly exposed the exhaust without

the extra layer of soot that develops due to the fuel-rich incomplete combustion, the material at the stagnation point would quickly rise well beyond the melting temperature of steel and erode or ablate at a catastrophic rate unless there existed a sufficiently large amount of surrounding material through which the heat might be conducted [32]. In this way, increasing the available thermal capacitance might be thought of as a method of "passive indirect cooling," as even without an active coolant convecting away heat, it is conceivably (though not practically) possible to produce a structural webbing that could survive in steady state simply by nature of being so large that the inbound heat is merely dispersed into its domain without ever causing a noticeable increase in temperature. The size restrictions of the existing hardware and the focused intensity of the flame make this impossible.

Minimizing the magnitude of the heat transfer at the leading edge comes at the cost of minimizing the local thermal capacitance, meaning that any heat that gets transferred into the leading edge will result in a significantly greater rate of temperature increase. Though the overall heat into the part might be lessened, the ability of the part to withstand said heat is further lessened, especially at the exposed surface where thermal failure is most likely. Considering the domain as an approximate cylinder may reveal why this is: the exposed surface area (and therefore the inbound heat flux) scales linearly with the radius, but the cross-sectional volume (and therefore the cross-sectional thermal capacitance) scales with the square of the radius. With an increasing radius, the latter is obviously going to increase at a greater rate than the former. If part life is assumed to, on similar magnitudes, scale negatively with heat transfer but positively with cross-sectional volume, it behooves the designer to maximize the size of the Spider to allow it to absorb more heat, rather than attempt to minimize its size to reduce heat flux. It should be noted, however, that the design tradeoff between increasing thermal capacitance at the cost of increasing heat transfer reaches a threshold as the cross-sectional area through which flow may pass begins to reach a constriction ratio that might cause transonic flow. It is understood that heat transfer is typically greatest near

the throat of a rocket nozzle where flow is choked, and as such great care should be taken to ensure that the local permitted flow area does not enter this regime. This result lends itself well to future design and manufacture. Producing knife-edge parts in a cyclically symmetric shape is difficult to do with precision with the facilities available at Cal Poly, and doing so would preclude the possibility of embedding thermocouples in the apparatus as there would be no space available for even a slender thermocouple wire. Furthermore, producing constant-radius features can be done more easily than variable-radius features. With the use of a corner-rounding end mill, such features can be milled using manual machines, eliminating the need for CNC or other equipment that may not be readily available.

Model Phase 2 Conclusion

Using FLUENT to simulate the turbulent flow over the airfoil cross-section of the structural webbing produced results that largely agreed with the previously constructed numerical solver implemented in MATLAB, suggesting that further CFD simulation would be appropriate to examine if three-dimensional effects or other phenomena such as combustion, radiation, or multispecies flow will significantly alter the observed heat load. FLUENT is capable of predicting the field of film coefficients with acceptable fidelity for a variety of rocket flow conditions, so long as a sufficiently refined grid is used. Even with y^+-insensitive wall functions, it was found that a grid whose wall-adjacent cell centroid was within the viscous sublayer produced the most accurate results for all three cases. The heat transfer at the stagnation point was confirmed to match with semi-empirical correlations, and seen to increase with O/F ratio and chamber pressure. The results of the parametric study provided suggestions for apparatus design with the goal of increasing part life, and indicated that part life is best improved by increasing volume (and therefore thermal capacitance) even at the cost of increasing total heat flux, such that the temperatures at the surface, where thermal failure is most likely, can be kept below critical values.

V. MODEL PHASE 3

For the final phase of the model, the flow domain was defined in three dimensions and the resulting heat transfer data mapped to a fully featured model of the solid domain. The model was partitioned to take advantage of cyclic symmetry, and is shown in Figure 32 and Figure 33.

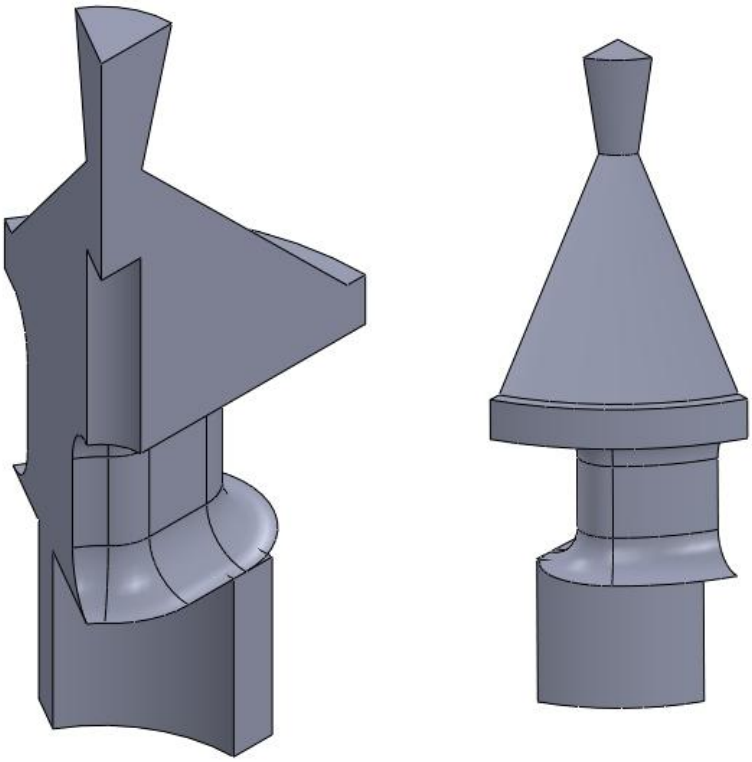

Figure 32: Fully Featured Flow Domain

In addition to the previously modeled thermal and fluid phenomena, this model considered the insulating effects of the soot layer deposited on the experimental prototype, as well as the conductance changes due to the presence of the instrumentation and the contact conduction between the thermocouple cartridges and the device body. The thermocouple cartridges are treated as a lumped capacitance with homogenous thermal conductance and specific heat, the values of which are calculated using a resistance-network approximation. ANSYS Workbench was used to mesh the domain and run the FLUENT simulations. Results from the CFD were exported as time-invariant boundary conditions to ANSYS's Transient Thermal analysis module, where the temperature distribution within the solid domain was calculated.

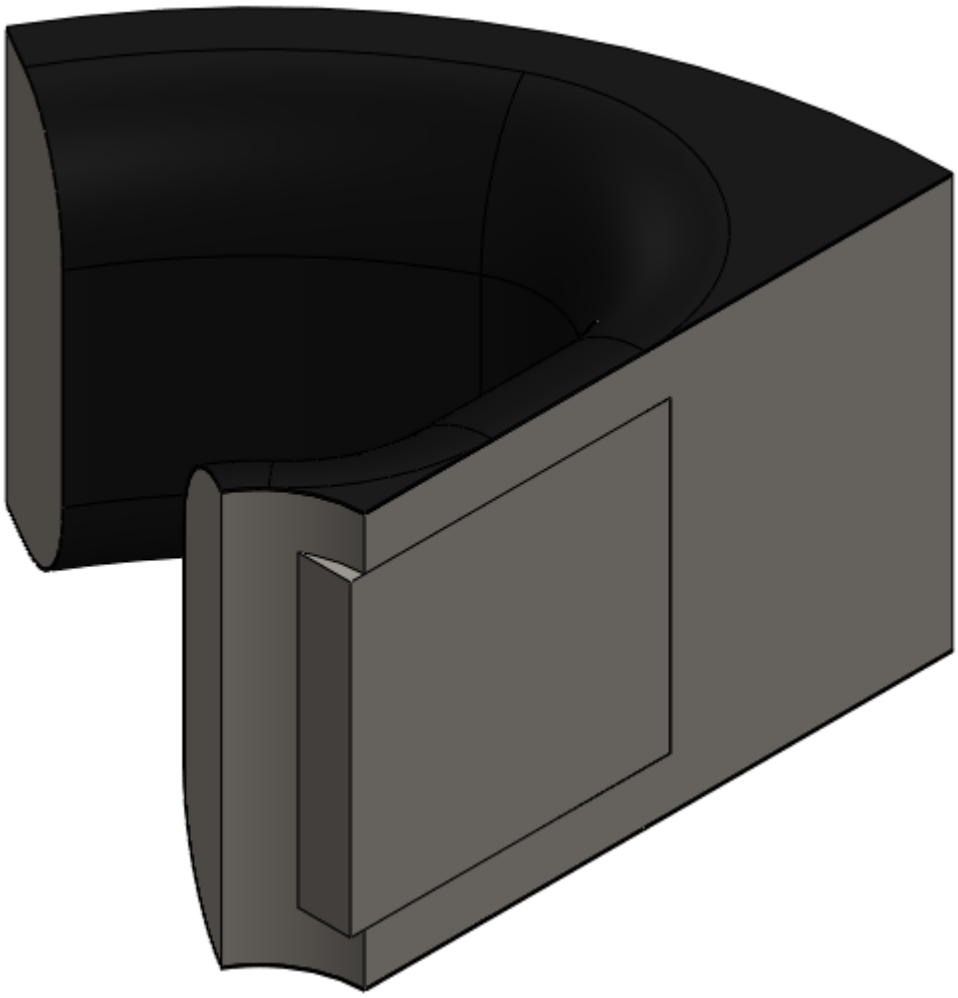

Figure 33: Fully Featured Solid Domain

This model phase was initially validated using the flow parameters for Run 86, detailed as Case 1 of Table 3. Grid independence was established using flow parameters from Run 103. For each run, the boundary conditions and fluid parameters were changed to match those estimated for the experimental runs. The simulation results are compared to experimental results in Section VII.

Material Properties

The thermophysical properties of the homogenous 304 stainless steel used in this simulation are presented in Table 6[33][34].

Table 6: Thermophysical Properties of 304 Stainless Steel

T(K)	Rho [kg/m^3]	Cp [J/kg-K]	k [W/m-K]
293.15	7910	456	14.2505
363.15	7880	490	15.38458
473.15	7840	532	17.39556
593.15	7790	557	19.28444
703.15	7740	574	20.84367
813.15	7690	586	22.25281
923.15	7640	599	23.66194
1033.15	7590	620	25.07049
1143.15	7540	645	26.4785

Soot Estimation

Combustion of hydrocarbon fuels frequently results in deposition of black soot on the surface of any object in the flow, especially if the combustion is fuel-rich. The insulating effect of the soot deposits on the webbing surface is non-negligible, and is modeled as a physical layer 0.005" thick that covers the solid domain. The temporal variation of soot thickness due to transient deposition is neglected for simplicity and is not feasible with the current experimental setup. The thermophysical parameters of the soot were estimated using methods suggested by Preciado[35] and are presented in Table 7.

Table 7: Thermophysical Properties of Modeled Soot

Thermal Conductivity, [W/m-K]	0.0671
Density, [kg/m^3]	40
Specific Heat, [J/g-K] as a function of Temp, [K]	0.0012*T+0.5

Cartridge Conductance Correction

In order to account for the effect of contact resistance between the thermocouple probes and the cartridge, the cartridge is modeled as a separate part of the solid domain with a modified conductance[36]. A passive resistance network method is used to evaluate the effective conductivity, and implemented as a temperature-dependent orthotropic thermophysical material property of the cartridge partition visible in Figure 33.

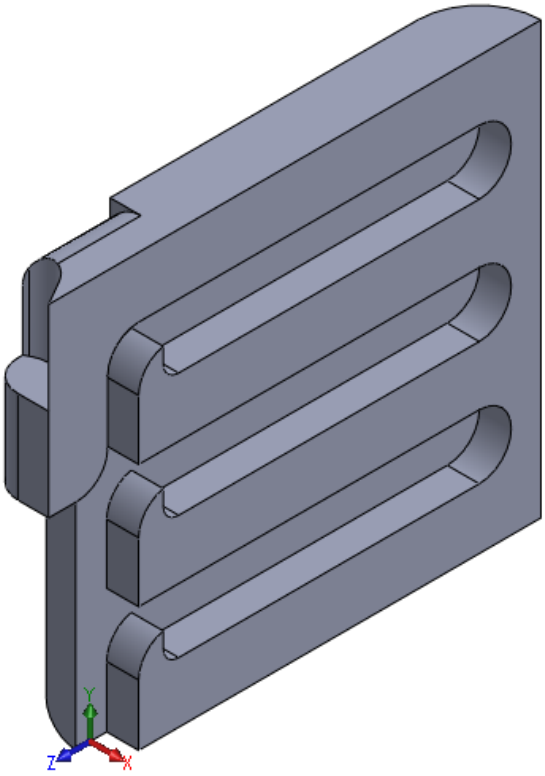

Figure 34: Cartridge with Thermal Resistance Network Axes

The thermal resistance networks used to approximate the thermal conductivities in each of the three directions, as shown in Figure 34, are presented in Figures Figure 35, Figure 36, and Figure 37.

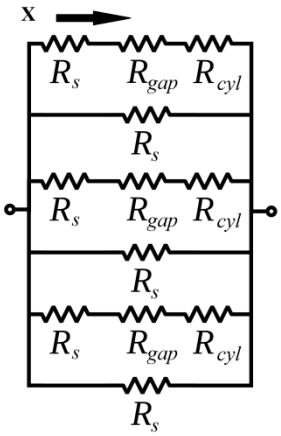

Figure 35: X-Direction Thermal Resistance Network

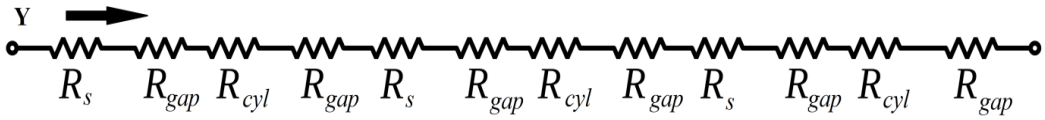

Figure 36: Y-Direction Thermal Resistance Network

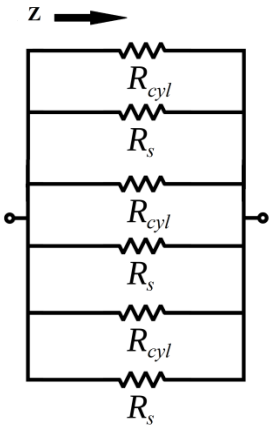

Figure 37: Z-Direction Thermal Resistance Network

In the above figures, R_S represents the thermal resistance of the homogenous sections of 304 stainless, which is taken to be the length of the material section in the direction of interest divided by the product of the thermal conductivity and the cross-sectional area. R_{cyl} represents the thermal resistance of the cylindrical probe, which is taken to be the same as that of R_s with the value of thermal conductivity of the thermocouple probes substituted in. R_{gap} represents the combined thermal resistance of the air gap and the cylinder-flat line contact interface. The calculations for this resistance value are performed using MATLAB in accordance with the parallel flux-tube model presented by Yovanovich[37] and are presented in Appendix B(xii). The computed orthotropic thermal conductivities are presented in Table 8.

Table 8: Modified Orthotropic Thermal Conductivities

T(K)	K_x [W/m-K]	K_y [W/m-k]	K_z [W/m-k]
100	6.9093	3.1007	12.26
150	7.3887	3.3705	13.055
200	7.8623	3.6278	13.85
250	8.3329	3.8783	14.645
300	8.8007	4.1228	15.44
350	9.266	4.3618	16.235
400	9.7312	4.6005	17.03
450	10.194	4.835	17.825
500	10.657	5.0677	18.62
550	11.118	5.298	19.415
600	11.579	5.5259	20.21
650	12.038	5.7518	21.005
700	12.497	5.9765	21.8
750	12.955	6.1992	22.595
800	13.412	6.4209	23.39
850	13.869	6.6416	24.185
900	14.326	6.8631	24.98
950	14.783	7.0836	25.775
1000	15.241	7.305	26.57
1100	16.155	7.7474	28.16
1200	17.069	8.1894	29.75
1300	17.987	8.6391	31.34
1400	18.918	9.1175	32.93
1500	19.848	9.594	34.52
1600	20.766	10.045	36.11
1700	21.688	10.504	37.7
1800	22.61	10.962	39.29
1900	23.535	11.428	40.88
2000	24.463	11.901	42.47
2100	25.395	12.381	44.06
2200	26.336	12.883	45.65
2300	27.283	13.397	47.24
2400	28.248	13.948	48.83
2500	29.224	14.526	50.42
3000	34.331	17.911	58.37

Convergence Studies

The grid-independence of the simulation was established for both the fluid and solid domains through convergence studies. The fluid simulation was considered converged when both the total heat measured heat flux on the spider walls and the area-weighted average convection coefficient were found to change by less than 1% for a substantial increase in grid density. The transient thermal solution was considered converged when the maximum temperature at each probe location and average slope of the profile varied less than 1% between mesh levels. Presented in Table 9 are the convergence study data for the fluid domain. Presented in Table 10 are the convergence study data for the solid domain.

Table 9: Phase 3 Fluid Domain Convergence

Run	Nodes	Elements	Spider Sizing [in]	Other Sizing [in]	Total Spider Heat Flux [BTU/h]	Area Weighted Average h [BTU/h-ft^2-°F]	Max h [BTU/h-ft^2-°F]
1	19271	95715	0.050	0.050	25676.283	295.471	1155
2	41667	209658	0.035	0.035	29168.564	335.599	1222
3	55613	282519	0.025	0.035	31322.46	360.349	1533
4	169789	896683	0.020	0.020	31619.779	363.258	1533
5	217589	1512264	0.015	0.015	31687.427	364.525	1533

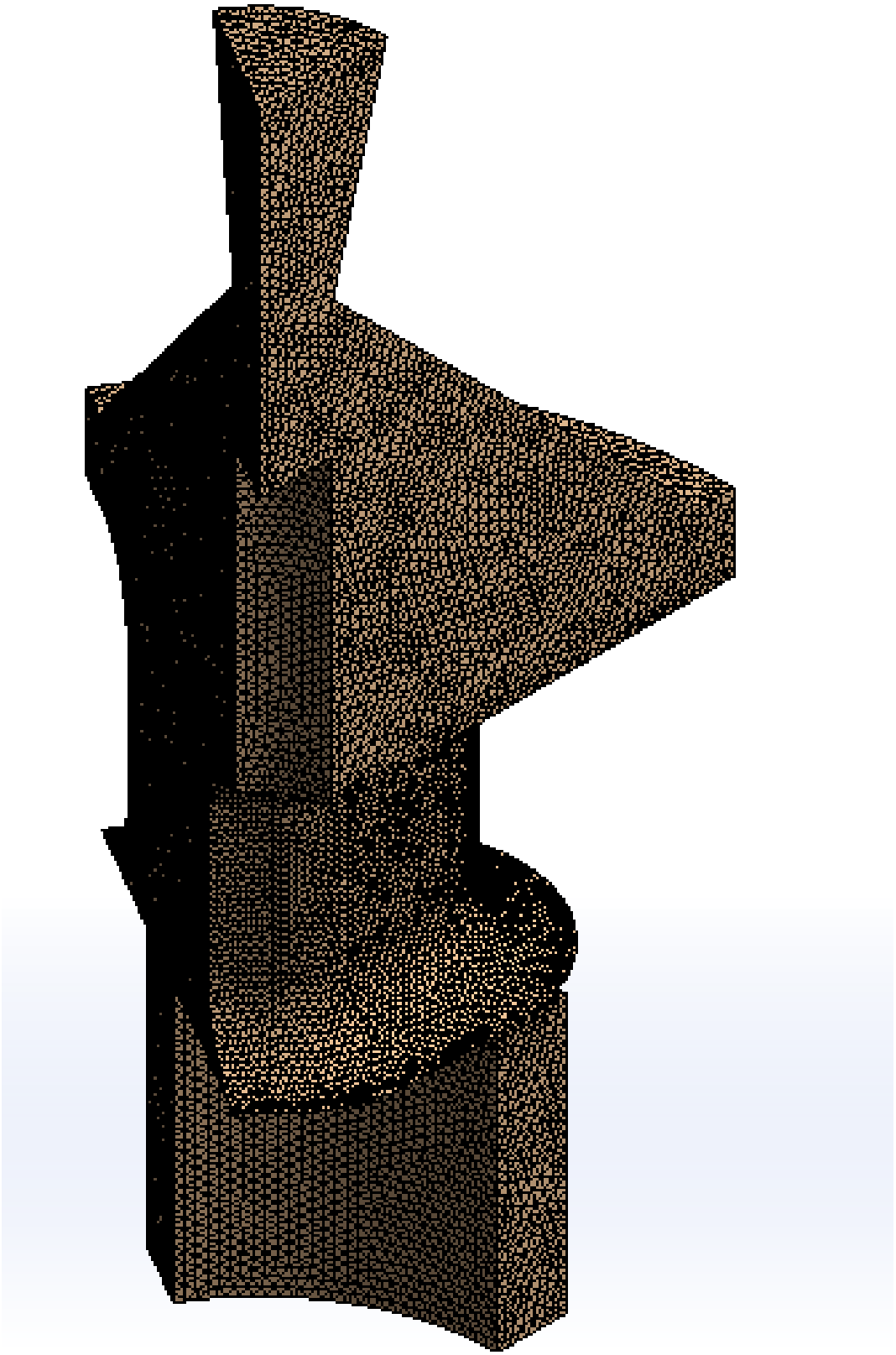

Figure 38: Fully Converged Fluid Domain Mesh, View 1

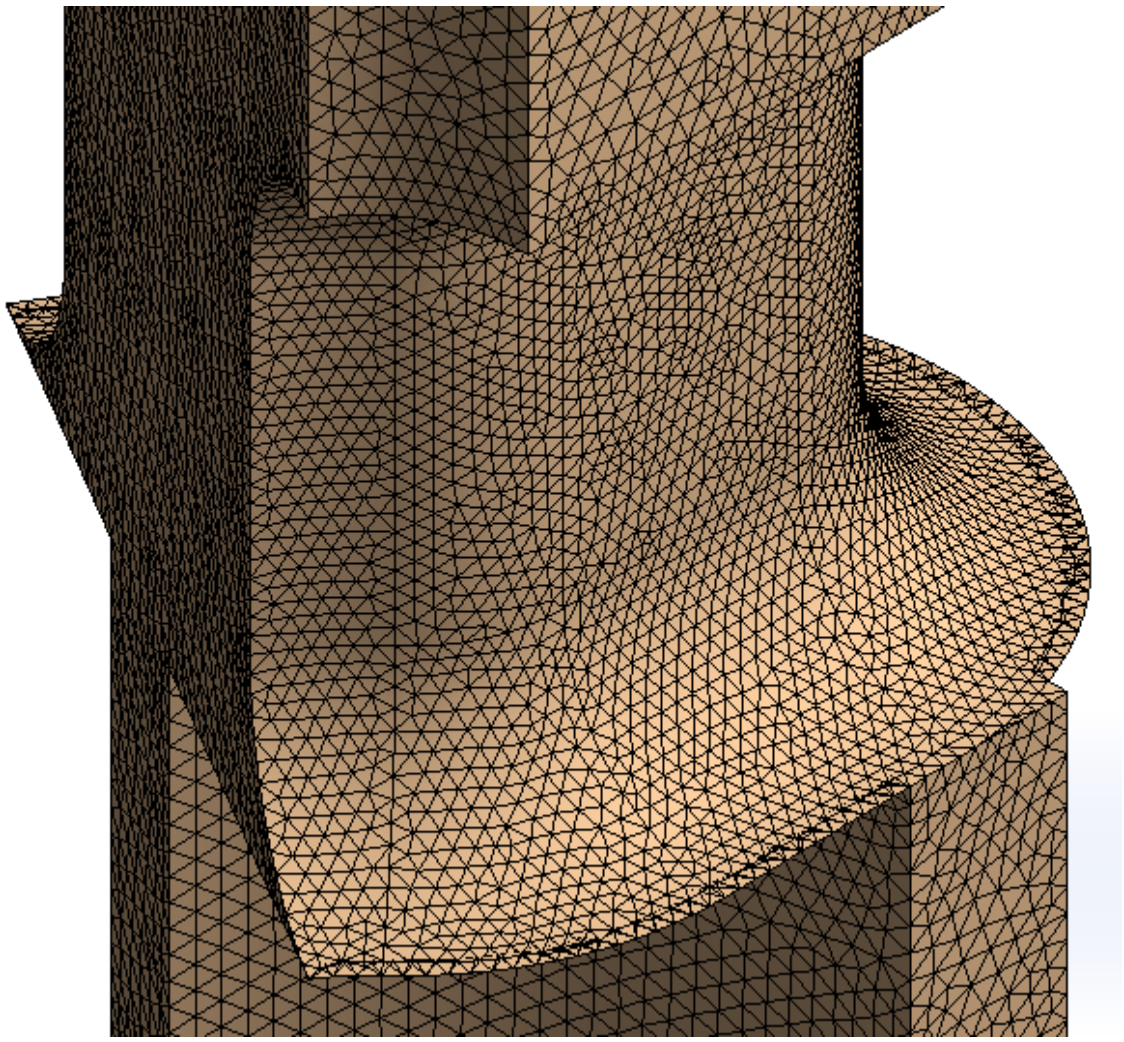

Figure 39: Fully Converged Fluid Domain Mesh, View 2

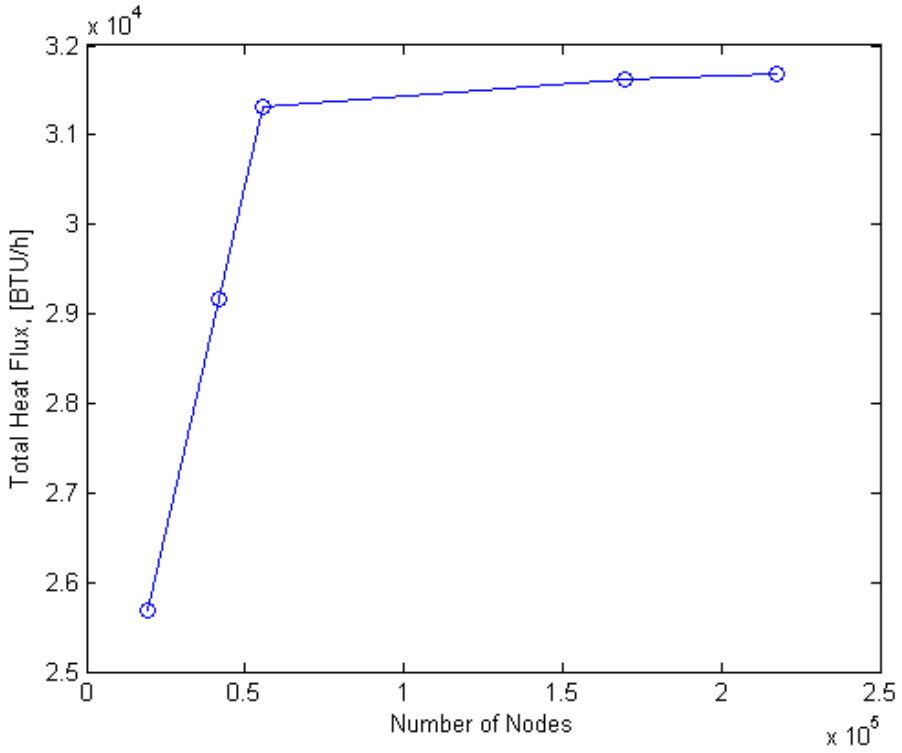

Figure 40: Fluid Domain Heat Flux Convergence Plot

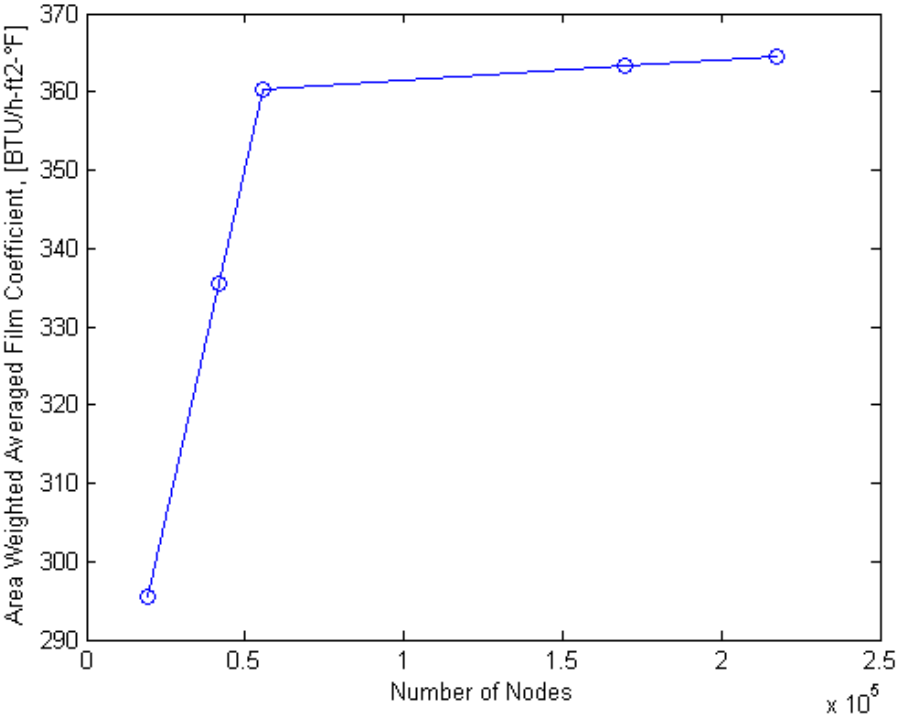

Figure 41: Fluid Domain Film Coefficient Convergence Plot

Table 10: Phase 3 Solid Domain Convergence

Run	Nodes*10^4	Elements	Sizing [in]	Tmax 1 [°F]	Tmax 2 [°F]	Tmax 3 [°F]
1	6.17	31155	5.00E-02	346.72	331.28	414.91
2	7.64	38946	4.50E-02	349.81	331.43	414.99
3	12.6	64080	3.50E-02	349.78	331.33	414.74

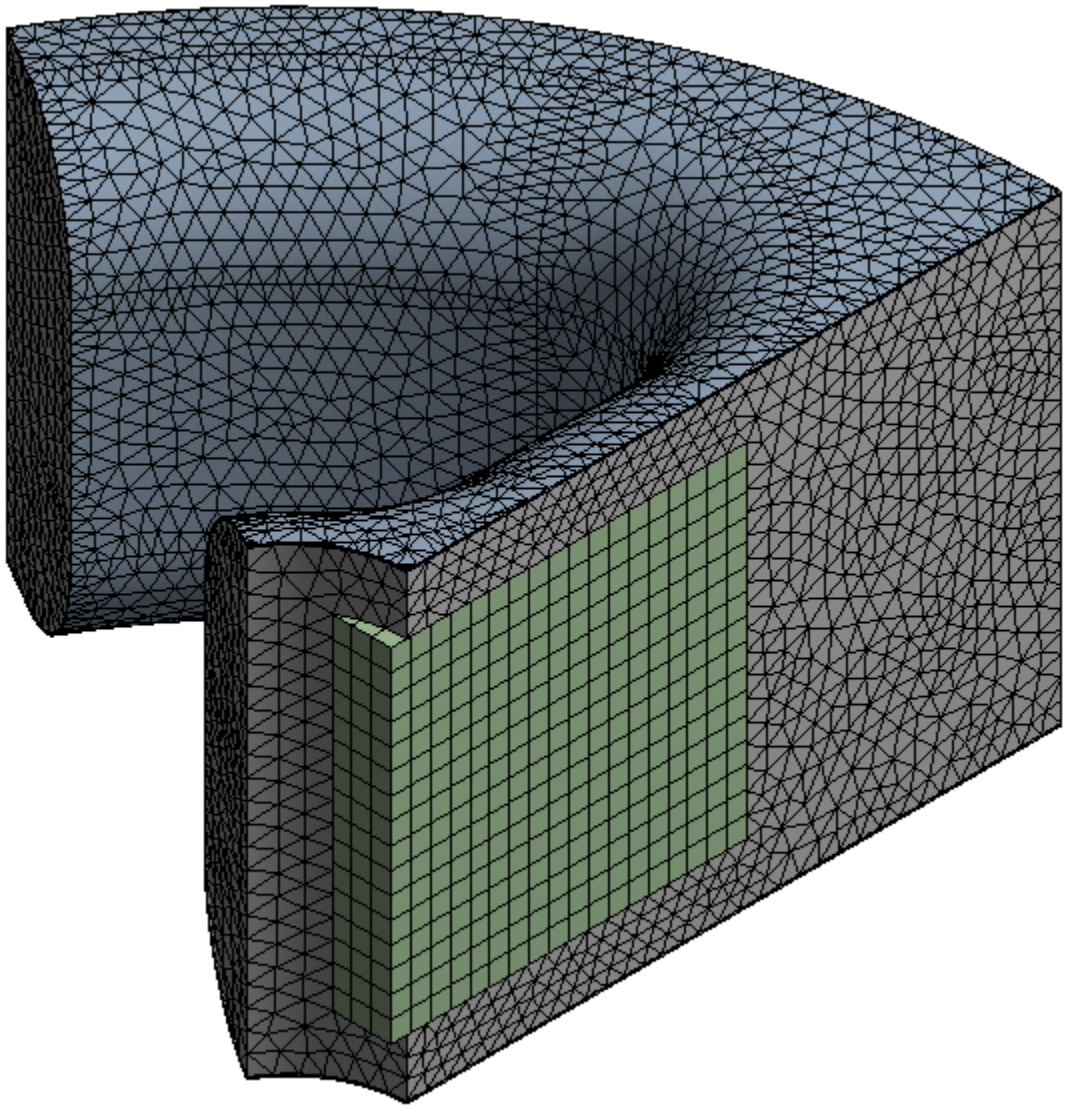

Figure 42: Converged Solid Domain Mesh, View 1

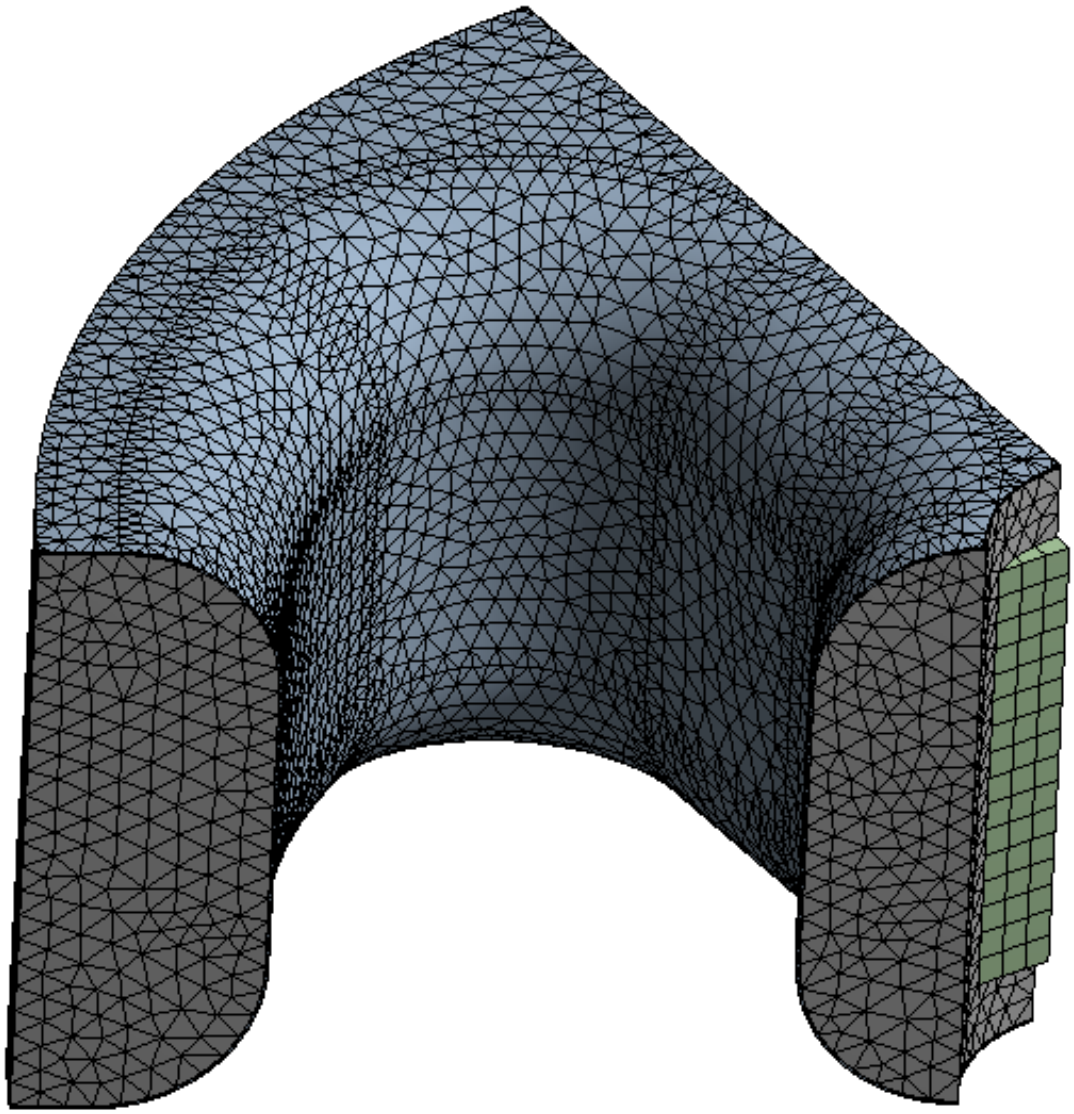

Figure 43: Converged Solid Domain Mesh, View 2

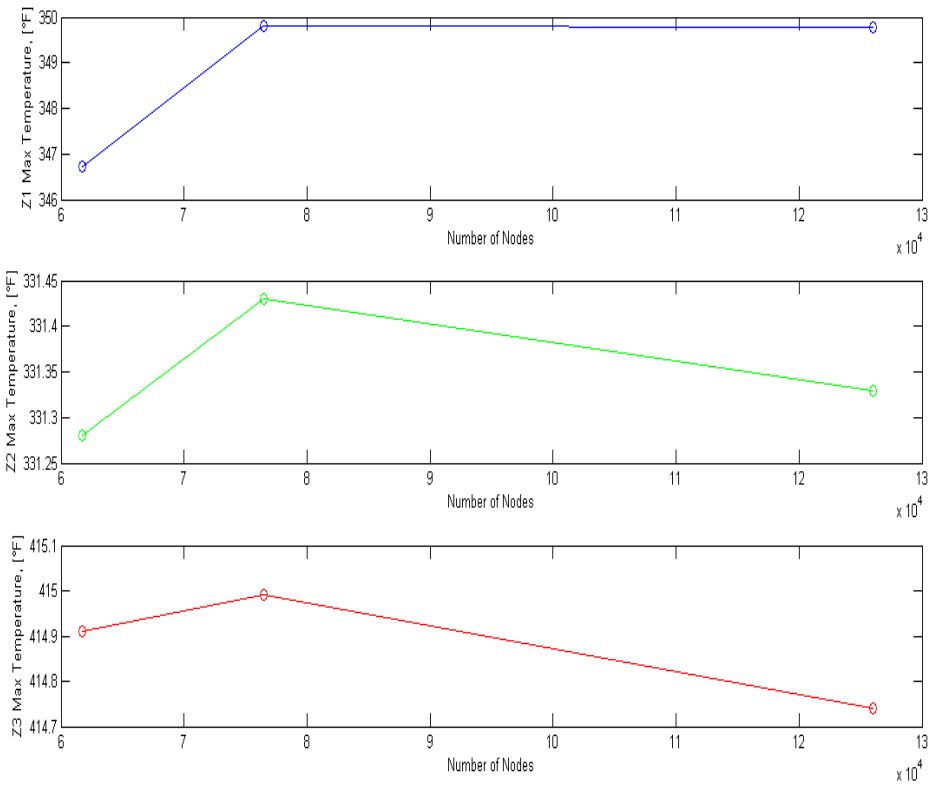

Figure 44: Solid Domain Temperature Convergence

Results

The FLUENT simulation was run until all iterations converged to within a maximum residual value of 10^{-6} for all solvers, and the transient thermal simulation was run for 10 seconds. The simulated temperatures were gathered and compared to experimental data as presented in Section VII.

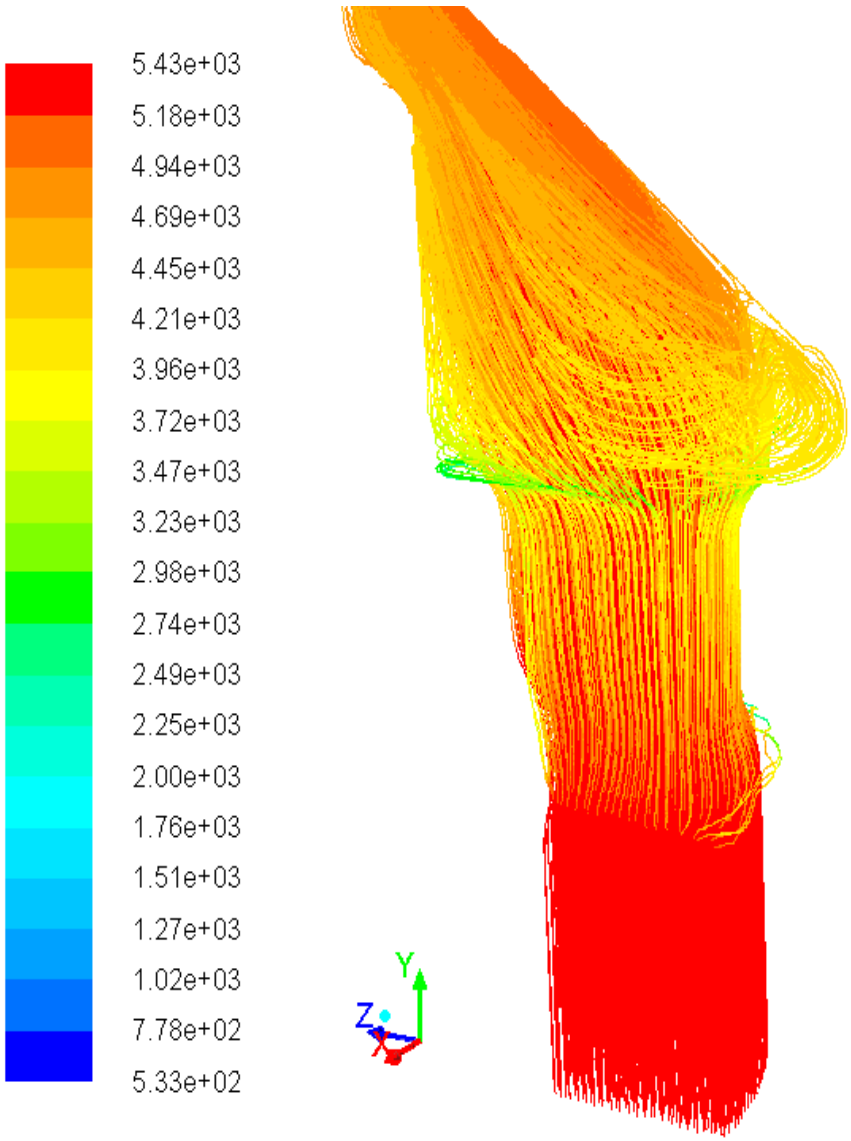

Figure 45: Fluid Domain Pathlines, Colored by Total Temperature [°R]

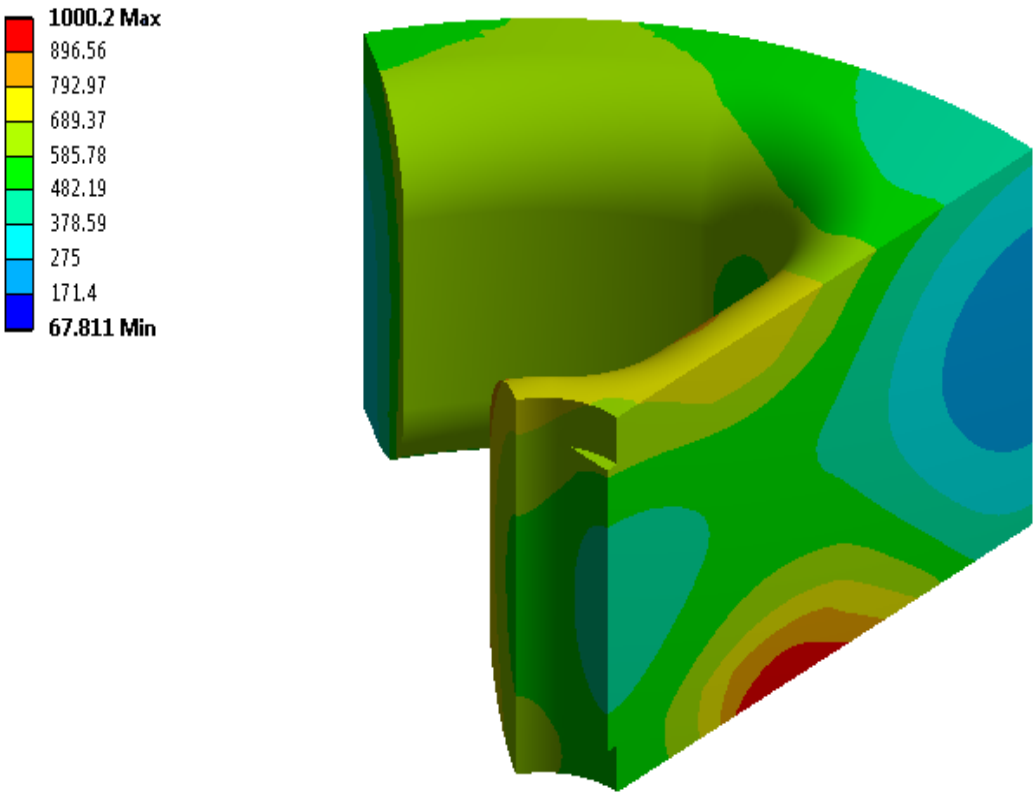

Figure 46: Solid Domain Temperature [°R] Distribution at t=10s.

Model Phase 3 Conclusion

A fully featured three-dimensional model was produced by extending upon the previous model phases. The effects of thermal contact resistance within the experimental apparatus as well as externally deposited soot were considered and implemented in the model. Convergence was achieved for both the fluid and solid domains, and the resulting model was used to simulate several testfires for comparison with experimentally acquired data, as presented in Section VII.

VI. EXPERIMENTAL VALIDATION

An experiment was designed to gather data for comparison against simulated results. Based on the results of the parametric study performed in Section IV, an iteration of the structural webbing with embedded thermocouple probes was manufactured and tested in three hotfire runs.

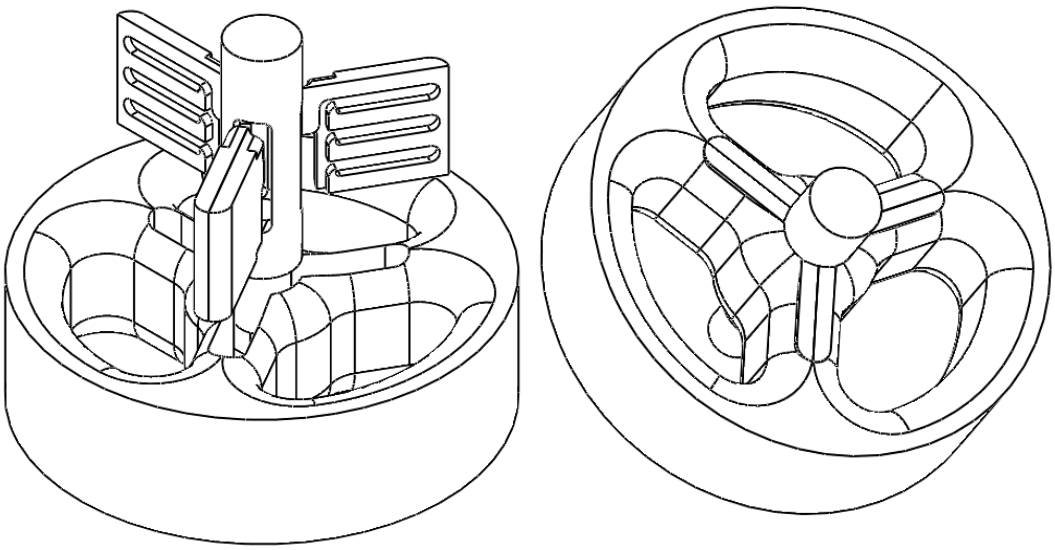

Figure 47: Experimental Rig Solid Model

Design

The primary goal of this design was to provide a platform for acquiring data to empirically validate the models presented in earlier sections. The design needed to be simple, directly relatable to an analytical model with a minimal margin of error, and producible using in-house manufacturing capabilities. In addition, the design needed to be sufficiently robust to survive a wide spectrum of test conditions without compromising measurement validity or device structural integrity.

The results of the parametric study indicated that for an uncooled device, part life is best improved by maximizing the local ratio of available thermal capacitance to exposed surface area, especially near the leading edge where heat flux is greatest. A rounded or “snub-nose” cross-section was chosen to take advantage of this relationship. The manufacturability of the device

was likewise improved by this selection. Cutting a constant-radius profile accurately and with good surface finish on the leading and trailing edges is easily accomplished using a corner-rounding end mill, as opposed to a variable radius which would require the use of a ball end mill and a stepover scheme, which would be slightly more time-intensive.

The material of choice for all manufactured parts was selected as 304 stainless steel. Although 304 stainless has a lower thermal conductivity (and is therefore more prone to melting near the leading edge) and is less machinable than plain carbon steel, it offers several advantages. First, this material is corrosion and rust resistant, making long-term storage easy and simple, and reducing the likelihood of the caustic exhaust causing chemical damage during a testfire. Second, 304 stainless is the same material that will likely be used in the actively cooled device iteration, and while the intended model validation was not necessarily dependent on use of identical materials, the improved similarity will likely improve the ease of model extensibility to the analysis of the cooled device. Plain carbon steel might be more suited to the application as the higher thermal conductivity makes carbon steel more capable of conducting heat away from the surface where thermal failure is more likely. However, early analyses indicated that using carbon steel would preserve the device body but result in destruction of the thermocouples probes, whose operating range is cut off below the melting temperature of the carbon steel considered. By selecting a slightly less conductive material, the instrumentation is preserved such that the surface overheating is more likely to be the primary mode of failure. Finally, though 303 stainless steel might be selected over 304 stainless for its improved machinability and ease of use, the sulfur in 303 makes it more difficult to weld. Welding the device components together is necessary in order to seal the device and prevent the potentially catastrophic intrusion of exhaust. The downsides of 304, namely a lack of machinability and tendency to gall when threaded, were deemed negligible in comparison to the numerous advantages, and 304 stainless was thusly selected.

Probe Design

K-Type BLMI thermocouple probes, 0.125" in diameter, were selected to protect te thermocouple junctions, allowing for temperature measurements nearer the melting point of steel. Using probes removed the need to weld thermocouple junctions directly to the part, and helped ensure junction quality and location certainty[38]. The instrumented spider featured three sets of three thermocouples placed in sequence along the midline of each spoke. The 24 AWG probe leads were welded to 4' of duplex-insulated 30 AWG wire. The outer insulation was stripped from the 30AWG wire nearest the probes, and non-fray fiberglass sleeving was slid over the junction and bare lead to prevent shorts and reduce the likelihood of wire fusion or destruction during welding.

Cartridge Design

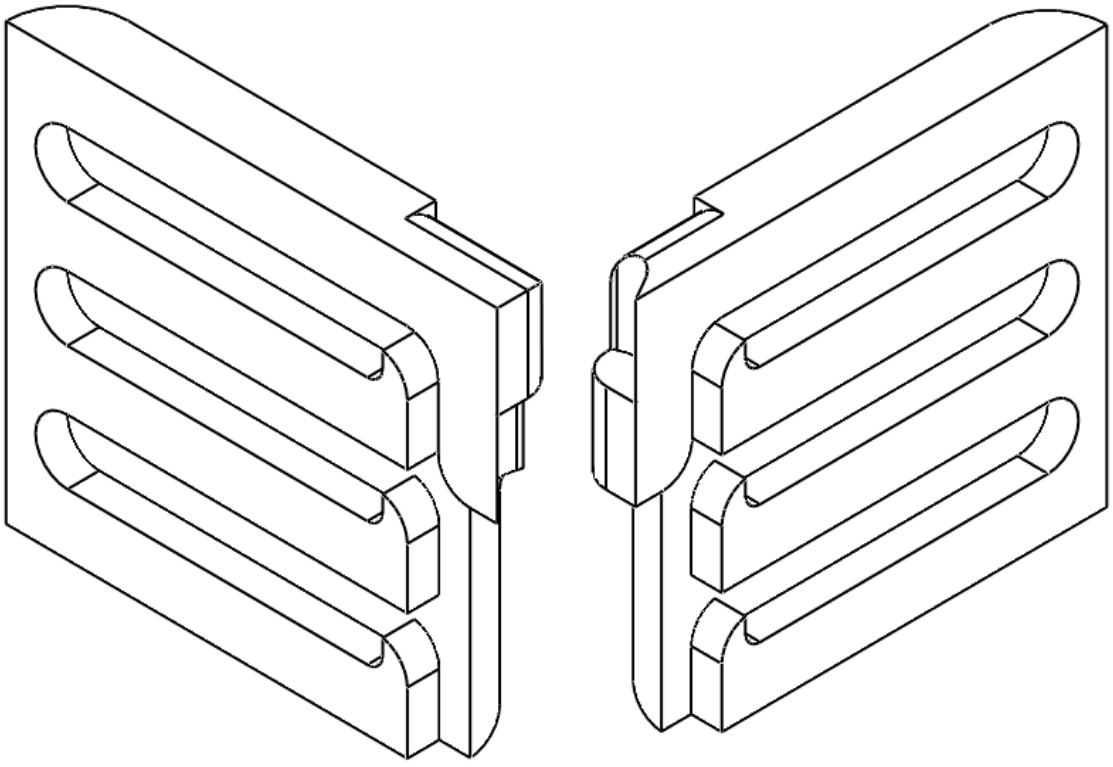

Figure 48: Thermocouple Cartridges

The thermocouple cartridges, shown in Figure 48, were designed to allow the probes to be accurately located within the structural webbing. The three axially spaced channels were

specified for a light press fit. Though this interference increases the difficulty of assembling the finished device, using an interference fit makes adhesives unnecessary and minimizes the removed thermal capacitance associated with removing material for a clearance fit. The minimization of removed thermal capacitance is important for measurement accuracy, as removing material from the device drastically alters the temperature gradient that develops within it. Uncertainty in device thermal capacitance respect can lessen the validity of the simulated model, which relies heavily on accurately and precisely representing the finished geometry.

The distal edge of each cartridge had a 0.125" radius to facilitate placement within the structural webbing. On the proximal edge, there were two 0.0625" fillets on the top and bottom which facilitated placement within the rounded center channel pockets. The proximal edge of each cartridge also had two locating features, an extrusion and an external pocket, which allowed the full six-cartridge assembly to seamlessly interlock as shown in Figure 49. The design of these interlocking features made it possible to snugly fit the entire assembly together, including the spider body and the center channel, with only a single clamping point, which provided for easier welding access.

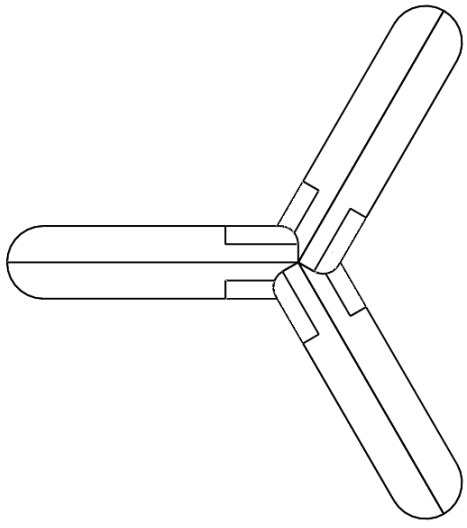

Figure 49: Interlocked Cartridges, Top View

Spider Design

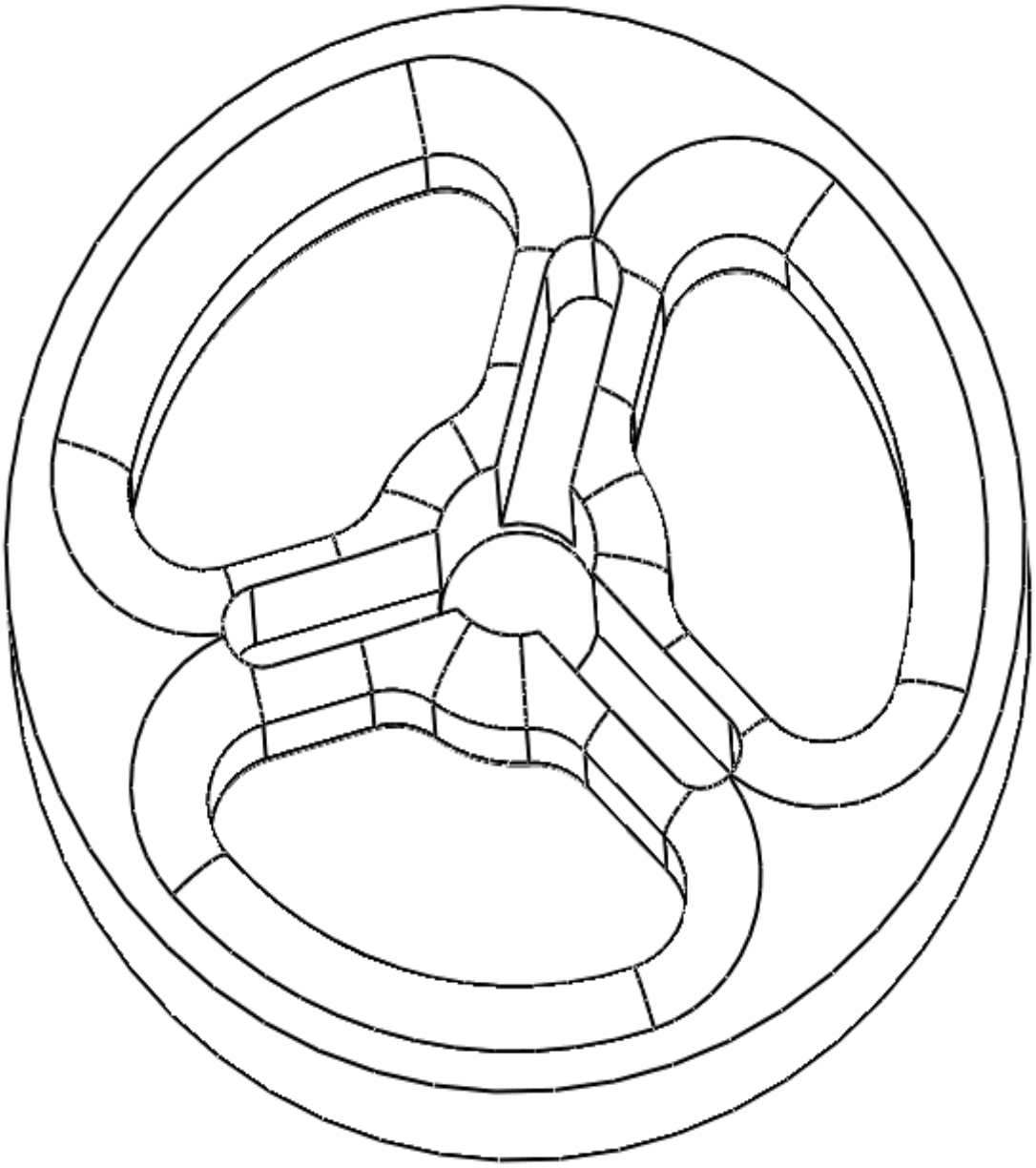

Figure 50: Structural Webbing for Empirical Validation

This iteration of the main structural webbing body was designed primarily to house the thermocouple cartridges. The webbing featured a three-spoke snub-nose configuration, with a 1" axial length, 0.5" spoke thickness, and 0.25" fillet radius. Each of the spokes had a milled channel into which the probe cartridges were inserted.

Partial Center Channel Design

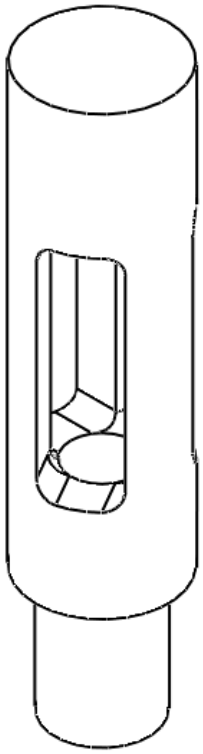

Figure 51: Partial Center Channel

The partial center channel was the centerpiece of the assembly, housing and locating the inner edges of the probe cartridges and acting as the conduit through which the thermocouple wires were run. The upper edge of the center channel extended 0.75" beyond the trailing edge of the spider with the goal of keeping the nearby downstream flow profile similar to that which would be observed if an aerospike were actually present. The lower step had a 0.375"-24 external thread which screwed into the primary center channel.

Manufacture

The experimental apparatus was produced using a Clausing manual lathe, a Haas TL-1 CNC lathe, and a Haas TM-1 CNC mill with a 4^{th} and 5^{th} axis rotary table.

Cartridge Manufacture

As shown in Figure 52, the inward-facing cartridge features were first milled out of a single billet of 304 stainless steel. A total of eight cartridges were produced: the six required, as well as a backup pair. A 0.125" and 0.0625" carbide end mill were used to cut the channel features, and a 0.25" end mill was used to cut the perimeters.

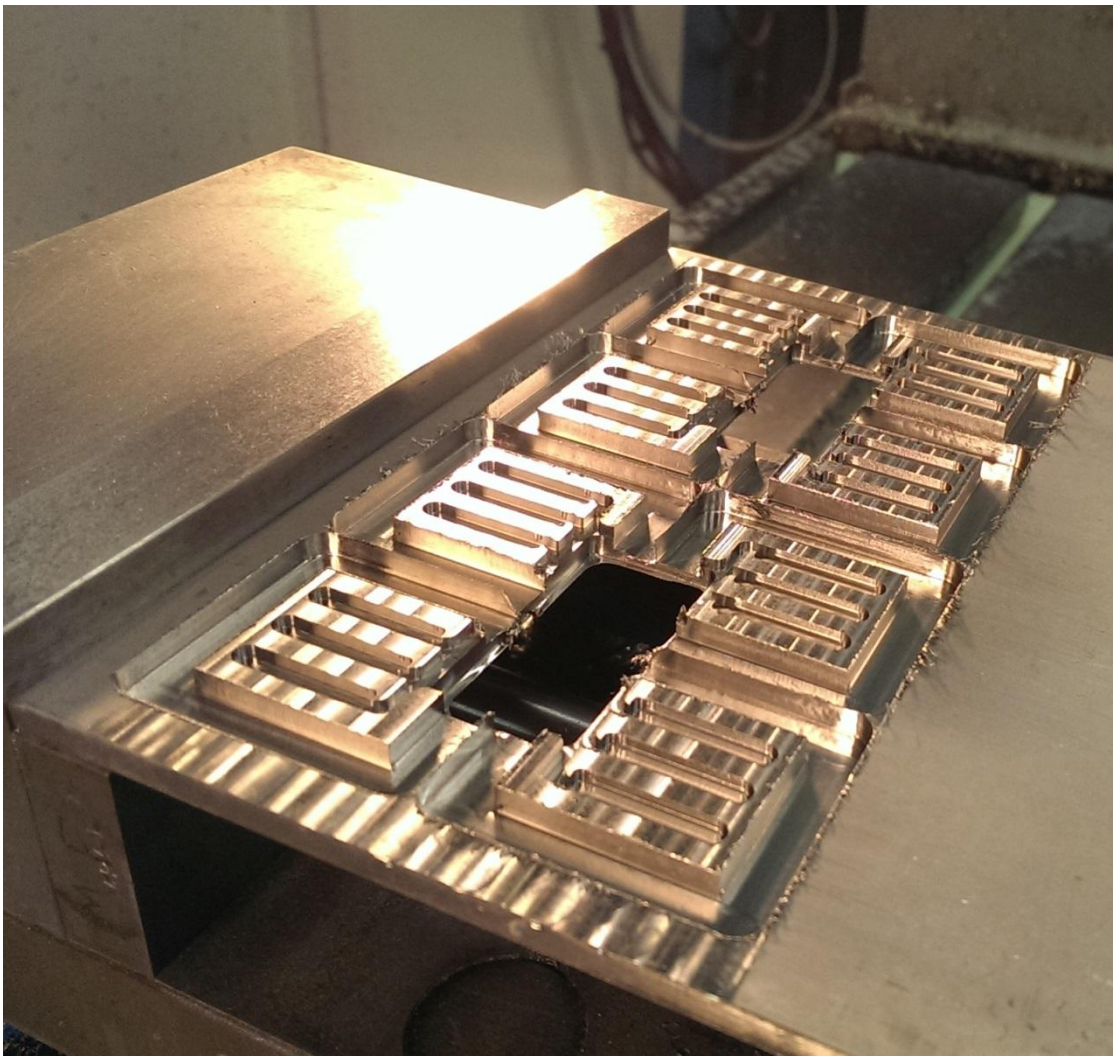

Figure 52: Thermocouple Cartridges, Setup 1

The cartridges were then individually freed from the billet on a horizontal bandsaw, and the excess material removed in the mill. Using two corner rounding end mills, the clearance and locating fillets were milled into each cartridge. Finally, the locating pockets were cut using a 0.125" end mill.

Spider Manufacture

The spider was turned and faced to finish length and OD from 3.5" 304 round bar stock. Aluminum soft jaws were milled to enable rigid fixturing of the round stock. In addition to the round pocket, a hole for a dowel pin was drilled into the soft jaws such that the spider could be angularly located for the second setup.

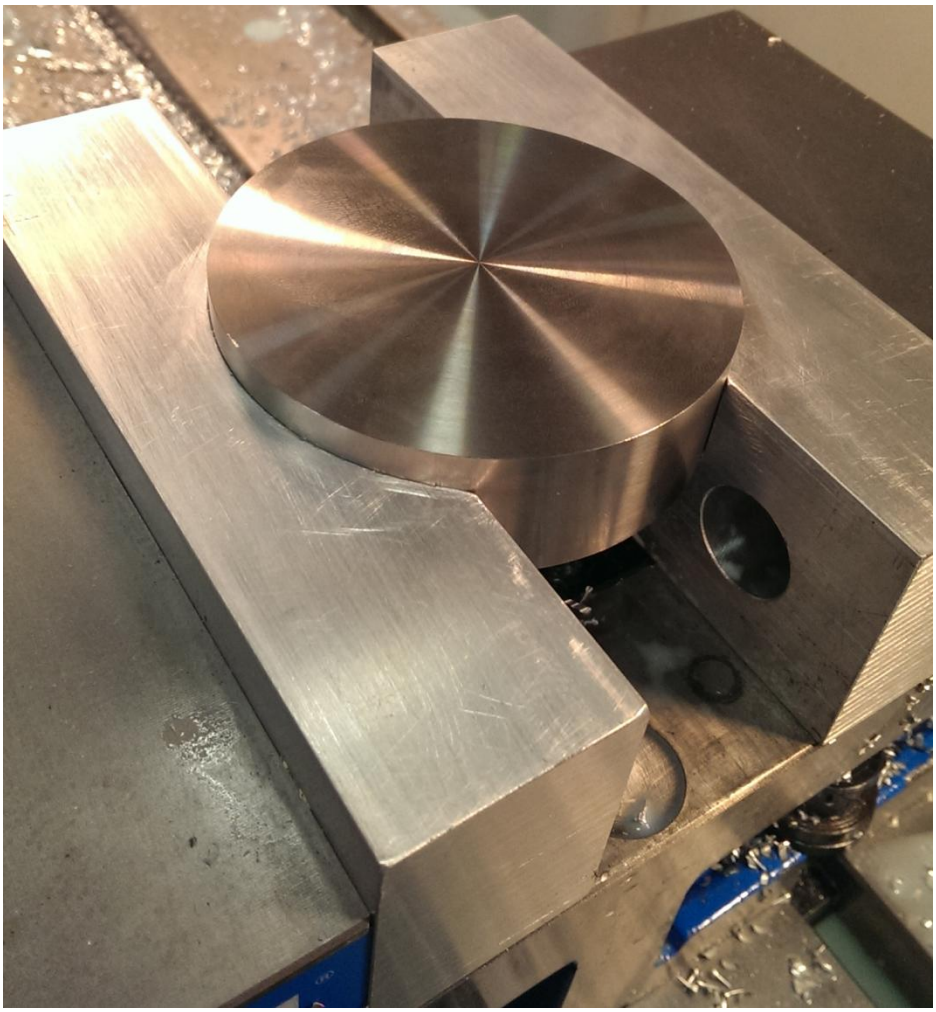

Figure 53: Spider Stock in Soft Jaws

First, three rounded pockets were milled through the body of the webbing. Then, a corner-rounding end mill was used to cut the constant radius fillet of each pocket, and a drill mill was used to drill the central through hole. Last, taking advantage of the through hole to make plunging unnecessary, the spoke-wise pockets were milled, and the completed cartridges inserted to ensure compatibility. Step-by-step progress of this first setup is shown in Figure 54.

Figure 54: Spider Setup 1

For the second setup, a dowel pin was inserted into the previously drilled hole, and used to locate the spider. Then, repeating the second step of the first setup, a corner rounding end mill was used to cut the leading edge fillets of each pocket.

Figure 55: Spider Setup 2

Partial Center Channel Manufacture

For the partial center channel, the outer diameters and central pocket were cut and drilled from 0.625" round stock, as shown in Figure 56. Then, the three intersecting pockets were milled using the 4^{th}-5^{th} axis rotary table.

Figure 56: Partial Center Channel, Turned and Reamed

Finally, the external threads were cut via the canned single-point threading cycle on the TL-1, as shown in Figure 57.

Figure 57: Partial Center Channel, Single Point Threading

Compatibility with the cartridges and webbing was confirmed by assembling the apparatus without the thermocouple probes.

Figure 58: Experimental Rig, Assembled without Probes

Probe Manufacture

The instrumentation was designed to consist of a 0.125" BLMI K-type thermocouple probe, welded to 30-gauge duplex insulated wire, with non-fray fiberglass sleeving fitted over the welds

to shield the bare leads from undesired fusing. The wires were welded using a Hughes Aircraft HRW-100B spot welder.

Figure 59: Thermocouple Probe with Duplex Insulated Wire

The completed instruments were labeled and inserted into the partial center channel. The thermocouple cartridges were then pressed onto the probes and slid inwards, making use of the locating features to ensure accurate placement.

Figure 60: Partially Assembled Instrumentation

Upon successful pressing of the cartridges over the nine probes, the complete device was assembled, as shown in Figure 61.

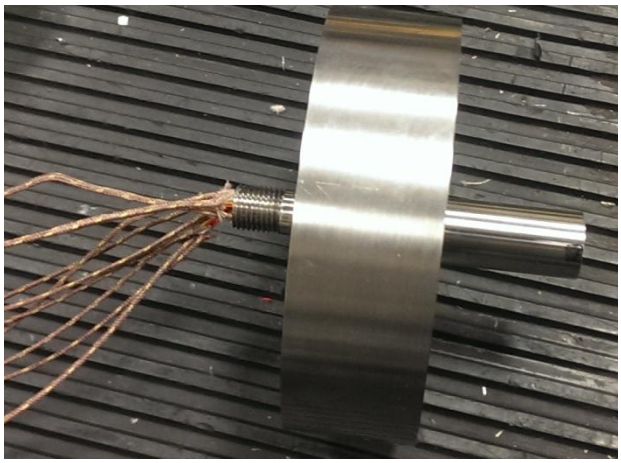

Figure 61: Assembled Test Rig

Welding and Heat-Shrink Tubing

The full assembly was TIG welded, as shown in Figure 62, to provide structural integrity and to seal against exhaust flow. The cartridges were designed to extrude slightly above the upper radius of the spider; this extra lip of material was left to allow the cartridges to be fusion welded into the webbing without the need for filler metal. In addition to the fusion welding, a ring of filler metal was welded around the interface between to the webbing and the center channel to seal this interface. This filler ring was repeated on the underside of the device.

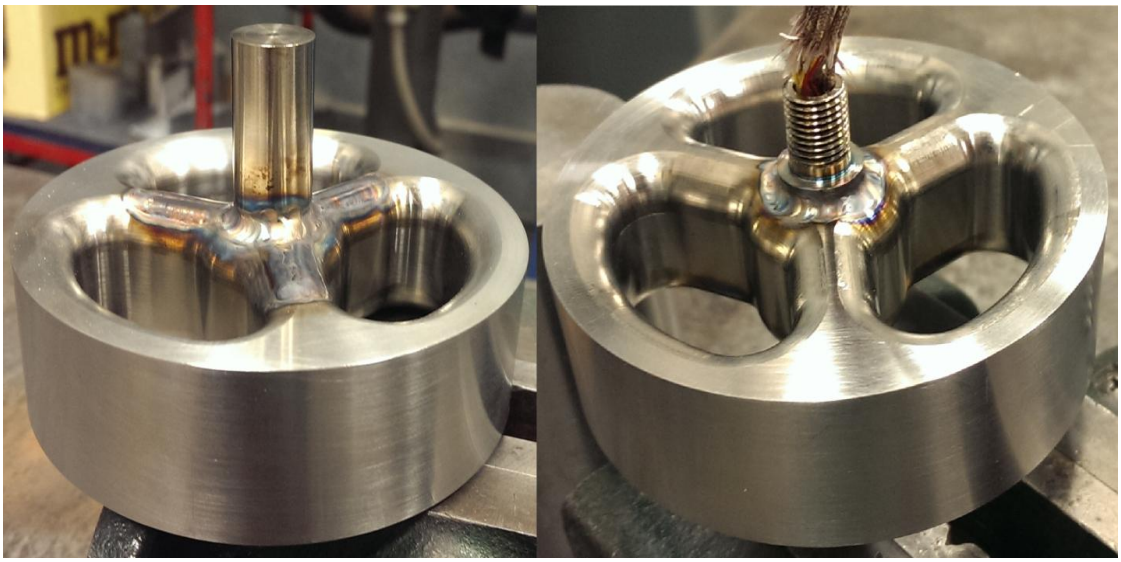

Figure 62: Test Rig Welding

High-temperature high-rigidity PTFE heat-shrink tubing was fitted into the partial center channel in order to strain relieve the wires, then flame-retardant polyefin heat-shrink was shrunk onto the rest of the wires, as shown in Figure 63.

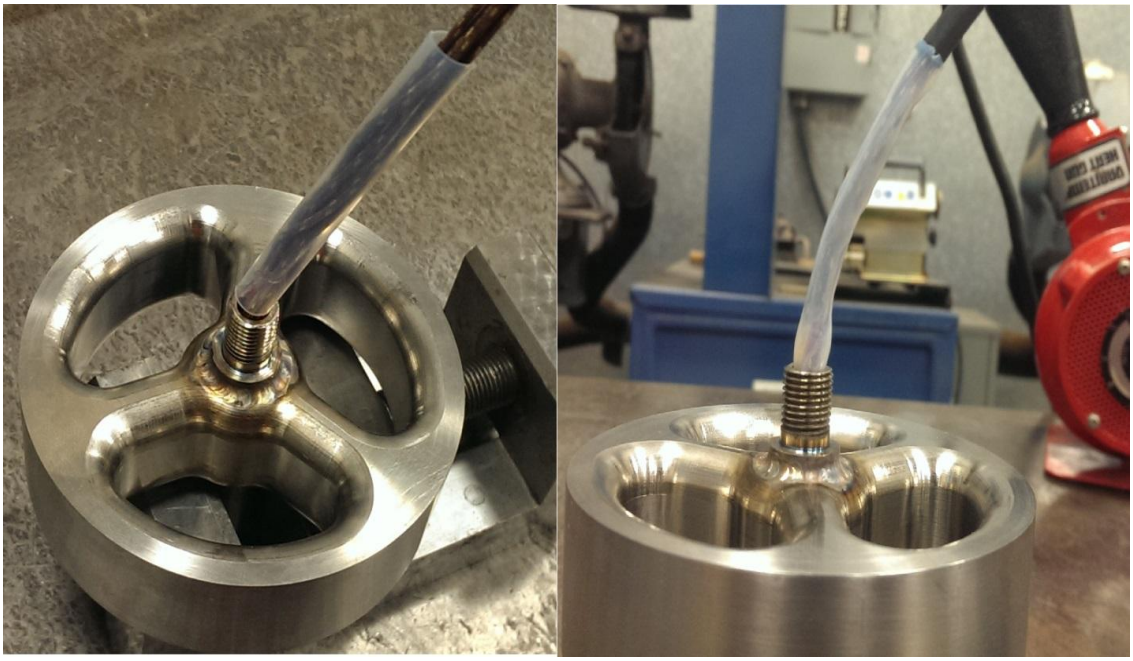

Figure 63: Heat-Shrink Tubing

Lastly, the threads were coated with lubricant to prevent galling, and the custom-made center channel was fitted over the bundled wires, as shown in Figure 64. The inner diameter of the inner fuel grain was chamfered to account for the fillet welds and loaded on top of the device.

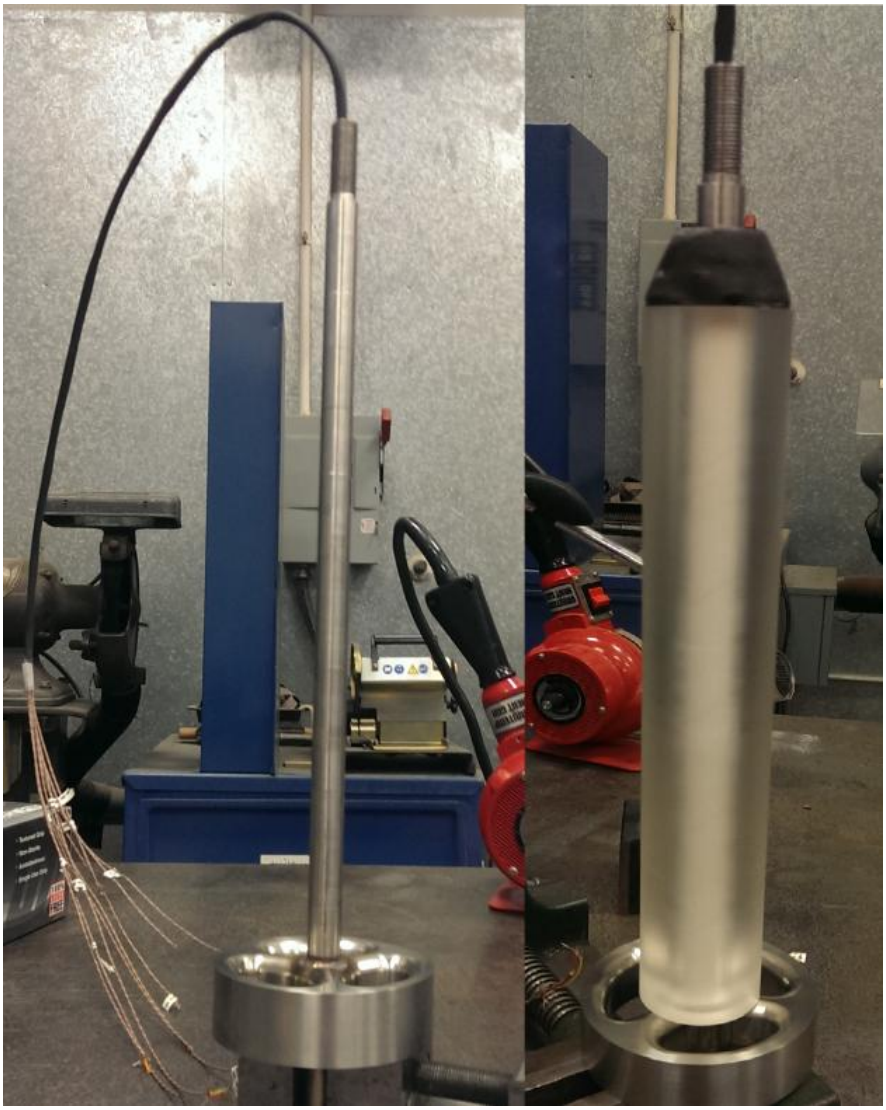

Figure 64: Assembled Apparatus

Test Runs

The experimental rig was subjected to three hotfire tests in the Cal Poly Labscale Hybrid Rocket Test facility. Temperature, pressure, and oxidizer mass flowrate data was gathered using the ADAM 5000 data acquisition system and ADAMVIEW software. The embedded thermocouples were connected to the custom-made thermocouple amplifier boards shown in Figure 66.

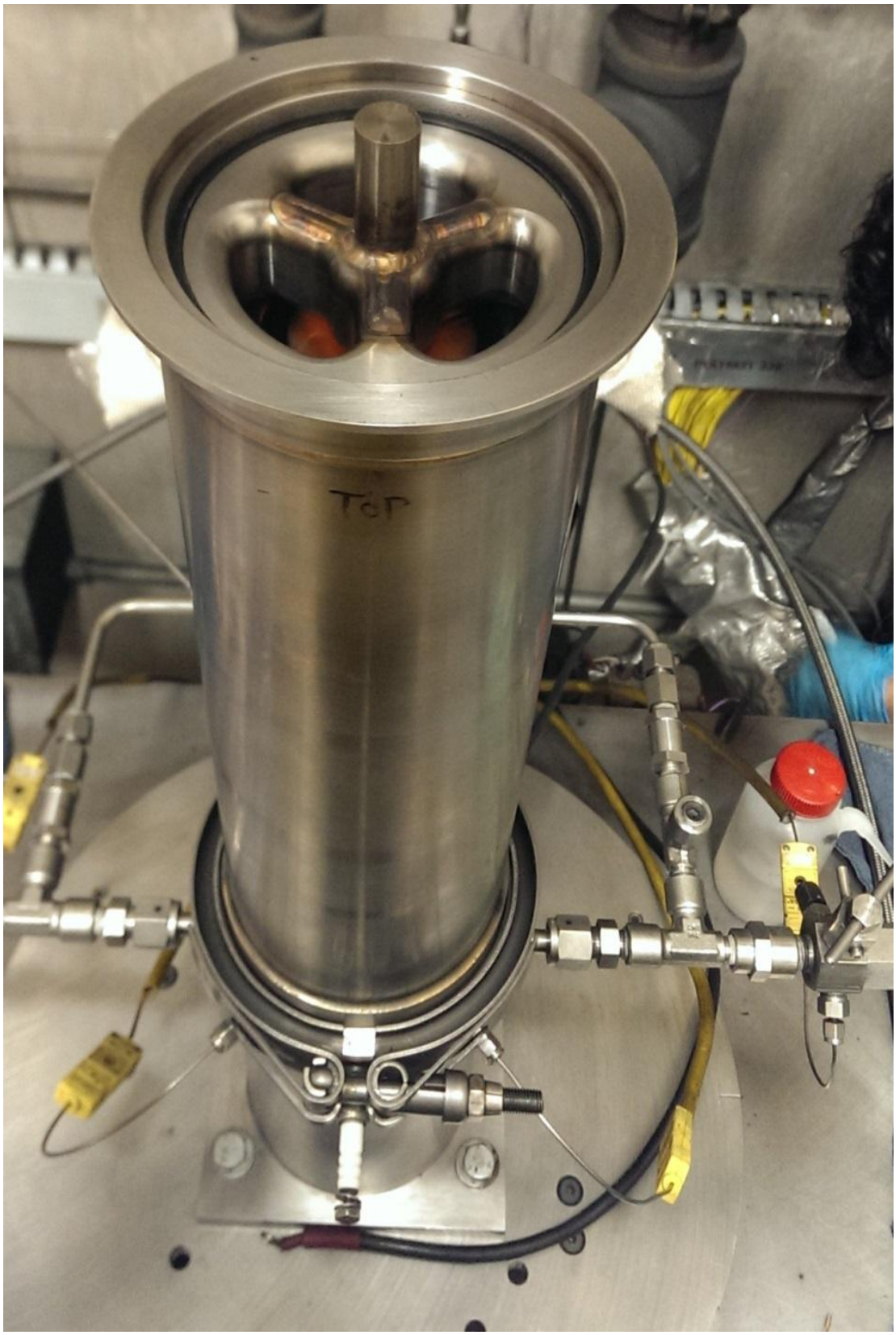

Figure 65: Experimental Apparatus, Mounted

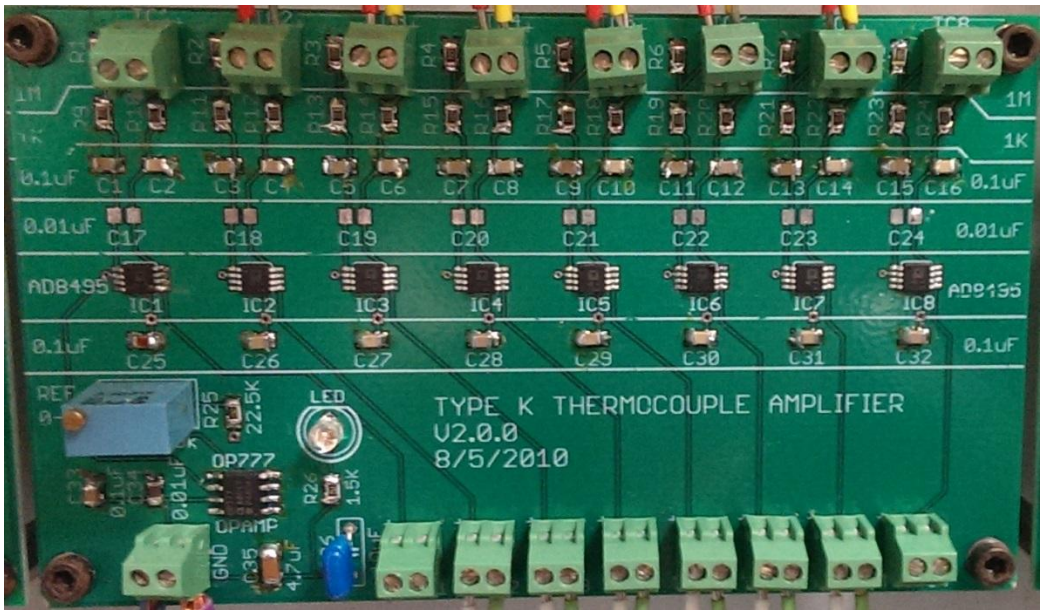

Figure 66: Thermocouple Amplifier Board

The first test run, Hotfire 103, was conducted on December 12th, 2014, and made use of four 0.025" diameter injectors. The second run and third runs, conducted on January 14th and 16th, each used six 0.025" diameter injectors. All three burns lasted for six seconds. An explanation of the design of the oxidizer delivery system can be found in previous Cal Poly theses[4]-[9].

Figure 67: Injector Configuration for Run 103

Each run began with a pre-ignition phase, shown in Figure 68, where propane and oxygen were used to ignite the grain. During Run 103, the pre-ignition flame was not visible, an effect which was not previously unobserved but the direct causes of which are not presently known with absolute certainty.

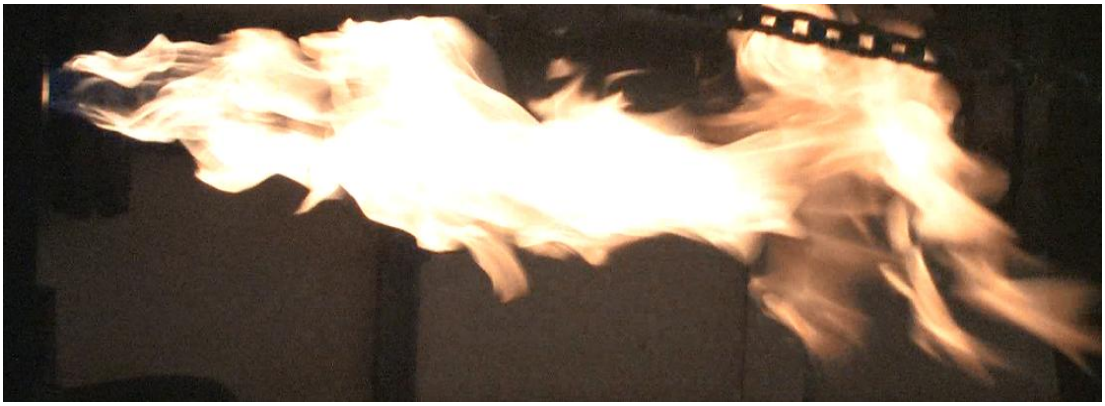

Figure 68: Rocket Pre-Ignition Flame, approximately 22"

Once the grain was lit, the nitrous oxide was flowed and the propane and oxygen flows were cut, beginning the actual testfire. Each testfire began with a transient portion, before the flow was fully developed, where unsteady effects were most observable. The most interesting transient effect that appeared to be specific to the spider was the tendency of the flame to exhaust in diagonal directions, presumably as flow through one sector of the spider dominated the other two and gave rise to greater mass flux in one direction. The transient flow is shown in Figure 69. Once the flow became fully developed, it entered the steady-state regime as shown in Figure 70. The simulated results are only compared to the results gathered during the steady-state period.

Figure 69: Hotfire 105 Transient Period, Exhaust Changing Directions

Figure 70: Hotfire 105 Exhaust. Flame approximately 18"

During each burn, the spider was covered in a layer of soot as a result of the incomplete and fuel-rich combustion regime. This soot provided a layer of insulation, shielding the device from the extreme environmental heat load. Though the spider suffered some discoloration as a result of this exposure, the structural integrity of the device and the instrumentation was not observably compromised throughout the course of testing.

Figure 71: Spider after Run 103, View 1

Figure 72: Spider After Run 103, View 2

Between each run, the fuel grains were weighed and compared to the weight of the nitrous oxide flowed during the test. The current experimental setup does not make real-time fuel regression rates available, and oxidizer flowrates are measured by comparing the weight of the supply bottles before and after the run with 0.5 lbm resolution. As such, the calculated O/F ratios suffer from a significant amount of uncertainty and can only be known as a bulk, "total-run" value. This limits the possibility of performing transient fluid analyses, as the time-varying boundary conditions are not accurately known—the use of static fluid analyses can be seen to reflect the instrumentation available.

Experimental Validation Conclusion

An experimental iteration of the structural webbing was designed, manufactured, and subjected to a series of hotfire tests. Experimental data were gathered for comparison against simulations.

VII. RESULTS

The experimental results were assembled and processed using MATLAB. Using the boundary conditions calculated by NASA-CEA with the measured oxidizer-fuel ratios and chamber pressures, and the fluid domain geometries based on the measured fuel geometries between runs, three simulation runs were performed. The simulated temperatures were compared to the experimentally measured temperatures. The flow parameters for each test are given in Table 11.

Table 11: Experimental Flow Parameters

Test Number	Burn Time [s]	O/F Ratio	Injector Config	Mean Chamber Pressure [Psia]	Mean Chamber Temp[°F]
103	6	2.3411	4 x 0.025"	157.6	4017.7
105	6	3.4611	6 x 0.025"	148.0	5007.4
106	6	3.3166	6 x 0.025"	172.2	4961.008

The measured temperature data gathered from the hotfire tests are presented in Figure 73 through Figure 90. The displayed temperature distribution is indicative of the filtering effects of the thermal capacitance that lies between the surface temperature and the measured temperature. Though the surface temperature is assumed to have a significant amount of high-frequency variation, as suggested by the measured pre-chamber pressure and temperature profiles as well as prior experience, the measured internal temperatures follow a smooth profile over the course of at least sixty seconds, significantly longer than the test duration. Additionally, the probes do not reach their maximum observed temperature until nearly a minute after the primary heat source is removed. Though this might be attributed to the heat convected to the device during the hotfire requiring time to “soak” through to the probes, simulations indicate that removing the heat source at the conclusion of the burn will result in an almost immediate decrease in temperature, suggesting that the surface of the device does not begin to cool immediately after the run concludes. Instead, the gas remaining in the chamber is still hot enough to cause heat to flow into the apparatus, though this convective flux is of much lower magnitude than that of the exhaust flow. The heat flows more slowly (relative to the duration of the burn) through the device, and

thus requires a long time to pass through the innermost section of the webbing where the instrumentation resides.

Shown in Figure 73 through Figure 90 are the experimental results compared to the Model Phase 3 results. For each run, the simulated temperature at the location of the thermocouple junction is compared to the mean of the three spoke-wise temperatures measured at each of the three axial locations. The error between the simulated and experimental results is given as the measured temperatures subtracted from the simulated temperatures at each timestep. Linear interpolation is used to ensure that the experimental results are locked to the same timestep as the simulated results. A quantitative examination of the errors is presented in Tables 12 through 14. A comparison of the mean time rate of temperature change, calculated using a cubic polynomial fit, is presented in Tables 15 through 17.

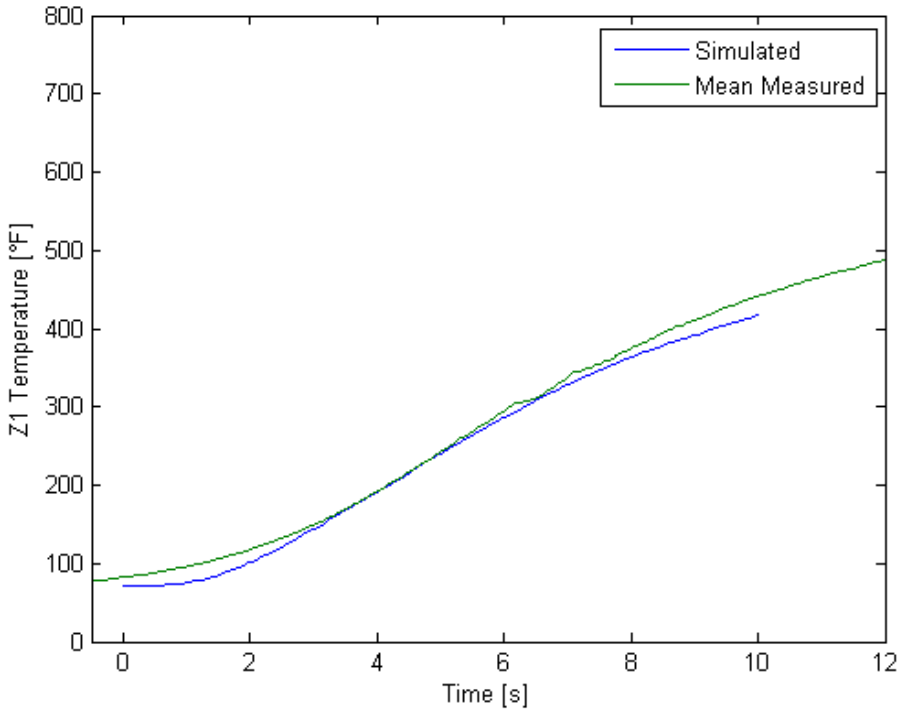

Figure 73: Run 103 Temperature at Axial Station 1

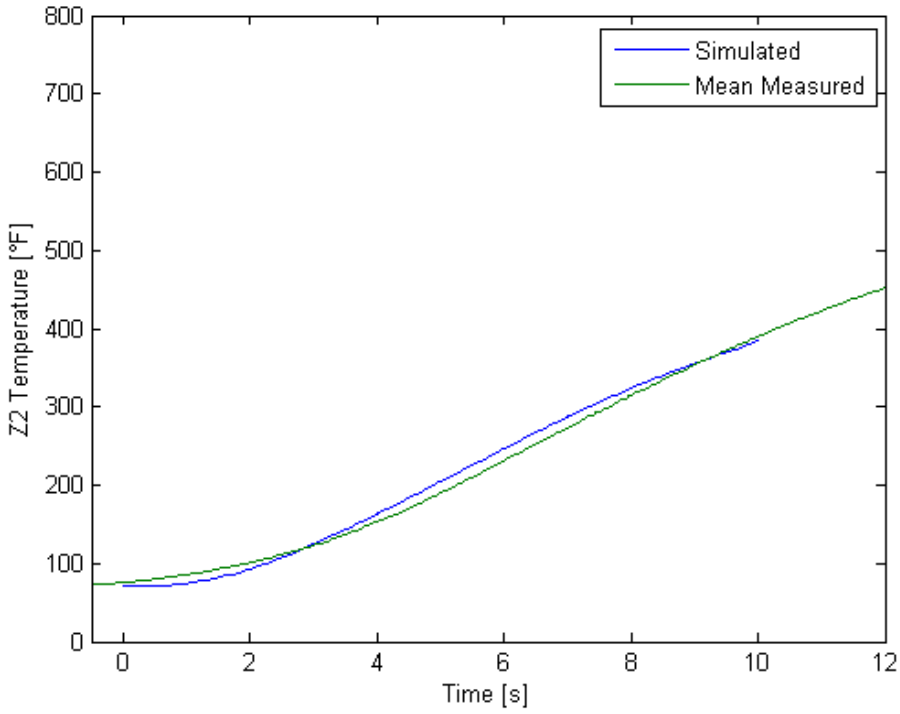

Figure 74: Run 103 Temperature at Axial Station 2

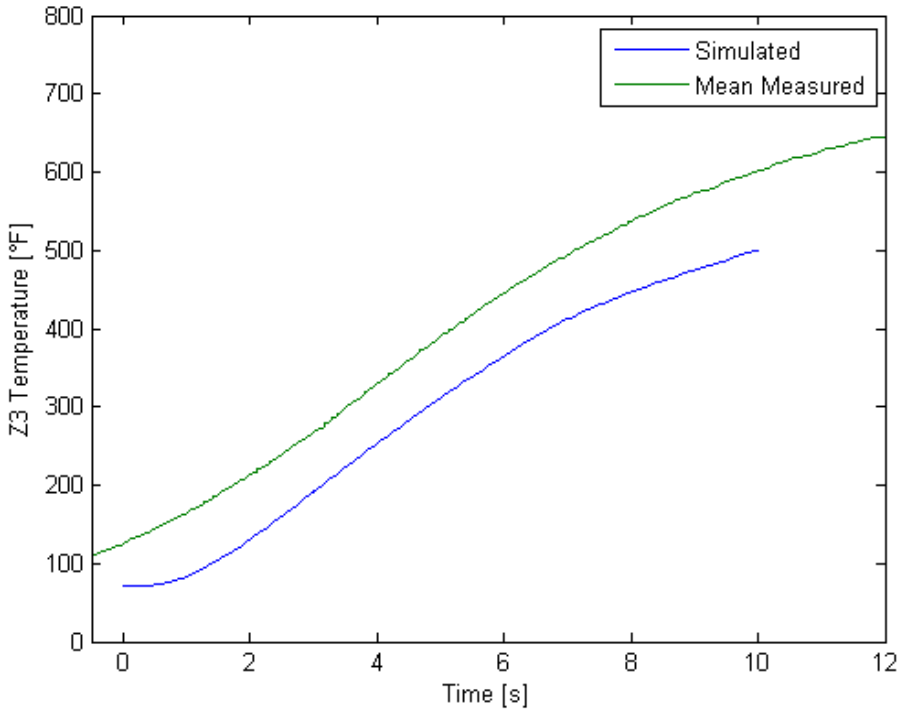

Figure 75: Run 103 Temperature at Axial Station 3

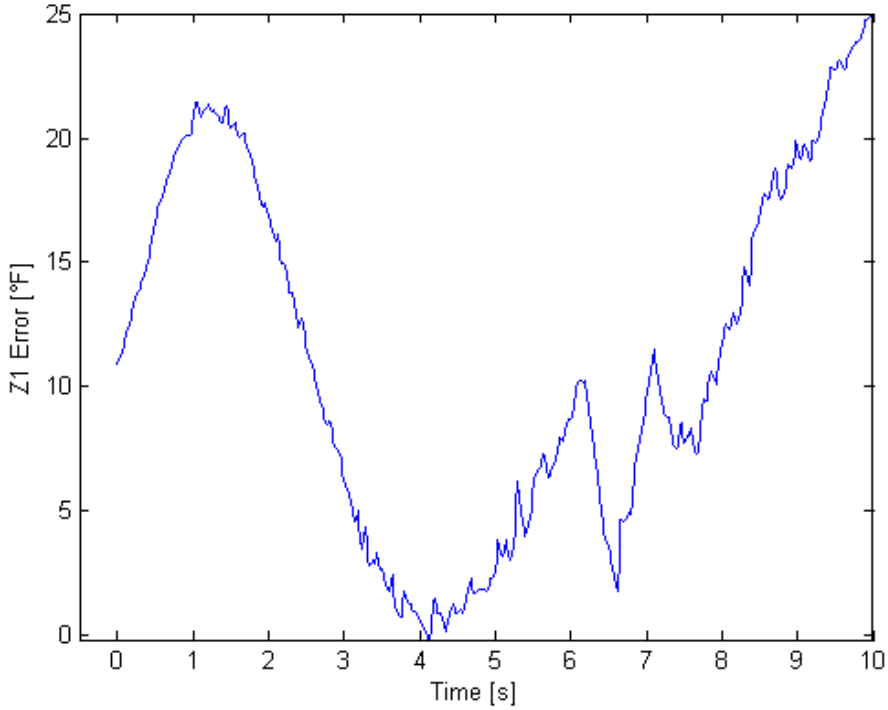

Figure 76: Run 103 Error, Measured Values Minus Simulated Values, Axial Station 1

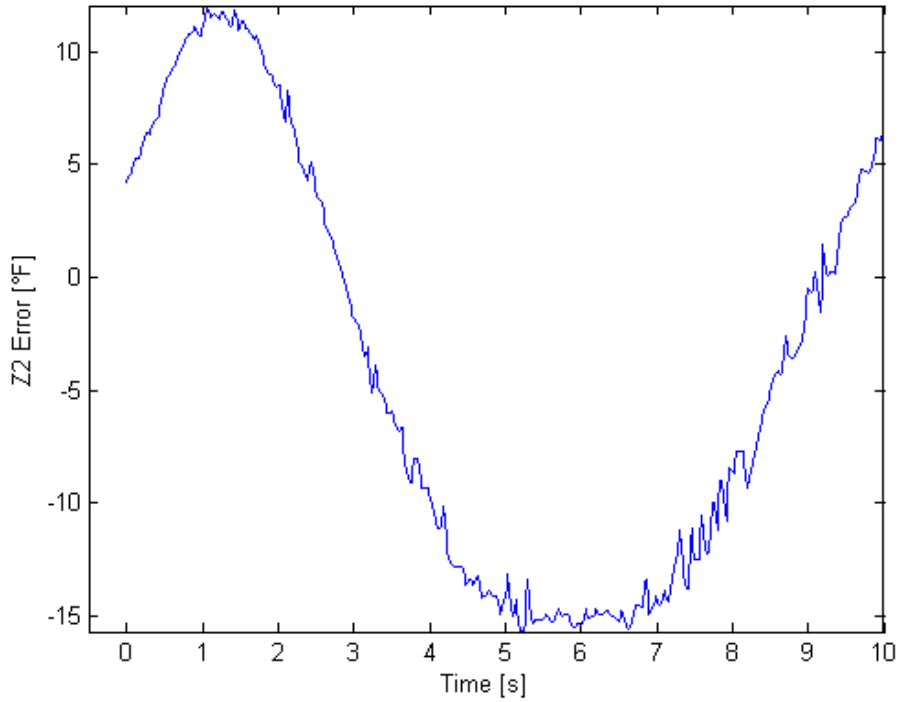

Figure 77: Run 103 Error, Measured Values Minus Simulated Values, Axial Station 2

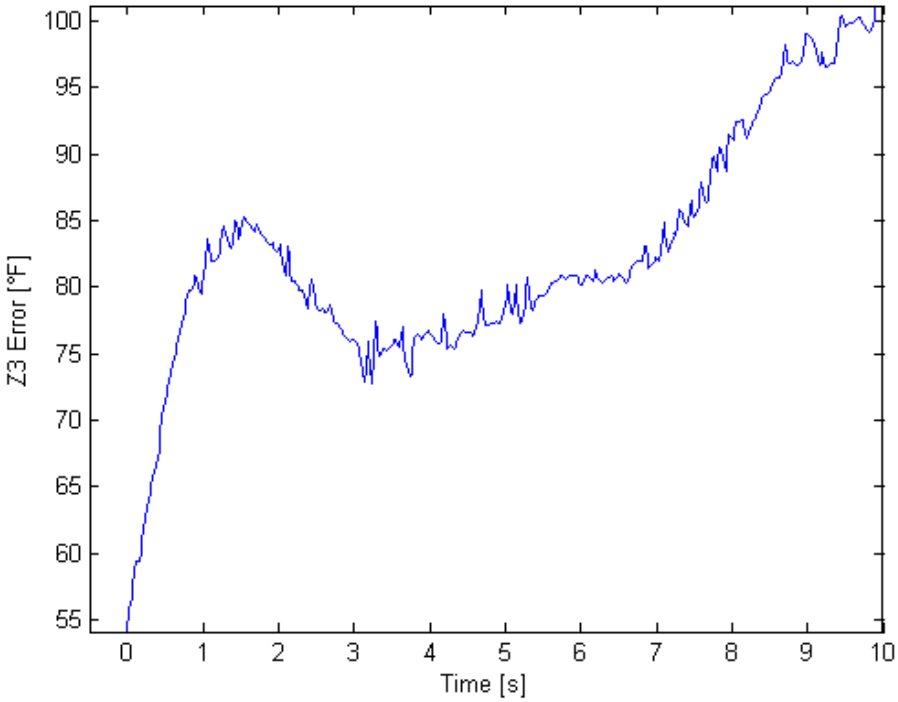

Figure 78: Run 103 Error, Measured Values Minus Simulated Values, Axial Station 3

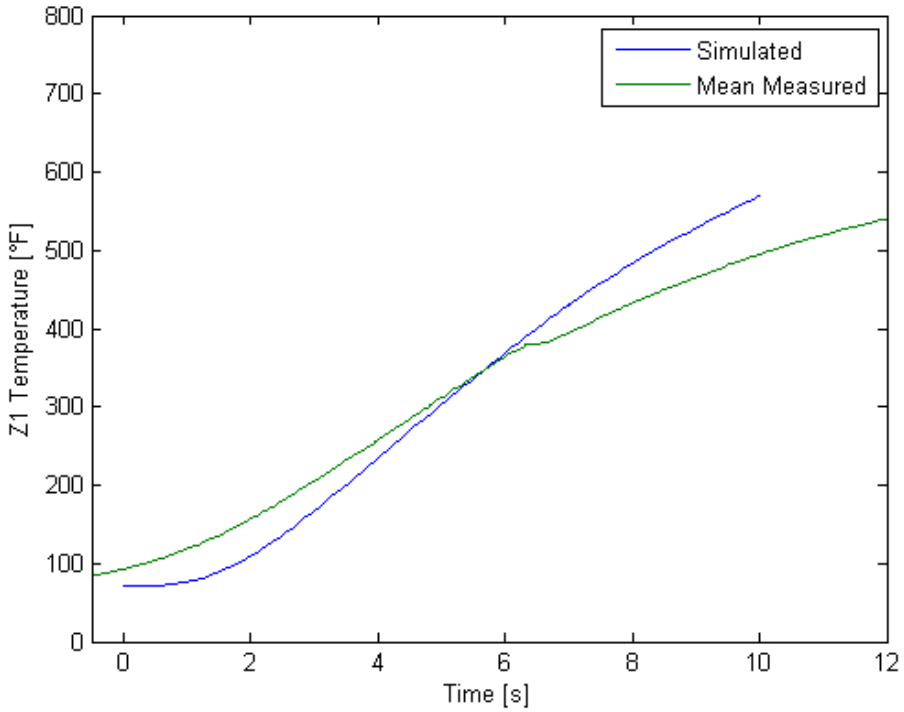

Figure 79: Run 105 Temperature at Axial Station 1

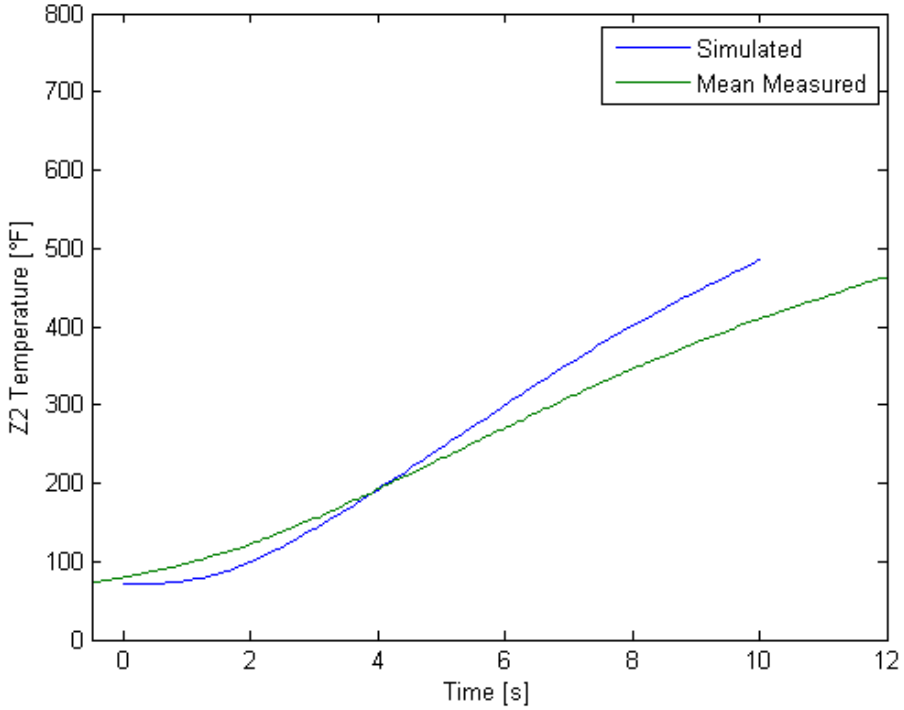

Figure 80: Run 105 Temperature at Axial Station 2

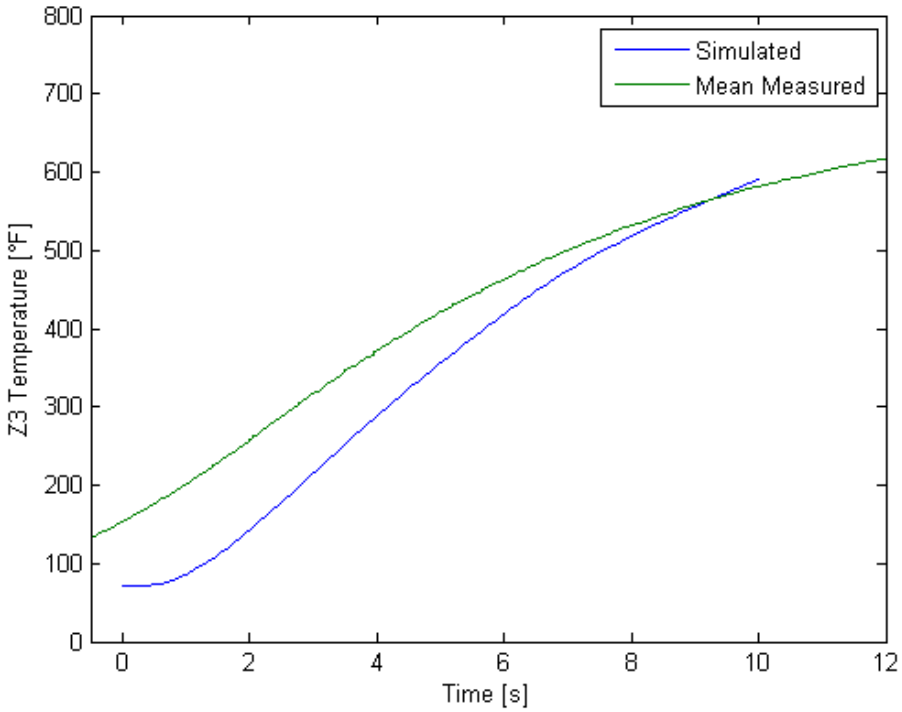

Figure 81: Run 105 Temperature at Axial Station 3

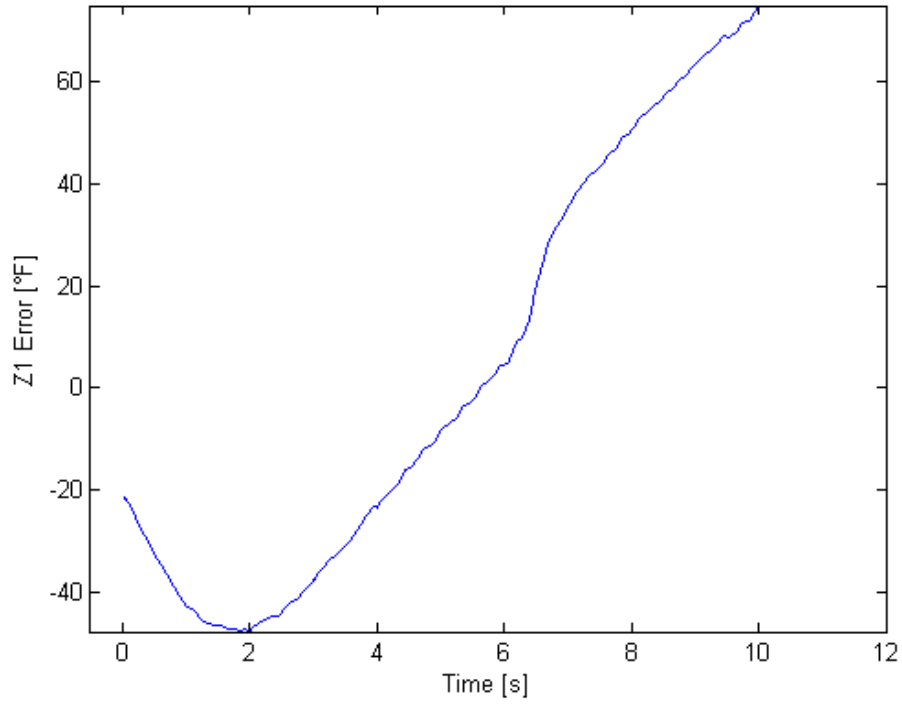

Figure 82: Run 105 Error, Measured Values Minus Simulated Values, Axial Station 1

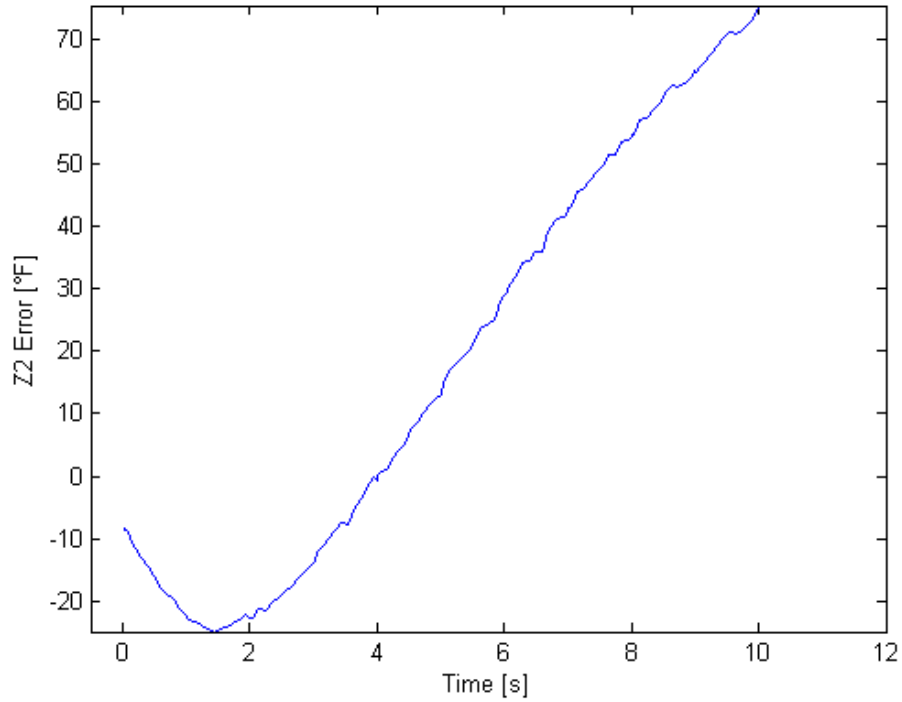

Figure 83: Run 105 Error, Measured Values Minus Simulated Values, Axial Station 2

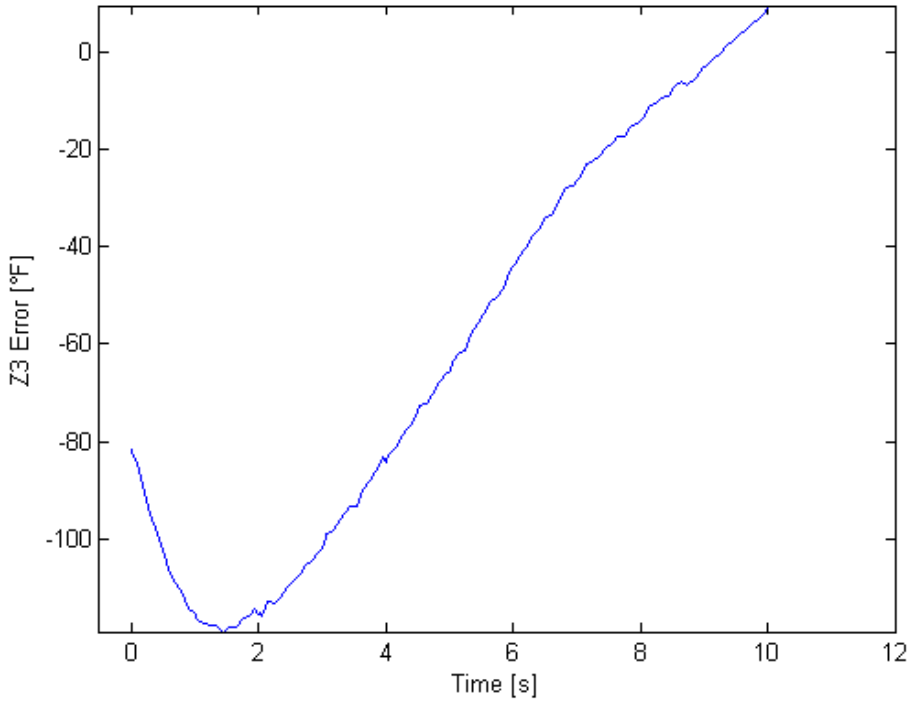

Figure 84: Run 105 Error, Measured Values Minus Simulated Values, Axial Station 3

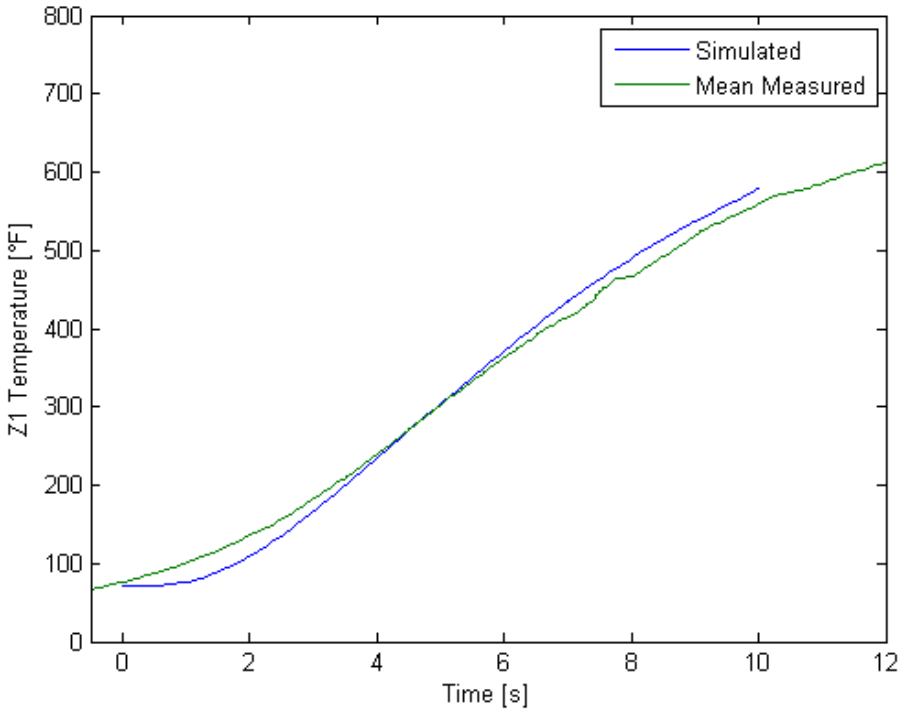

Figure 85: Run 106 Temperature at Axial Station 1

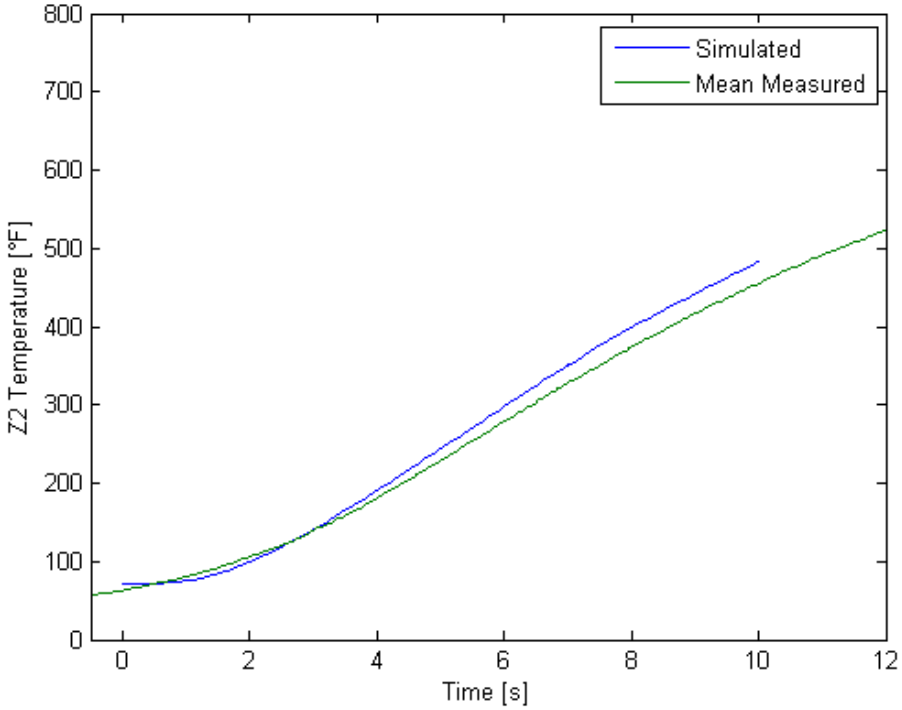

Figure 86: Run 106 Temperature at Axial Station 2

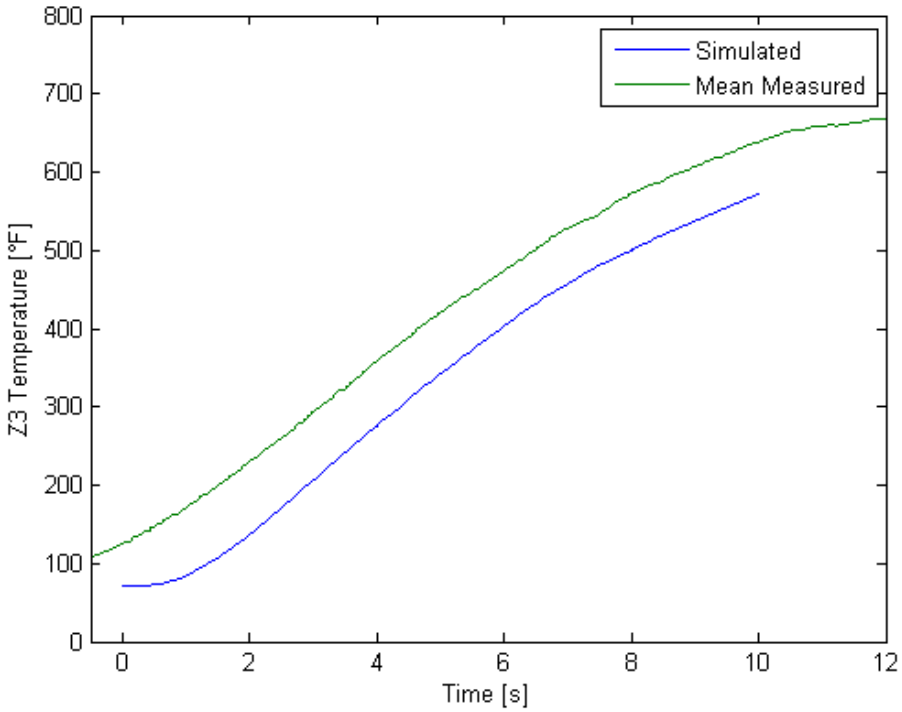

Figure 87: Run 106 Temperature at Axial Station 3

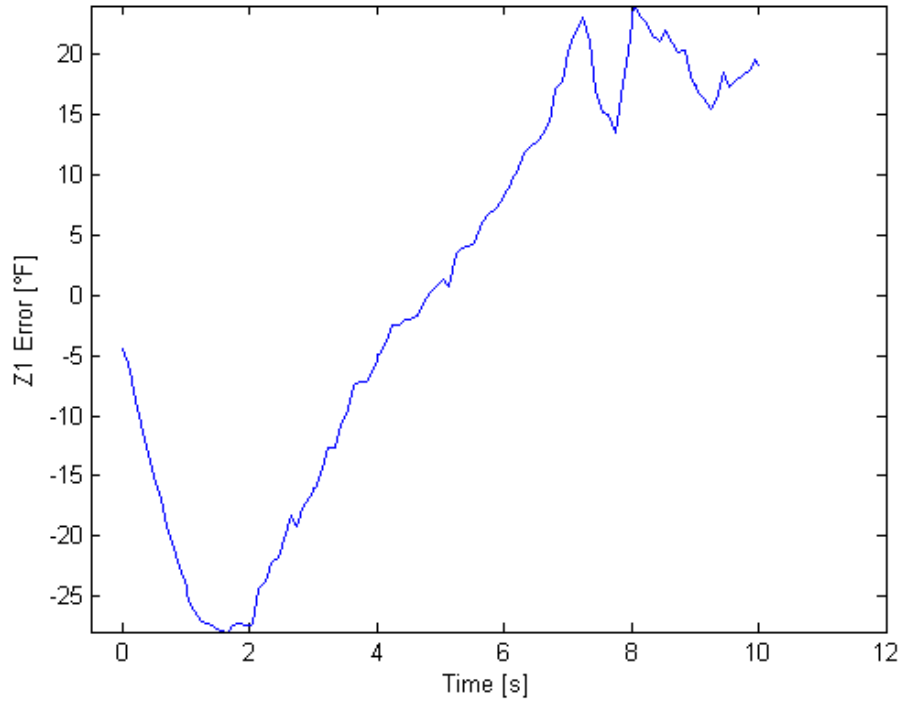

Figure 88: Run 106 Error, Measured Values Minus Simulated Values, Axial Station 1

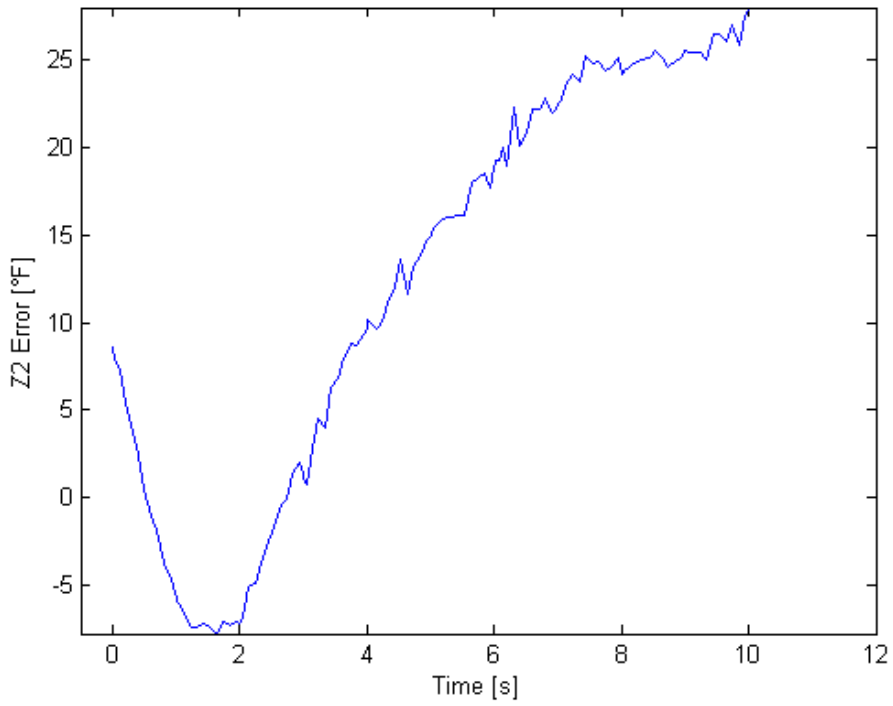

Figure 89: Run 106 Error, Measured Values Minus Simulated Values, Axial Station 2

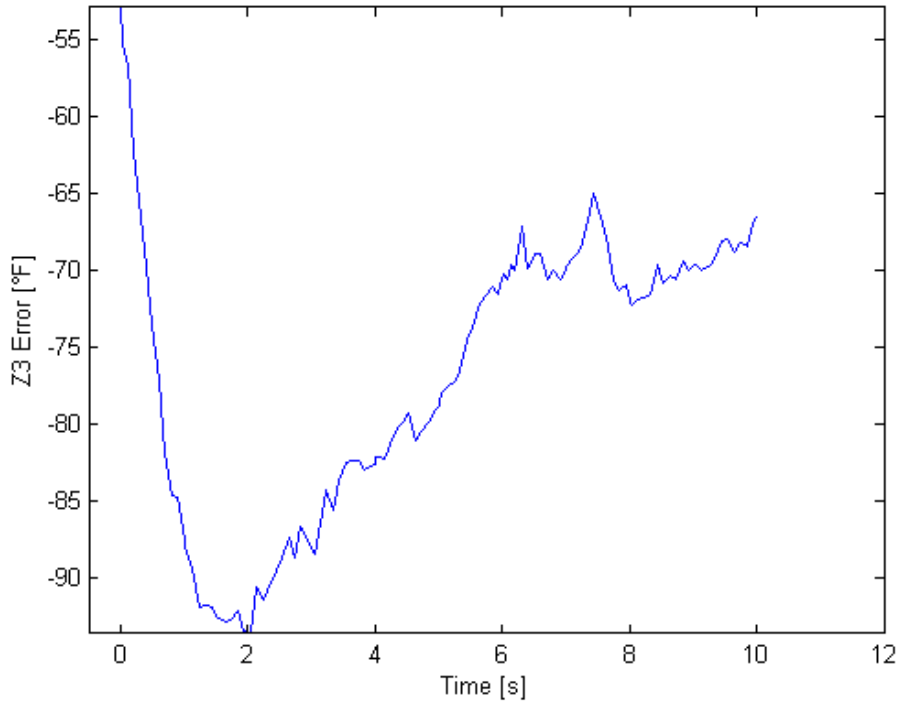

Figure 90: Run 106 Error, Measured Values Minus Simulated Values, Axial Station 3

Table 12: Run 103 Errors

Run 103 Station	Mean Error [°F]	Maximum Error [°F]	Mean Abs Error [°F]
Z1	11.159	25.024	11.160
Z2	-4.075	-15.693	9.157
Z3	82.567	101.158	82.567

Table 13: Run 105 Errors

Run 105 Station	Mean Error [°F]	Maximum Error [°F]	Mean Abs Error [°F]
Z1	0.283	75.027	33.464
Z2	16.359	75.554	28.957
Z3	-61.67	-119.188	62.254

Table 14: Run 106 Errors

Run 106 Station	Mean Error [°F]	Maximum Error [°F]	Mean Abs Error [°F]
Z1	0.209	-27.929	14.141
Z2	12.382	28.027	14.408
Z3	-75.366	-93.65	75.366

Table 15: Run 103 Slopes

Run 103 Station	Mean Simulated Slope [°F/s]	Mean Measured Slope [°F/s]	Error [°F/s]
Z1	35.700	35.330	-0.370
Z2	29.125	25.857	-3.268
Z3	48.883	53.238	4.355

Table 16: Run 105 Slopes

Run 105 Station	Mean Simulated Slope [°F/s]	Mean Measured Slope [°F/s]	Error [°F/s]
Z1	49.498	45.178	-4.320
Z2	37.975	31.828	-6.147
Z3	57.832	51.584	-6.248

Table 17: Run 106 Slopes

Run 106 Station	Mean Simulated Slope [°F/s]	Mean Measured Slope [°F/s]	Error [°F/s]
Z1	49.817	47.798	-2.019
Z2	37.617	35.960	-1.657
Z3	55.250	57.680	2.430

For all three runs, each axial station showed good agreement between simulation and experiment both in terms of profile shape and magnitude. The time rate of temperature change at a particular spatial location is related to the convective heat flux through the heat equation:

$$\frac{dT}{dt} = \frac{\nabla \cdot (\mathrm{k}\nabla T)}{\rho c_p}$$

where k is thermal conductivity, ρ is mass density, and c_p is the specific heat at constant pressure. As the time derivative of the temperature is proportional to the convective heat flux, it is logical to compare the simulated and measured temperature slopes rather than the exact temperatures. Were the temperature distribution within the Spider at the beginning of the burn known with great accuracy, it would likely be possible to match the simulated and experimental temperatures more closely. Due to heat transfer during the pre-ignition phase, the Spider is not at a uniform ambient temperature when the primary burn starts. Rather than attempt to simulate the pre-ignition phase to account for "pre-heating," the time rate of change of the temperatures is examined instead.

Though the simulated temperature profile at the third station matches the shape and slope of the experimental profile, the third station suffers from significantly more error that may be due to a number of different sources. First, the distribution of the soot on the spider surface is assumed to be of uniform, homogenous thickness. In reality, the soot is likely to be thicker on the bottom of the spider (closer to the first axial station) where the flame impinges the device. Literature[35] suggests that the soot is packed more densely closer to the surface, such that an increase in the total thickness of a soot layer means significantly more soot, by mass, has been deposited on that portion of the surface.

If the soot is less thick on top of the spider, nearest the third axial station, then the heat transfer in that region will be lower in magnitude than that predicted for a constant thickness, presumably resulting in an increase in the computed temperature that would reduce the error. Measuring the

soot layers using typical tools, such as calipers, is inaccurate; calipers tend to compact the soot layer and must be perfectly clamped onto the dimension of interest without any movement thereafter, lest the soot be displaced and the measurement lost completely. The dearth of information on the ash distribution makes accurate modeling difficult. Rather than make a change to the model not supported by observation or validated analysis, this error is deemed acceptable.

Another possible source of error is the precision of the probe locations. If the actual location of the thermocouple junction varies then it will introduce a discrepancy between the modeled and measured results that will produce an observable error. An example that makes use of this effect conversely involves comparing the measured results for the third axial station to the temperatures simulated at a location 0.0625" higher. By moving the location of the simulated temperature, much greater agreement can be found between the simulated and measured temperatures. This may suggest that the probe junctions at the axial stations are actually higher than was thought, but this cannot be confirmed without destroying the experimental prototype. Even with a destructive test, it is doubtful whether the exact locations of the junctions could be ascertained post-destruction.

It may be considered desirable to compare experimental results to earlier model phases in an attempt to achieve the most accuracy with the least model complexity in order to facilitate parametric studies or rapid design iterations. Future work on this particular project, however, is likely to be focused on developing an active cooling methodology. In order to accurately predict the temperature distribution in the device and ensure robust performance while guarding against thermal failure, the three-dimensional fluid and conductive phenomena cannot be ignored. The probability that the cooling passageways are not likely to be easily simplified into a lower-dimensional model further enforces this sentiment. Such an analysis is not within the scope of this project.

VIII. CONCEPT DESIGN: ACTIVELY COOLED STRUCTURAL WEBBING

Without an active cooling strategy, it is unlikely that the structural webbing will survive for an extended period of time, given that the ambient flow temperature is significantly hotter than the melting point of most metals. Though some refractory metals have sufficiently high melting temperatures to survive, they are restrictively expensive to acquire and form. The need for a low-cost design capable of being manufactured using the resources existing at Cal Poly and consistent with the direction of the Hybrid Rocket group's research motivates the following concept designs. Detail design of the actively cooled spider will require further characterization of the two-phase coolant flow, and is therefore not yet feasible.

Design Version 1

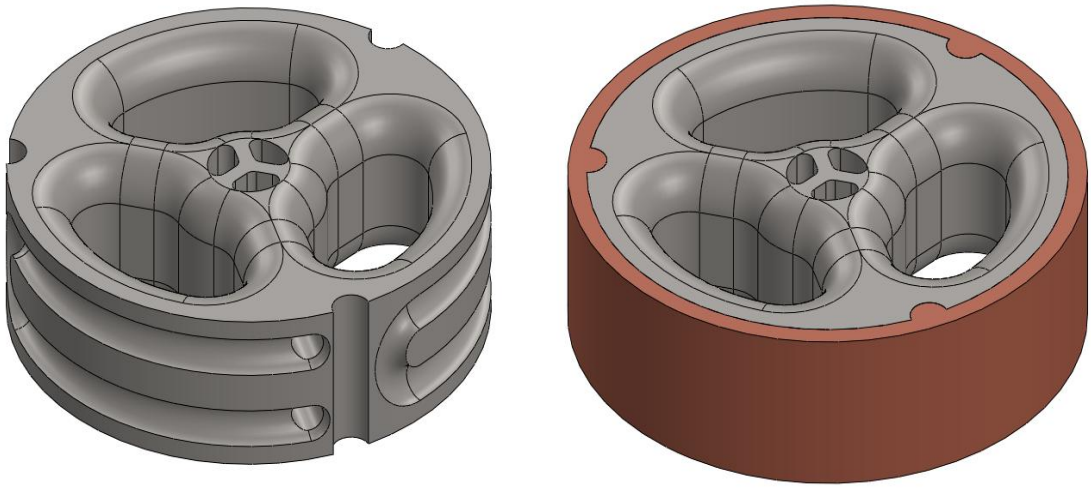

Figure 91: Cooled Spider Concept 1

As shown in Figure 91, the actively cooled structural webbing concept design resembles the prototype used for empirical validation. This concept version relies on an indirect cooling method, keeping the center of the spokes and the outer edges cooled. This strategy assumes that heat will be conducted away from the leading edge quickly enough that the device can survive indefinitely. Detail design will require an in-depth consideration of this conduction to ensure the feasibility of the suggested strategy.

The envisioned manufacturing process begins when the raw material is faced and turned on a lathe to the designed dimensions and surface finish. Next, the three axial pockets are cut while the part is clamped in a soft jaw vise. The cross sections are rounded to maximize available thermal capacitance at the forward stagnation point, and to enable easy manufacture with corner-rounding end mills. Producing the upstream and downstream fillets requires two setups, as was the case for the instrumented iteration.

The most notable features are the two passages drilled into each spoke and the coolant channel on the external radius. These features would be produced using a fourth-fifth axis rotary table add-on to a CNC mill, several of which are currently in use at the Cal Poly facilities. The passages that run through the spokes are located using the fifth-axis, then drilled and reamed to size. The coolant channel on the outer annulus is milled with a ball end mill, using the rotary action of the fifth-axis to smoothly maintain accurate depth of cut.

In place of a central through-hole, two sets of three pockets are milled from either end, leaving some material at the mid-plane. The material left at the mid-plane serves to separate the upstream and downstream ports to prevent unnecessary coolant backflow. Addition of the mid-plane material is also advantageous from a manufacturing standpoint, as it reduces the depth of cut from what was needed to produce the through-hole in the instrumented prototype, without requiring any additional setups. A smaller through-hole might be put in this feature to enable recirculation, though recirculation designs would require redesign of the existing center channel and cooled aerospike.

To seal the outer annulus, an OFHC copper ring is brazed to the stainless steel webbing, using the brazing techniques developed for the cooled aerospike. The copper ring enables coolant flow along the outer edge and interfaces the insulating chamber liner.

Design Version 2

Figure 92: Cooled Spider Concept 2

The second concept design for the actively cooled spider, shown in Figure 92, seeks to directly cool the leading and trailing edges where the heat transfer is greatest, in contrast to the indirect cooling used for the first design. The cooling passages are milled along the pocket edges on both the top and underside of the device. These passages are connected by through holes drilled at the termination of the underside channels to allow axial coolant flow. The OFHC copper shells, shown in Figure 93, are brazed to each side of the stainless portion of the device to form a clamshell. As with the first design, a redesign of the existing cooled aerospike and surrounding infrastructure would be required to make use of a regenerative cooling technique.

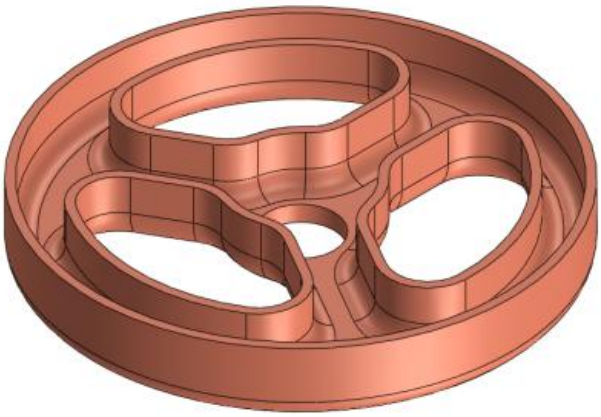

Figure 93: Cooled Spider Design 2, Copper Shell

IX. CONCLUSION

A model for simulating the convective heat transfer to a webbed structure designed to prevent deflection of annular aerospikes was developed in three phases. At each model phase, complexity was progressively increased until a fully-featured three-dimensional model was produced. Flow within the hybrid rocket motor was simulated in ANSYS FLUENT using flow parameters calculated by NASA-CEA, and conduction within the device was simulated using the ANSYS Transient Thermal module.

An experimental prototype of the structural webbing with embedded thermocouple probes was designed, built, and subjected to a series of hotfire tests. The transient temperature data gathered from these tests was compared to the simulated temperature profiles and used to validate the model. Though there was a notable discrepancy between the simulated and experimental temperatures at one measurement station, the simulated rate of temperature change was shown to agree with the experimental rate of temperature change for all stations. The agreement in the rate of temperature change indicated that the convective heat load was accurately modeled.

Future Work

Should the accuracy of the model presented herein be deemed insufficient, there are several phenomena which might be investigated to improve model fidelity. First, the composition, distribution, and thermophysical properties of the soot layer that forms on the surface of the Spider could be determined experimentally. A more accurate sooting model would be a good first step towards pinpointing the source of any model discrepancies.

Investigating the effects of incomplete combustion on the thermophysical properties of the exhaust flow might also improve model fidelity. A semi-empirical correlation for combining

knowledge of combustion efficiency with the outputs of NASA-CEA would allow designers to more accurately quantify the gas properties for a range of different reactants.

Several proposed improvements to the Cal Poly Hybrid Rocket Test Stand would facilitate future project efforts and add to the accuracy of the existing models. Acquiring a mass flux measurement device such as a Coriolis flow meter would provide a method for acquiring accurate real time oxidizer mass flow data with high resolution. Presently, oxidizer mass flow rates are determined by examining the change in weight of the oxidizer supply bottles through a scale with 0.5lb resolution and a low signal-to-noise ratio. Developing a method for determining the regression rate of the solid fuel in real time would further improve fidelity and synergize well with the oxidizer mass flow rate measurements. Presently, solid fuel mass flow rates are estimated by measuring the change in weight of the solid fuel grains and assuming a constant rate of pyrolysis during the burn. Automating the ignition sequence, which is presently performed manually, would improve test repeatability by removing a source of human error. To automate the ignition, a set of criteria for measuring when the fuel grain is fully lit and ready for the main oxidizer to be flowed must be developed, and a set of electronically controlled valves must be integrated into the existing hardware.

Though the uncooled structural webbing was shown to survive multiple hotfire tests without observable damage, the extreme temperature of the exhaust gases would eventually cause the device to overheat and fail due to thermal effects during an extended duration burn. In order to produce a device that can survive in steady state, an active cooling strategy must be implemented.

Two concept designs for an actively cooled iteration of the structural webbing were presented in this report. The concept designs suggested methods for manufacturing enclosed cooling passages on a modified version of the experimental prototype. To complete the detail design of the cooled

Spider, a complete thermal analysis of both the external convective heat load and the internal cooling heat transfer must be conducted. The primary goal of such a design would be to ensure that the cooling heat transfer from the device is greater than or equivalent to the convective heat transfer to the device, guaranteeing that the device will not fail due to overheating. The models developed in this project may be used to predict the convective heat transfer from the exhaust flow. More analysis and modeling work remains to determine the necessary cooling heat flux, the coolant delivery strategy, and the coolant flow rate for a given strategy.

Nitrous oxide has previously been used as a coolant in an actively cooled rocket nozzle and aeropsike, though a validated model of the two-phase flow has not yet been produced. Development and validation of a model for two-phase flow of nitrous oxide is currently the subject of a series of Cal Poly projects. Once achieved, a validated two-phase nitrous oxide model may be used in the design of the actively cooled structural webbing.

The cooled aerospike and rocket nozzle were designed to eject the nitrous oxide as base bleed after using it as a coolant. A likely improvement in cooling strategy would be to regeneratively flow the nitrous oxide back into the combustion chamber for use as the primary oxidizer. A regenerative cooling technique would be especially advantageous if multiple cooled parts were present, as the coolant flow to each part could come from a single source. Furthermore, using the coolant as oxidizer would remove the need for individual reservoirs, resulting in a weight reduction that would be desirable for any rocket designed for flight. Developing a regenerative cooling strategy would require detail design of the coolant delivery system, as well as a complete analysis of the convective heat load to each subsystem and the cooling heat transfer throughout the system. The methods presented in this paper could be extended to quantify the external heat load on each part.

REFERENCES

[1] Chiaverini, Martin J., George C. Harting, Kenneth K. Kuo, and Arie Peretz. "Regression-Rate and Heat-Transfer Correlations for Hybrid Rocket Combustion." *Journal of Propulsion and Power* 17.1 (2001): 99-110. Web.

[2] Muzzy, R. J. and Wooldridge, C. E. "Internal ballistic considerations in hybrid rocket design." *Journal of Spacecraft and Rockets*, Vol. 4, No. 2 (1967), pp. 255-262. doi: 10.2514/3.28844

[3] Sutton, George Paul. *Rocket Propulsion Elements: An Introduction to the Engineering of Rockets*. New York: Wiley, 1986.

[4] Nelson, Lauren M., "Rayleigh Flow of Two-Phase Nitrous Oxide as a Hybrid Rocket Nozzle Coolant," Master's Thesis, California Polytechnic State University, Sept. 2009.

[5] Brennen, Peter. **"**Simulation of an Oxidizer-Cooled Hybrid Rocket Throat: Methodology Validation for Design of a Cooled Aerospike Nozzle." Master's Thesis, California Polytechnic State University, 2009.

[6] Grieb, Daniel, "Design and Analysis of a Reusable N_2O-cooled Aerospike Nozzle for Labscale Hybrid Rocket Motor Testing." Master's Thesis, California Polytechnic State University, 2011.

[7] Browning, William R. "Preliminary Design Study of an Un-cooled Annular Aerospike Nozzle". Master's Thesis, California Polytechnic State University, 2007.

[8] Imbaratto, David, "The Interaction between Throttling and Thrust Vectoring of an Annular Aerospike Nozzle," Master's Thesis, California Polytechnic State University, Sept. 2009.

[9] Beebe, Stanley Ikuo. "Hole-type Aerospike Compound Nozzle Thrust Vectoring". Master's Thesis, California Polytechnic State University, 2009.

[10] Marxman, G. and Gilbert, M., "Turbulent Boundary Layer Combustion in the Hybrid Rocket," *Ninth* Symposium (International) on Combustion, Academic Press, 1963, pp 371-372.

[11] Zilliac, Greg, and M. Arif Karabeyoglu. "Hybrid Rocket Fuel Regression Rate Data and Modeling." *Proceedings of the 42nd AIAA/ASME/SAE/ASEE Joint Propulsion Conference & Exhibit*, pp 4504-4513, July 2006, AIAA Paper 2006-4504.

[12] Lee, Changjin. "Internal Flow Dynamics and Regression Rate in Hybrid Rocket Combustion." *International Journal of Aeronautical and Space Sciences* 13.4 (2012): 507-14. Web.

[13] Chiaverini, M. J., Serin, N., Johnson, D., Lu, Y. C., Kuo, K. K., and Risha, G. A., "Regression Rate Behavior of Hybrid Rocket Solid Fuels ," *Journal of Propulsion and Power*, Vol. 16, No. 1, January-February 2000, pp. 125-132.

[14] Doran, E., Dyer, J., Lohner, K., Dunn, Z., Cantwell, B., and Zilliac, G. "Nitrous oxide hybrid rocket motor fuel regression rate characterization." *Proceedings of the 43rd*

AIAA/ASME/SAE/ASEE Joint Propulsion Conference, pp. 3485–3496, July 2007, AIAA Paper 2007-5352.

[15] Greiner, B., and Federick, R, "Results of Labscale Hybrid Rocket Motor Investigation," *AIAA/ASME/SAE/ASEE 28th Joint Propulsion Conference & Exhibit*, Nashville, TN, AIAA, Paper 92-3301,1992.

[16] "CEARUN." NASA, Web. <http://www.grc.nasa.gov/WWW/CEAWeb/ceaHome.htm>

[17] Bejan, Adrian, and Kraus, Allan D. *Heat Transfer Handbook*. New York: J. Wiley, 2003. Print.

[18] Kays, W. M. *Convective Heat and Mass Transfer*. New York: McGraw-Hill, 1966. Print.

[19] Pefley, R. K. Convection Heat Transfer Coefficients in De Laval Nozzles, Technical Report No. HS-3. 1951. Print.

[20] V.K. Sin and T.Y. Tong, "Stagnation-Point Pressure Distribution and Wall Shear Stress: Numerical Simulation and Similarity Solution", Proceedings of the World Congress on Engineering 2009 (WCE2009) - The International conference of Mechanical Engineering, July 1-3, 2009, Imperial College London, London, UK, pp. 1673-1678, ISBN 978-988-18210-1-0

[21] Bartz, D. R. "An Approximate Solution of Compressible Turbulent Boundary-Layer Development and Convective Heat Transfer in Convergent-Divergent Nozzles." *ASME Transactions*, Vol. 77, No. 8, pp. 1235-1245, November 1955.

[22] "ANSYS CFX-Solver Modeling Guide." <http://www.mecheng.osu.edu/documentation/Fluent14.5/ 145/cfx_mod.pdf>

[23] Bartz, Donald R. "A Simple Equation for Rapid Estimation of Rocket Nozzle Convective Heat Transfer Coefficients," *Jet Propulsion*, Vol. 27, p. 49, January, 1957.

[24] "Optimal Thrust Vectoring for an Annular Aerospike Nozzle," NASA STTR Phase II Grant, Contract NND06AB82C, 06/06 – 06/08. Principal Investigator: T.W. Carpenter, co-Investigators: W.R. Murray.

[25] "A Reusable, Oxidizer-Cooled, Hybrid Aerospike Rocket Motor for Flight Test," NASA STTR Phase I Grant, Contract NNX08CD33P, 01/08 - 01/09. Principal Investigator: W.R. Murray, co-Investigators: T.W. Carpenter, J.D. Mello, P. Lemieux, and M. Kerho.

[26] "A Reusable, Oxidizer-Cooled, Hybrid Aerospike Rocket Motor for Flight Test," NASA STTR Phase II Grant, Contract NNX10RA29C, 10/23/09 – 04/22/11. Principal Investigator: W.R. Murray, co-Investigators: J.D. Mello, P. Lemieux, and M. Kerho.

[27] White, Frank M. *Viscous Fluid Flow*. New York: McGraw-Hill, 1974. Print.

[28] Elliot, David G., Bartz, Donald R., and Silver, Sidney. "Calculation of Turbulent Boundary-Layer Growth and Heat Transfer in Axisymmetric Nozzles." *Technical Report No. 32-387*, Jet Propulsion Laboratory, Pasadena, February 15, 1963.

[29] Simulia Inc. ABAQUS CAE & Analysis User's Manual, Theory Manual. Simulia Inc., 2007.

[30] Young, Warren C., *Roark's Formulas for Stress and Strain*. New York, NY: McGraw-Hill, 1989.

[31] "Partial Differential Equation Toolbox." Mathworks, 1 Aug. 1995. Web. 19 May 2014.

[32] Welsh, W. E. Jr., and A. B. Witte, "A Comparison of Analytical and Experimental Local Heat Fluxes in Liquid-Propellant Rocket Thrust Chambers," Technical Report No. 32-43, Jet Propulsion Laboratory, Pasadena, February 1, 1961.

[33] Smithells, Colin J., and Eric A. Brandes. *Metals Reference Book*. London: Butterworths, 1976. Print.

[34] Graves, R. S., T. G. Kollie, D. L. Mcelroy, and K. E. Gilchrist. "The Thermal Conductivity of AISI 304L Stainless Steel." *International Journal of Thermophysics* 12.2 (1991): 409-15. Web.

[35] Preciado, Ignacio. *Study of Soot Deposition in Flames and Its Effect on Heat Transfer to Metal Surfaces*. Dissertation, Department of Chemical Engineering, University of Utah, 2009. Print.

[36] Madhusudana, C.V. *Thermal Contact Conductance.* New York: Springer, 1996.

[37] McGee, G. R., Schankula, M. H., and Yovanovich, M. M., 1985, "Thermal Resistance of Cylinder-Flat Contacts: Theoretical Analysis and Experimental Verification of a Line-Contact Model," *Nuclear Engineering Design,* 86, pp. 369–381

[38] Zanstra, P. E. "Welding Uniform Sized Thermocouple Junctions from Thin Wires." *Journal of Physics E: Scientific Instruments* 9.7 (1976): 526-28. Web.

Appendix A: Derivation of Bartz Modification

Appendix B: Matlab Code

i. Bartz Solver

ii. BartzStartz

iii. BartzMesher

iv. Walzing

v. Structural Webbing Heat Transfer Load Estimator

vi. CEASE

vii. FLUENT2ABAQUS

viii. F3DI

ix. Hotfire Data Processor

x. Parametric Study

xi. Thermal Contact Conductance Worksheet

Appendix C: Experimental Apparatus Drawings

APPENDIX A: DERIVATION OF BARTZ MODIFICATION

In order to apply the solution methodology proposed by Bartz[23], the integral equations of interest must be modified. The original equations assume an axisymmetric geometry, which is typically valid for a nozzle contour. This analysis extends the original results to the general geometry case. Beginning with Bartz's equation D19, the momentum balance is

$$\frac{d}{dx}\left(\dot{M}_r + 2\pi r\rho U^2\theta\right) = -2\pi r(\delta'_r - \delta^*)\frac{dp}{dx} \tag{D19}$$

where the 2πr terms represent the local cross-sectional area, assuming a circular geometry, and the $\frac{d}{dx}$ terms are presented for an axial-wise integral. The 2πr terms are replaced with a generic local cross-sectional area term, A_s, and the axial derivatives are replaced with a surfacewise derivative, $\frac{d}{ds}$. Equation D19 now becomes

$$\frac{d}{ds}\left(\dot{M}_r + A_s\rho U^2\theta\right) = -A_s(\delta'_r - \delta^*)\frac{dp}{ds} \tag{D19M}$$

where the M indicates the modified form of Equation D19 given by Bartz. Now, following Bartz's method with this substitution, the equations become

$$\frac{d}{ds}\dot{M}_r = -A_s(\tau_w + \delta'_r\frac{dp}{ds}) \tag{D20M}$$

$$\frac{d}{ds}(A_s\rho U^2\theta) = A_s(\tau_w - \rho U\delta^*\frac{dU}{ds}) \tag{D21M}$$

Differentiating D21< by parts and introducing $C_f = \frac{2\tau_w}{\rho U^2}$, the skin-friction coefficient yields

$$\frac{d\theta}{ds} = \frac{C_f}{2} - \theta[\frac{1+\frac{\delta^*}{\theta}}{U}\frac{dU}{ds} + \frac{1}{\rho U}\frac{d(\rho U)}{ds} + \frac{1}{A_s}\frac{dA_s}{ds}] \tag{D22M}$$

Writing expressions for density and velocity as a function of the Mach number gives

$$\frac{1}{U}\frac{dU}{ds} = \frac{1}{M(1+\frac{\gamma-1}{2}M^2)}\frac{dM}{ds} \tag{D23M}$$

$$\frac{1}{\rho U}\frac{d(\rho U)}{ds} = \frac{1-M^2}{M(1+\frac{\gamma-1}{2}M^2)}\frac{dM}{ds} \tag{D24M}$$

Substituting D23M and D24M into D22M and transforming the independent variable to z yields

$$\frac{d\theta}{dz} = \frac{C_f}{2}\frac{ds}{dz} - \theta\left[\frac{2-M^2+\frac{\delta^*}{\theta}}{M\left(1+\frac{\gamma-1}{2}M^2\right)}\frac{dM}{dz} + \frac{1}{A_s}\frac{dA_s}{dz}\right] \quad \text{(D25M)}$$

Now, moving to the energy equation, which is

$$\frac{d}{ds}\left(\dot{H}_r + A_s\rho U c_p(T_0 - T_w)\varphi\right) = 0 \quad \text{(D26M)}$$

$$\frac{d}{ds}\dot{H}_r = -A_s q_s \quad \text{(D27M)}$$

Next, D27M is subtracted from D26M to yield

$$\frac{d}{ds}\left(A_s\rho U c_p(T_0 - T_w)\varphi\right) = A_s q_s \quad \text{(D28M)}$$

Differentiating D28M by parts yields

$$\frac{d\varphi}{ds} = \frac{1}{A_s\rho U c_p(T_0 - T_w)}\left[A_s q_s - \varphi\frac{dA_s}{ds}\rho U c_p(T_0 - T_w) + \frac{d\rho U c_p}{ds}\left((T_0 - T_w)A_s\right)\right] \quad \text{(D29M)}$$

Recalling the Stanton Number, $C_h = \frac{q_s}{\rho U c_p(T_{aw} - T_w)}$, substituting the Mach number relations, and transforming the independent variable to z yields

$$\frac{d\varphi}{dz} = C_h\left(\frac{T_{aw} - T_w}{T_0 - T_w}\right)\frac{ds}{dz} - \varphi\left[\frac{1-M^2}{M\left(1+\frac{\gamma-1}{2}M^2\right)}\frac{dM}{dz} + \frac{1}{A_s}\frac{dA_s}{dz} - \frac{1}{(T_0 - T_w)}\frac{dT_s}{dz}\right] \quad \text{(D30M)}$$

The remaining equations of the integral solver do not make use of the axisymmetric geometry assumption and are therefore unchanged.

APPENDIX B: MATLAB CODE

Bartz Integral Equation solver, Version 3.0

This function is called by ODE45 and used to solve the integral equations describing the development of the momentum and energy boundary layers as given by Bartz in JPL Technical Report No 32-387. The equations have been slightly modified to solve for the boundary layers that develop over the structural webbing, and the resulting distribution of film coefficients may be used tosolve thermomechanical FEA problems. This version of the file works with the BartzGeometry function to solve for the film coefficient distribution over the spider.

Contents

- Bartz Zeta Case I Solver, Zeta >=1, Trapezoidal

Main file

```
function BartzSolver
```

```
clc
clear all
close all
global  dTsdz  To po Ts gamma cp m mu0 Pr n rs
```

Parameters

```
global T1
T1=[2.51 3.10 3.97 4.88 5.73 7.41 8.94 12.75 16.36 23.2 29.6 35.9 41.8 53.6 64.8
    590e-5 524e-5 464e-5 426e-5 398e-5 363e-5 340e-5 308e-5 290e-5 269e-5 255e-5 246e-5 238e-5 227e-
5 219e-5];
% global To po Ts gamma cp m mu0 Pr n rs
To=4500; % °R, stagnation temperature of the freestream
po=300; % psia, stagnation pressure of the freestream
Ts=530; % °R, surface temperature
gamma=1.3; % Dimensionless, stagnation gas specific heat ratio
cp=0.45; % Btu/Lbm*°R, stagnation gas specific heat
m=0.65; % Dimensionless,Temperature dependence of viscosity
rs=0.885;
mu0=1.5764e-6;
dTsdz=0;
Pr=0.60; % Dimensionless, Prandtl number
n=0.1; % Dimensionless, boundary layer interaction exponent
```

Get geometry

```
global zn
r_inner=0.75/2;
r_outer=3.6/2;
dels=0.05;
delz=0.05;
maxz=1;
spokes=3;
g=BartzGeometryv3(r_inner,r_outer,dels,delz,maxz,spokes);
zn=g.z;
Astar=.25*pi*.75^2;
```

Mach number

```
global MM1
delM=0.001;
for i=1:1/delM-5
    MM1(i)=(i+5)*delM;
    AA1(i) = ((1/MM1(i))*(((1+ ((gamma-1)/2)*(MM1(i)^2))/((gamma+1)/2))^((gamma+1)/(2*(gamma-1)))));
end
global Mz dMz

for i=1:length(g.z)
```

```
    Mz(i)=interp1(AA1,MM1,g.A_f(i)/Astar);
end
dMz=ppval(fnder(interp1(zn,Mz,'cubic','pp')),zn);
global MPRO
%  Mpro selects which skin friction coeff relation to use.
MPRO=4;
global options options2
options=optimset('TolX',1e-30);
options2=optimset('TolX',1e-20,'TolFun',1e-20);
options3=odeset('RelTol',1e-9);
zinitial=0.01;
global ge A_s dA_s
A_s=g.A_s;
dA_s=g.dA_s;
```

Solve

```
[zinitial, theta0, phi0, hstart] = BartzStartz;
for j=1:length(fieldnames(g))-5
    ge=g.(sprintf('S%d',j));
    [zz,x] = ode45(@Bartz,[zinitial(end) zn(end)],[theta0 phi0],options3);
    theta=x(:,1);
    phi=x(:,2);
    clear dx hh qw delta triangle delstar Cf Ch zeta
    dx=zeros(length(zz),2);
    for i = 1:length(zz)
        [dx(i,:), hh(i),  qw(i), delta(i), triangle(i), delstar(i), Cf(i), Ch(i),
zeta(i)]=Bartz(zz(i),[x(i,1) x(i,2)]);

    end
    z=[zinitial';zz(2:end)];
    h=[hstart hh(2:end)];
    if j==1
        assignin('base','h',h)
        assignin('base','Ch',Ch)
        assignin('base','cp',cp)
        assignin('base','rhoU',hh./cp./Ch)
        assignin('base','zeta',zeta)
        assignin('base','z',z)
    end
    if j>=28
       assignin('base','h',hh)
        assignin('base','z',z)
    end
        g.(sprintf('h%d',j))=[z h'];
end
global gg
gg=g;
assignin('base','gg',gg)
BartztoAbaqus
```

```
end

function [dx hg qw delta triangle delstar Cf Ch zeta]=Bartz(z,x)
```

ODE45 Function

This function integrates at each surfacewise station. X= [theta phi]

```
global theta phi ge A_s dA_s zn To T Tas Ts dTsdz a b c m mu0 Rtheta
global Rphi cp po n Pr  gamma Mz dMz
```

Provide parameters:

```
theta=x(1);
phi=x(2);
```

A. Interpolation between R, Tw, and M from Input

```
dsdz=interp1(ge(:,3),ge(:,4),z);
```

For testing with Bartz's numbers

```
As=interp1(zn,A_s,z);
dAsdz=interp1(zn,dA_s,z);
```

B. Auxiliary Input Quantities

1. Mach number

```
M=interp1(zn,Mz,z);
dMdz=interp1(zn,dMz,z);
```

2. Temperature Ratios

```
TnotoverT=1+( (gamma-1)/2)*(M^2); % 35
T=To/TnotoverT;
TasoverTo=(1+(0.89*((gamma-1)/2))*(M^2))/(1+(( (gamma-1)/2)*(M^2))); % 18
Tas=TasoverTo*To;
```

3. Constants in Integrals

```
a=Ts/T;
b=-1+To/Ts;
c=( ((gamma-1)/2)*(M^2))*(T/Ts);
```

4. Flow Density

```
rhoU=((32.174/778.2)^(1/2))*gamma*po*M/( sqrt(cp*To*(gamma-1))*( (1+(((gamma-1)/2)*
(M^2)))^((gamma+1)/(2*(gamma-1))) ) );
```

3. Reynolds Numbers

```
Rtheta=(12/32.174)*(rhoU*theta/mu0)*((1+( (gamma-1)/2)*(M^2))^m); % 34 [Check the units]
Rphi=(12/32.174)*(rhoU*phi/mu0)*((1+( (gamma-1)/2)*(M^2))^m); % 45 [Check the units]
```

4. Skin Friction

(a) Adiabatic Skin Friction Coefficient (b) Diabatic Skin Friction Coefficient

```
Cf=C_f(Rtheta,z);
Cfphi=C_f(Rphi,z);
```

5. Stanton Number

```
Ch=( (Cfphi/2)*((phi/theta)^n))/(1-(5*sqrt(Cfphi/2)*(1-Pr+log(6/(5*Pr+1))))); %47
```

6 Ratio of Displacement to Momentum Thickness, Zeta

```
zeta=fzero(@zg1,1.02);
if zeta>=1 % (a)
    delstar=theta*( ((a*zeta^7)/7)-I2(b,c,zeta)-I3(b,c,zeta))/I1(b,c,zeta); % 82
else %(b), zeta<1
    zeta=fzero(@zg1,1);
    delstar=theta*( (a/7)-I6(b,c,zeta)-I7(b,c,zeta))/(I4(b,c,zeta)+I5(b,c,zeta)); % 93
end
```

D. Equations for remaining output quantities

1. Velocity and Temperature Thicknesses

```
if zeta>=1
    thetaoverdelta=(7/a)*I1(b,c,zeta); % 72
else % zeta <1
    thetaoverdelta=(7/a)*(I4(b,c,zeta)+I5(b,c,zeta)); % 85
end
delta=theta/thetaoverdelta;
triangleoverdelta=zeta^7;% 65
triangle=delta*triangleoverdelta;
```

2. Heat Transfer Coefficient

```
hg=cp*rhoU*Ch;
```

3. Heat Flux

```
qw=hg*(Tas-Ts);
```

C. Equations for Iterative Simultaneous Solution of Momentum and Energy Equations

1. Momentum Equation

```
dthetadz=(Cf*dsdz/2)-theta*( ( (2-(M^2)+(delstar/theta))/(M*(1+ ( ((gamma-1)/2)*(M^2) ) )) )*dMdz +
(dAsdz/As)); % 25
```

2. Energy Equation

```
dphidz=(Ch*(Tas-Ts)*dsdz/(To-Ts))-phi*( ( (1-(M^2))/(M*(1+ ( ((gamma-1)/2)*(M^2) ) )) )*dMdz +
(dAsdz/As)-(dTsdz/(To-Ts))); % 30
% output=[dthetadz;dphidz;hg;qw;delta;triangle;delstar;Cf;Ch;zeta];
dx=[dthetadz;dphidz];
```

```
end
```

Integral 1

```
function I = I1(b,c,zeta)
%syms s
%I = double(int(s^7*(1-s)/(1+b/zeta*s-c*s^2),0,1));
s = 0:1/100:1;
I = trapz(s,s.^7.*(1-s)./(1+b/zeta.*s-c*s.^2));
end
```

Integral 2

```
function I = I2(b,c,zeta)
%syms s
%I = double(int(s^7/(1+b/zeta*s-c*s^2),0,1));
s = 0:1/100:1;
I = trapz(s,s.^7./(1+b/zeta.*s-c*s.^2));
end
```

Integral 3

```
function I = I3(b,c,zeta)
%syms s
%I = double(int(s^6*(1-s)/(1+b/zeta*s-c),1,zeta));
s = 1:(zeta-1)/100:zeta;
I = trapz(s,s.^6./(1+b/zeta.*s-c));
end
```

Integral 4

```
function I = I4(b,c,zeta)
%syms s
%I = double(int(s^7*(1-s)/(1+b/zeta*s-c*s^2),0,zeta));
s = 0:zeta/100:zeta;
I = trapz(s,s.^7.*(1-s)./(1+b/zeta.*s-c*s.^2));
end
```

Integral 5

```
function I = I5(b,c,zeta)
%syms s
%I = double(int(s^7*(1-s)/(1+b-c*s^2),zeta,1));
s = zeta:(1-zeta)/100:1;
I = trapz(s,s.^7.*(1-s)./(1+b-c*s.^2));
end
```

Integral 6

```
function I = I6(b,c,zeta)
%syms s
%I = double(int(s^7/(1+b/zeta*s-c*s^2),0,zeta));
s = 0:zeta/100:zeta;
I = trapz(s,s.^7./(1+b/zeta.*s-c*s.^2));
end
```

Integral 7

```
function I = I7(b,c,zeta)
%syms s
%I = double(int(s^7/(1+b-c*s^2),zeta,1));
s = zeta:(1-zeta)/100:1;
I = trapz(s,s.^7./(1+b-c*s.^2));
end
```

Integral 1'

```
function I = I1p(b,c,zeta)
%syms s
%I = double(int(s^7*(1-s)/(1+b*s-c*zeta^2*s^2),0,1));
s = 0:1/100:1;
I = trapz(s,s.^7.*(1-s)./(1+b.*s-c*(zeta^2)*s.^2));
end
```

Integral 2'

```
function I = I2p(b,c,zeta)
%syms s
%I = double(int(s^7*(1-s)/(1+b*s-c*zeta^2*s^2),0,1/zeta));
s = 0:1/zeta/100:1/zeta;
I = trapz(s,s.^7.*(1-s)./(1+b.*s-c*zeta^2*s.^2));
end
```

Integral 3'

```
function I = I3p(b,c,zeta)
%syms s
%I = double(int(s^6*(1-s)/(1+b*s-c),1/zeta,1));
s = 1/zeta:(1-1/zeta)/100:1;
I = trapz(s,s.^6.*(1-s)./(1+b.*s-c));
end
```

Bartz Zeta Case I Solver, Zeta >=1, Trapezoidal

This version of the solver uses the trapezoidal rule to integrate stuff.

```
function out = zg1(guess)
global phi theta b c
zeta=guess;
```

```
out = -zeta+( (phi*I1(b,c,zeta))/(theta*(I2p(b,c,zeta)+(I3p(b,c,zeta)/zeta))))^(1/8); % 83

end
% Skin Friction Dealio
function Cf = C_f(R,z)
global m a options2
Cfb = T1i(R);
if(Cfb*R>64.8)
    Cfb = fminbnd(@(x) minimize40(x,R),0,0.00219,options2);
end
if(Cfb*R<=2.51)
    Cfb = solve41(R);
end
Cf  = Cfb/((0.5*(a+1))^((3-m)/4));
end
function result = T1i(R)
global T1
result = interp1(T1(1,:)./T1(2,:),T1(2,:),R,'cubic');
end
function result = solve41(R)
    result = (0.009896/(R^0.562))^(1/1.562);
end
```

Published with MATLAB® R2013a

Bartz Startz

This function calculates the stagnation point solution for the Bartz integrals for use in determining the field of film coefficients that develop over the surface of the structural webbing when placed in cross flow. It uses a stagnation point solution to determine the initial h-values, then determines the Z-value at which the boundary layer has developed to the point where it is logical to abandon the stagnation solution, and feeds the initial values of the thermal and momentum boundary layer thicknesses to the Bartz solver.

Contents

Function

```
function [zinitial, theta0, phi0, hstart,U,nu] = BartzStartzFinal(rhoU)
global mu0 Pr cp rho
rho_lbm=rho*1000*32.174049/14.593903/(3.28084^3); % lbm/ft^3
rho_lbf=rho_lbm/32.174049; % lbf-s^2/ft^4;
rho_mix=rho_lbm/144; % lbm/ft-in^2
U=rhoU/rho_mix; % ft/s

k=cp*mu0*32.174/Pr/12;
D=.01/12; % ft
z=0:0.0001:1; %ft
% Incompressible
B=4*U/D; % ft/s
del_stag=2.4*sqrt(mu0/rho_lbf/B); % ft
nu=mu0/rho_lbf; % ft^2/s
Rez=z*rhoU*(12/32.174)/mu0; %no dim
del_bl=0.16.*z./(Rez.^(1/7)); % ft
del_bl(1)=0;
Cf=0.027./(Rez.^(1/7));
lambda=sqrt(2./Cf);
theta=((3.54./lambda)-(22.21./(lambda.^2))).*del_bl;
theta=ones(1,length(z))*1e-3;
theta(1)=0;

zinitial=interp1(del_bl,z,del_stag);
theta0=interp1(z,theta,zinitial);
phi0=theta0*1.1;

ReD=D*U/nu;
NuD=1.15*(ReD^(1/2))*(Pr^(1/3));
zres=50; % number of points
zinitial=linspace(0,12*zinitial,zres);
hstart=NuD*k/(D*12)*ones(1,length(zinitial));
hstart(1);
end
```

Published with MATLAB® R2013a

Bartz Mesher

This program produces a 3-D mesh of the Spider using a similar scheme to the BartzGeometry code. It can easily be recast to display the 3-dimensional variation of calculated film coefficients.

Contents

Function

```
clc
clear all
close all
r_inner=0.75/2;
r_outer=3.6/2;
dels=0.05;
delz=0.05;
maxz=1;
n=3;
z=[0:delz:maxz]';
tt=[AirfoilProfile(); 999*maxz 0];
alpha=2*pi/n;
% Initial x limits
xstart=r_inner;
% Inner and outer circumferences and angular resolutions
circum_outer=alpha*r_outer;
dtheta_outer=dels/r_outer;
circum_inner=alpha*r_inner;
dtheta_inner=dels/r_inner;
% define limits for for loops
lim1=floor((r_outer-r_inner)/dels);
lim2=lim1+floor(circum_outer/dels);
lim3=lim2+lim1;
lim4=lim3+floor(circum_inner/dels);
x=zeros(length(z),lim4);
y=zeros(length(z),lim4);
v=zeros(length(z),lim4);
for j=1:length(z)
    t=interp1(tt(:,1),tt(:,2),z(j));
    v(j,:)=z(j);
    for i=1:lim1
        x(j,i)=xstart+(i-1)*dels;
        y(j,i)=t;
    end
    for i=lim1+1:lim2+1
        x(j,i)=r_outer*cos((i-lim1-1)*dtheta_outer);
        y(j,i)=r_outer*sin((i-lim1-1)*dtheta_outer);
    end
    for i=lim2+2:lim3+1
        x(j,i)=((r_outer-(i-lim2-1)*dels)*cos(alpha))+t*cos(alpha-.5*pi);
        y(j,i)=((r_outer-(i-lim2-1)*dels)*sin(alpha))+t*sin(alpha-.5*pi);
    end
    for i=lim3+2:lim4
        x(j,i)=r_inner*cos(alpha-(i-lim3-1)*dtheta_inner);
        y(j,i)=r_inner*sin(alpha-(i-lim3-1)*dtheta_inner);
    end
    x(j,lim4)=xstart;
```

```
    y(j,lim4)=0;
end
g=mesh(x,y,v);
```

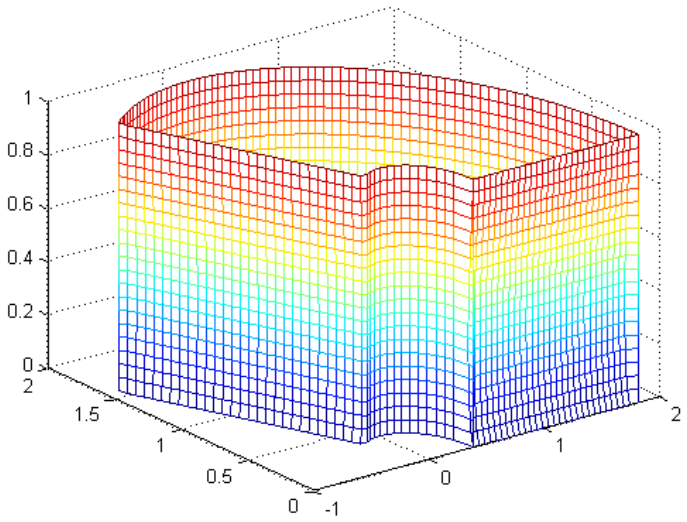

Published with MATLAB® R2013a

Contents

WALZING Function

This function uses ODE45 to solve the compressible-turbulent boundary layer using the Karman-based method of Walz(1969) in order to determine the necessary length of flat plate preceding a nozzle for the momentum and enthalpy boundary layer thicknesses to develop to a desired point. It is also desired to compare this to the results given by the Van Driest II flat plate theory (1956).

```
function Walzing
clc
clear all
close all
global Ue gamma Ma dUedx Te Tw Taw m rhoU n muw
n=0.268;
% Mach number stuff:
m=0.65; % Temperature dependence of viscosity
gamma=1.2;
delM=0.001;
rs=0.885;
Astar=pi*rs^2;
AA1=zeros(995,1);
MM1=zeros(995,1);
rb=[2.500 2.486 2.443 2.367 2.266 2.150 2.035 1.919 1.803 1.688 1.572...
    1.456 1.341 1.225 1.104 1.010 0.945 0.904 0.886 0.885 0.886 0.891...
    0.917 0.965 1.045 1.180 1.314 1.448 1.582 1.716 1.850];
zb=[0.0 0.2 0.4 0.6 0.8 1.0 1.2 1.4 1.6 1.8 2.0 2.2 2.4 2.6 2.8 3.0 3.2...
    3.4 3.6 3.66 3.7 3.8 4.0 4.2 4.5 5.0 5.5 6.0 6.5 7.0 7.5];
for i=1:1/delM-5
    MM1(i)=(i+5)*delM;
    AA1(i) = ((1/MM1(i))*(((1+ ((gamma-1)/2)*(MM1(i)^2))/((gamma+1)/2))^((gamma+1)/(2*(gamma-1)))));
end
Ma=interp1(AA1,MM1,pi*rb(1)^2/Astar);
% Specific heat at constant pressure
cp=0.567; % Btu/lbm-degR
cv=cp/gamma; % Btu/lbm-degR
R1=cp-cv; % Btu/lbm-degR
% BTU/lbm-->1 BTU=778.3 ft-lbf
% 1 lbf=1slug*ft/s^2
% 1 slug = 32.174049 lbm
R=R1*778.3;% ft-lbf
R=R*32.174049; % ft^2/s^2-degR
To=4500; % degR, stagnation temp
Te=To; % Same thing, different variable
po=300; % psia
% Speed of sound:
c=sqrt(R*Te*gamma);
Ue=Ma*c;
dUedx=0;
Tw=1125;
Taw=Te*((1+0.89*((gamma-1)/2)*(Ma^2))/(1+((gamma-1)/2)*(Ma^2)));
rhoU=((32.174/778.2)^(1/2))*gamma*po*Ma...
    /( sqrt(cp*To*(gamma-1))*...
    ( (1+(((gamma-1)/2)*(Ma^2)))^((gamma+1)/(2*(gamma-1))) ) );
rho=rhoU/(Ue/12); % lbm/sec-in^2*(sec/in)=lbm/in^3
```

```
mue=1.3e-6;
muw=mue*((Tw/Te)^m);
dUedx=-.1;
options=odeset('RelTol',1e-9);
[x,out]=ode45(@Walz45,[0.01 1],[0.01 1.55]);
% plot(x,out(:,1),x,out(:,2))
assignin('base','out',out);
% Plot Data if Desired
% plot(x,out(:,1),x,out(:,2))
% axis([0 0.15 0 2.5])
% xlabel('X [in]')
% ylabel('\delta [in]')

end
```

ODE45 Function

```
function out = Walz45(x,in)
```

```
global Ue gamma Ma dUedx Te Tw Taw m rhoU muw n


Z=in(1);
W=in(2);
% [in(1) in(2) x]
theta=(Z/((rhoU/muw)^n))^(1/n);
```

Parameters

Heat transfer parameter

```
THETA=(Taw-Tw)/Taw-Te;
% Intermediate parameters
a=0.0394*((W-1.515)^0.7);
b=1+0.88*(gamma-1)/2*(Ma^2)*(W-THETA)*(2-W);
% H=delstar/theta, displacement thickness over momentum thickness
H=1+1.48*(2-W)+104*((2-W)^6.7);
% n is the viscosity-temperature exponent
Beta=(  (1+0.587*(gamma-1)*(Ma^2)*(1-0.75*THETA))/...
    (1+0.44*(Ma^2)*(1-THETA)*(gamma-1)))^m;
% Algebraic functions
F1=2.268+1.268*H-Ma^2;
F2=1.268*a/b;
F3=1-H+0.88*(gamma-1)*(Ma^2)*(1-THETA/W);
F4=(1/b)*(2*Beta*((rhoU*theta/muw)^0.168)-a*W);

dZdx=F2-(F1/Ue)*dUedx*Z;
dWdx=(F4/Z)-(F3/Ue)*dUedx*W;
out=[dZdx;dWdx];
```

```
end
```

Structural Webbing Heat Transfer Load Estimator

This code calculates the h coefficient using conservative numbers and Bartz's 1957 correlation, then calculates temperature and stress as a function of time using classical heat transfer methods.

Contents

Clear the playing field

```
clc
clear all
close all
```

Define Parameters

```
D=2*1.624; % inches
Di=2*.350; % inches
thickness=.125; % Spoke thickness, inches
nspokes=3; % number of spokes
C=0.026; % Dimensionless
Dstar=0.75; % inches
mu=1.3e-6;% lb/foot-s*1foot/12in
Cp=0.45; % Btu/Lbm*degreesF
Pr=0.60; % Dimensionless
Pc=300; % psiA
Cstar=4500; % ft/s
rc=3/32; %inches
Astar=0.25*pi*Dstar^2; % in^2
A=9.2; % in^2
sigma=1.2; % Dimensionless
```

Caclulate h, T, stress

```
h=((C/(Dstar^0.2))*((mu^0.2)*Cp/(Pr^0.6))*((Pc/Cstar)^0.8)*((Dstar/rc)^0.1))*((Astar/A)^0.9)*sigma %
 [BTU/s-in^2-°R]
```

```
h =

      1.23302218178841e-05
```

For Titanium Carbide

```
rho=0.00046225*12*32.174; % lbm/in^3
Cp=[530 720 900 1080 1260 1440 1620 1800 1980 2160 2340 2520 2700 2880 3060
```

```
    0.135014335 0.165383303 0.180156879 0.188793114 0.194529103 0.198721798...
    0.202013840 0.204749245 0.207121522 0.209245343 0.211192378 0.213015185...
    0.214742432 0.216398009 0.217998639]'; % °R,Btu/lbm-degF
A=24.7139; % in^2
V=2.6962; % in^3
alpha=4.28e-6; % in/in-degF
E=65e6; % Psi
m=rho*V;
Tinf=4500; % °R
To=530; % °R
T(1)=To;
for i=2:6000
    t(i)=i/100;
    C_p=interp1(Cp(:,1),Cp(:,2),T(i-1));
    T(i)=Tinf-(Tinf-To)*exp(-h*A*t(i)/(m*C_p));
    stress(i)=E*alpha*(T(i)-To);
end
```

Plots

```
plot(t,T)
title('T(t)')
xlabel('Time, Seconds')
ylabel('Temperature, °R')
figure
plot(T,stress)
title('Stress(T)')
xlabel('Temperature, °R')
ylabel('Stress, Psi')
```

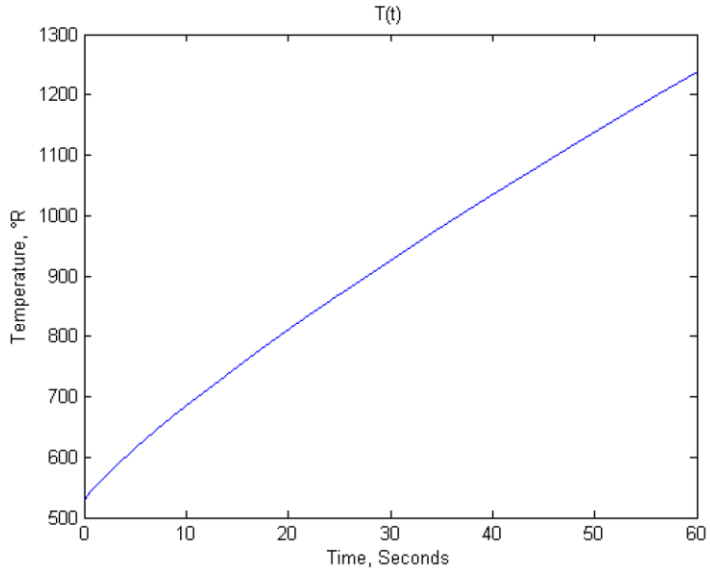

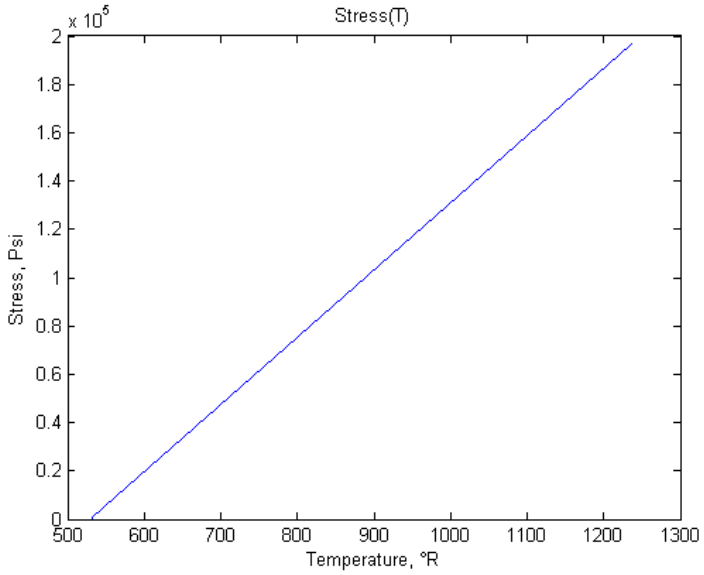

Published with MATLAB® R2013a

CEASE, CEA Scrounging Elephant

A Brock 4.30.14

This script reads CEA output files and parses the data into arrays that can be easily used for analysis with MATLAB.

Contents

How this code works

Though the CEAOUT files are in wildly different formats from run to run, certain portions of the files are always output the same way. This code scans the text to find these data portions, then reads all parameters into a variety of arrays. Importing the data allows for the analyst to average data across runs for use in further analyses.

CEASE

Change folder if desired: cd HotfireData

```
clc
clear all
close all
fclose all;
% Declare variables indicating start and end of runs
startCEA=62;
endCEA=93;
for j=[startCEA+1:endCEA]-startCEA
```

```
    fclose all;
    runno(j)=j+startCEA;
    % Avoid runs that do not have CEA files
    if any(j+startCEA==[70 72 73 74 88])
        continue
        % Account for the change in capitalization between runs 79 and 80
    elseif j+startCEA <=79
        filnam=sprintf('CEAOUT-0%2i.out',j+startCEA);
    else
        filnam=sprintf('ceaout-0%2i.out',j+startCEA);
    end

    % Open the file
    fid=fopen(filnam);
```

Determine locations of relevant data

```
a=textscan(fid,'%s');
i1=find(strcmp('problem',a{:}));
i1=i1(end);
i2=find(strcmp('THEORETICAL',a{:}));
imu=find(strcmp('VISC,MILLIPOISE',a{:}));
igma=find(strcmp('GAMMAs',a{:}));
irho=find(strcmp('G/CC',a{:}));
iT=find(strcmp('T,',a{:}))+1;
iH=find(strcmp('H,',a{:}))+1;
iU=find(strcmp('U,',a{:}))+1;
iG=find(strcmp('G,',a{:}))+1;
iS=find(strcmp('S,',a{:}))+1;
iCp=find(strcmp('Cp,',a{:}))+1;
ik=find(strcmp('CONDUCTIVITY',a{:}));
iCstar=find(strcmp('CSTAR,',a{:}))+1;
iPr=find(strcmp('PRANDTL',a{:}))+1;
```

Parse Data

Viscosities, millipoise:

```
mu_chamber(j)=str2double(cell2mat(a{:}(imu+1)));
mu_throat(j)=str2double(cell2mat(a{:}(imu+2)));
% Specific Heat Ratios:
gamma_chamber(j)=str2double(cell2mat(a{:}(igma+1)));
gamma_throat(j)=str2double(cell2mat(a{:}(igma+2)));
% Densities, g/cc:
b=cell2mat(a{:}(irho+1));
rho_chamber(j)=str2double(b(1:end-2))*10^str2double(b(end-1:end));
b=cell2mat(a{:}(irho+2));
rho_throat(j)=str2double(b(1:end-2))*10^str2double(b(end-1:end));
% Temperatures, Kelvin:
T_chamber(j)=str2double(cell2mat(a{:}(iT+1)));
T_throat(j)=str2double(cell2mat(a{:}(iT+2)));
% H (enthalpy?) cal/g:
H_chamber(j)=str2double(cell2mat(a{:}(iH+1)));
H_throat(j)=str2double(cell2mat(a{:}(iH+2)));
% U (speed?) cal/g:
U_chamber(j)=str2double(cell2mat(a{:}(iU+1)));
U_throat(j)=str2double(cell2mat(a{:}(iU+2)));
% G ? Cal/g:
G_chamber(j)=str2double(cell2mat(a{:}(iG+1)));
G_throat(j)=str2double(cell2mat(a{:}(iG+2)));
% S (entropy?) Cal/g-K:
S_chamber(j)=str2double(cell2mat(a{:}(iS+1)));
S_throat(j)=str2double(cell2mat(a{:}(iS+2)));
% Specific heats with Equilibrium Reactions, Cal/g-K:
Cp_eq_chamber(j)=str2double(cell2mat(a{:}(iCp(2)+1)));
Cp_eq_throat(j)=str2double(cell2mat(a{:}(iCp(2)+2)));
% Specific heats with Frozen Reactions, Cal/g-K:
Cp_fr_chamber(j)=str2double(cell2mat(a{:}(iCp(3)+1)));
Cp_fr_throat(j)=str2double(cell2mat(a{:}(iCp(3)+2)));
% Conductivities with Equilbirum Reactions:
k_eq_chamber(j)=str2double(cell2mat(a{:}(ik(2)+1)));
k_eq_throat(j)=str2double(cell2mat(a{:}(ik(2)+2)));
% Conductivities with Frozen Reactions:
k_fr_chamber(j)=str2double(cell2mat(a{:}(ik(3)+1)));
k_fr_throat(j)=str2double(cell2mat(a{:}(ik(3)+2)));
% Specific Speed, ft/s:
```

```
    Cstar_throat=str2double(cell2mat(a{:}(iCstar+1)));
    Cstar_exit=str2double(cell2mat(a{:}(iCstar+2)));
    % Prandtl number with Equilibrium Reactions:
    Pr_eq_chamber(j)=str2double(cell2mat(a{:}(iPr(1)+1)));
    Pr_eq_throat(j)=str2double(cell2mat(a{:}(iPr(1)+2)));
    % Prandtl Number with Frozen Reactions:
    Pr_fr_chamber(j)=str2double(cell2mat(a{:}(iPr(2)+1)));
    Pr_fr_throat(j)=str2double(cell2mat(a{:}(iPr(2)+2)));
```

Parse Exit Data

Because not all runs have EXIT calculations, not all exit data is available.

```
    if find(strcmp('EXIT',a{:}))
        mu_exit(j)=str2double(cell2mat(a{:}(imu+3)));
        gamma_exit(j)=str2double(cell2mat(a{:}(igma+3)));
        b=cell2mat(a{:}(irho+3));
        rho_exit(j)=str2double(b(1:end-2))*10^str2double(b(end-1:end));
        T_exit(j)=str2double(cell2mat(a{:}(iT+3)));
        H_exit(j)=str2double(cell2mat(a{:}(iH+3)));
        U_exit(j)=str2double(cell2mat(a{:}(iU+3)));
        G_exit(j)=str2double(cell2mat(a{:}(iG+3)));
        S_exit(j)=str2double(cell2mat(a{:}(iS+3)));
        Cp_eq_exit(j)=str2double(cell2mat(a{:}(iCp(2)+3)));
        Cp_fr_exit(j)=str2double(cell2mat(a{:}(iCp(3)+3)));
        k_eq_exit(j)=str2double(cell2mat(a{:}(ik(2)+3)));
        k_fr_exit(j)=str2double(cell2mat(a{:}(ik(3)+3)));
        Pr_eq_exit(j)=str2double(cell2mat(a{:}(iPr(1)+3)));
        Pr_fr_exit(j)=str2double(cell2mat(a{:}(iPr(2)+3)));
    end
```

```
end
```

Data processing:

To get the mean of data and neglect all dataless entries: mean(Pr_eq_chamber(Pr_eq_chamber~=0)) Examine Variance in values if desired plot(Pr_eq_chamber(Pr_eq_chamber~=0)) plot(100*(Pr_fr_chamber(Pr_fr_chamber~=0)-mean(Pr_fr_chamber(Pr_fr_chamber~=0)))/mean(Pr_fr_chamber(Pr_fr_chamber~=0))) plot(T_chamber)

Unit Conversions/averaging

```
mu_lbf = 100*mu_chamber/(1e6*4.448221615*(3.28084^2));
mu_mean=mean(mu_lbf(mu_lbf~=0));
rho_mean=mean(rho_chamber(rho_chamber~=0));
Pr_eq_mean=mean(Pr_eq_chamber(Pr_eq_chamber~=0));
Pr_fr_mean=mean(Pr_fr_chamber(Pr_fr_chamber~=0));
k_eq_mean=mean(k_eq_chamber(k_eq_chamber~=0));
k_fr_mean=mean(k_fr_chamber(k_fr_chamber~=0));
k_imperial=k_fr_mean*(4.184e-3)/1055.05585/.39370087/1.8;

% Return to parent folder if required
% cd ..
```

FLUENT2ABAQUS

This program takes a field of film coefficients from FLUENT and parses the data into a .txt file for use with ABAQUS, correcting for units and mapping the data to the geometry parameterized within GeoParam, a function contained within this file.

Contents

Function

```
function FLUENT2ABAQUS
```

```
clc
clear all
close all
```

Get geometry

```
prof='Snub'; % Snub-nose Profile
n=5;
[geo,br]=GeoParam(prof,n);
% plot(geo(:,1),geo(:,2));
% axis([-.05 .2 -.4 .4])
% assignin('base','geo',geo)
```

Get FLUENT data

```
cd FLUENTResults
fid=fopen('ha1.xy');
h1=cell2mat(textscan(fid,'%f %f',373,'HeaderLines',4));
fclose all;
h1(:,2)=h1(:,2)/1055.05585/1.8/(39.3701^2);  % (1BTU/1055joule)=1btu/sec-m^2-K,*1K/1.8Rankine*1m^2/
h1(:,1)=-h1(:,1)*39.3701; % inches
I=find(h1(:,1)>=0,1);
% h should be in units of BTU/sec-in^2-R
BTUtoINLBF=9331.8; % in-lbf/BTU
h1(:,2)=h1(:,2)*BTUtoINLBF; %[(in-lbf/sec)/(in^2-°R)]
```

Map data to Geometry

```
nx=20; % spatial resolution in x-y on one edge
nz=5; % Spatial resolution in z
% Initialize mapped matrix
g=zeros(nx*nz*2,4);
for j=1:nz
```

```
    for i=1:nx*2
            g((j-1)*nx*2+i,1)=interp1(h1(:,1),h1(:,2),geo);

    end
end
```

```
end
```

GeoParam

This function produces paramaterized arrays containing the X-Y data for a particular piece of geometry. The geometry is presumably planar.

```
function [g,br]=GeoParam(in,nn)
if strcmp(in,'Snub')
    % Define SnubNose Parameters
    % Presume attached to origin on left side midpoint

    % Define Parameterization Parameters

    lim1=nn;
    lim2=lim1+nn;
    lim3=lim2+nn;
    lim4=lim3+nn;
    % br is the variable that defines the "break" point, past which the
    % fluent data will need to be flipped.
    br=lim2+1;
    geo=zeros(lim4,2);

    % Define Geometry
    for i=1:lim1
        geo(i,1)=0; % x on first leg
        geo(i,2)=(-.375/2)+.375*(i-1)/nn;    %  y on first leg
    end
    % Define half-circle of radius .0625 centered at (0.0625, .375/2)
    for i=lim1+1:lim2
        geo(i,1)=.0625+.0625*cos(pi-(pi*(i-lim1)/nn));
        geo(i,2)=.375/2+.0625*sin(pi-(pi*(i-lim1)/nn));
    end
    % Define second leg
    for i=lim2+1:lim3
        geo(i,1)=.125;
        geo(i,2)=.375/2-.375*(i-lim2)/nn;
    end
    % Define half-circle of radius 0.0625 centered at (0.0625,-.375/2)
    for i=lim3+1:lim4
        geo(i,1)=.0625-.0625*cos(pi-pi*(i-lim3)/nn);
        geo(i,2)=-.375/2-.0625*sin(pi*(i-lim3)/nn);
    end
    % Shift parameterized geometry to accomodate FLUENT:
    g=zeros(lim4+2,2);
    g(1:lim2+1,:)=flipud(geo(lim1+nn/2:lim3+nn/2,:));
    g(lim2+2:lim4+2,:)=[geo(lim3+nn/2:lim4,:);geo(1:lim1+nn/2,:)];
    % g(:,1)=[g(:,1);geo(

end
end
```

Fluent 3D Interpolator

A Brock, 11.4.2014

This function takes in three separate FLUENT .xy data files each containing a single coordinate tied to a surface film coefficient value and uses that to create a cohesive film coefficient map.

Contents

Empty the Arena

```
clc
clear all
close all
```

Parse data

```
a=csvread('Sx1.xy',4,0);
a=length(a)+1;
b=dlmread('Sx1.xy','\t',[4 0 a 1]);
x=b(:,2);
hx=b(:,1);
clear b
b=dlmread('SY1.xy','\t',[4 0 a 1]);
y=b(:,2);
hy=b(:,1);
clear b
b=dlmread('SZ1.xy','\t',[4 0 a 1]);
z=b(:,2);
hz=b(:,1);
clear b
h=hz;
clear hx hy hz
```

Write data

```
csvwrite('C:\Temp\Fluentfilm1.dat',[x*39.3701 y*39.3701 z*39.3701
h/1055.05585/1.8/(39.3701^2)]*9331.8)
```

Published with MATLAB® R2013a

Hotfire Data Processor

ABCDE, 12.12.14

This function processes data from a set of hotfire log files, fixes the inherent error in the ADAMVIEW timestamp scheme, then displays data for verification. This version of the code brings in data for Run 103.

Contents

Bring in data

```
clc
clear all
close all
fclose all;
```

Enter Burn Start Time

```
burnstart=334.1; % [s]
```

Parse Timestamps

```
for i =1:3
fid = fopen(sprintf('ABCD_RocketData022-%1i.log',i));
data.(sprintf('f%1i',i))=textscan(fid, '%s %f %f %f %f %f %f %f %f %f %f %f %f %f %f
%f','Headerlines',2,'Delimiter',',');
tt.(sprintf('t%1i',i))=zeros(length((data.(sprintf('f%1i',i)){1})),1);
for j = 1:length(tt.(sprintf('t%1i',i)))
    if length((data.(sprintf('f%1i',i)){1}{j})) == 11
        data.(sprintf('f%1i',i)){1}{j}=[data.(sprintf('f%1i',i)){1}{j}(1:9), '0',data.
(sprintf('f%1i',i)){1}{j}(10:end)];
    end
    seconds = str2double(data.(sprintf('f%1i',i)){1}{j}(7:end));
    minutes = str2double(data.(sprintf('f%1i',i)){1}{j}(4:5));
    if i==1
        time1(j,1) = minutes*60 + seconds - burnstart; % [s]
    elseif i==2
        time2(j,1) = minutes*60 + seconds - burnstart; % [s]
    elseif i==3
        time3(j,1) = minutes*60 + seconds - burnstart; % [s]
    end
end
fclose(fid);
end
data.f3(10:end)=[];
```

Parse Data

For this version of the code, each data channel is given its own two-column array containing time in the first column and the relevant data in the second column. Because the timestamp is different for each datafile, the only way to parse data that might belong in a single array (a set of temperatures, for example) would be to linearly interpolate to get each datapoint onto a unified timeseries, which may be undesirable. Structs may also be used to parse data, though getting values back out of structs tend to be a little bit more tedious and unwieldy.

```
t_low=max([time1(1) time2(1) time3(1)]); % [s]
t_high=min([time1(end) time2(end) time3(end)]); % [s]
dt = 20/1000; % [s] 50 ms
t=t_low:dt:t_high;
% Temperatures
T1=interp1(time2,data.f2{9},t)'; % [°F], Main N2O Supply Temp
T2=interp1(time2,data.f2{10},t)'; % [°F], Cooling N2O Supply Temp
T3=interp1(time2,data.f2{11},t)'; % [°F], Right N2O Temp
T4=interp1(time2,data.f2{12},t)'; % [°F], Left N2O Temp
T5=interp1(time2,data.f2{13},t)'; % [°F], Left Pre Chamber Temp
T6=interp1(time2,data.f2{14},t)'; % [°F], Right Pre Chamber Temp
T7=interp1(time2,data.f2{15},t)'; % [°F]
T8=interp1(time2,data.f2{16},t)'; % [°F]
T9=interp1(time1,data.f1{2},t)'; % [°F]
T10=interp1(time1,data.f1{3},t)'; % [°F]
T11=interp1(time1,data.f1{4},t)'; % [°F]
T12=interp1(time1,data.f1{5},t)'; % [°F]
T13=interp1(time1,data.f1{6},t)'; % [°F]
T14=interp1(time1,data.f1{7},t)'; % [°F]
T15=interp1(time1,data.f1{8},t)'; % [°F]
T16=interp1(time1,data.f1{9},t)'; % [°F]
T17=interp1(time3,data.f3{2},t)'; % [°F]
T18=interp1(time3,data.f3{3},t)'; % [°F]
T19=interp1(time3,data.f3{4},t)'; % [°F]
T20=interp1(time3,data.f3{5},t)'; % [°F]
T21=interp1(time3,data.f3{6},t)'; % [°F]
T22=interp1(time3,data.f3{7},t)'; % [°F]
T23=interp1(time3,data.f3{8},t)'; % [°F]
T24=interp1(time3,data.f3{9},t)'; % [°F]
T25=interp1(time1,data.f1{10},t)'; % [°F]
T26=interp1(time1,data.f1{11},t)'; % [°F]
T27=interp1(time1,data.f1{12},t)'; % [°F]
T28=interp1(time1,data.f1{13},t)'; % [°F]
T29=interp1(time1,data.f1{14},t)'; % [°F]

% Pressures
P_N2O_MAIN=interp1(time2,data.f2{2},t)';
P_UPSTREAM=interp1(time2,data.f2{3},t)';
P_PRECHAMBER=interp1(time2,data.f2{4},t)';
P_COOLING_SUPPLY=interp1(time2,data.f2{5},t)';

% Weights
w=interp1(time1,data.f1{16},t)';
```

Spider Plots

Temperatures

```
close all
figure(1)
plot(t,T7,t,T8,t,T9,t,T10,t,T11,t,T12,t,T13,t,T14,t,T15)
```

```
xlabel('Time [s]')
ylabel('Temperature [°F]')
legend('T1','T2','T3','T4','T5','T6','T7','T8','T9')
axis([-0.5 12 0 500])
title('Spider Temperatures as a function of Time')
figure
plot(t,T7,t,T8,t,T13)
xlabel('Time [s]')
ylabel('Z1 Temperature [°F]')
legend('T1','T2','T7')
axis([-0.5 8 0 500])
title('Spider Z1 Temperatures as a Function of Time')
figure
plot(t,T9,t,T10,t,T11)
xlabel('Time [s]')
ylabel('Z2 Temperature [°F]')
legend('T3','T4','T5')
axis([-0.5 8 0 500])
title('Spider Z2 Temperatures as a Function of Time')
figure
plot(t,T12,t,T14,t,T15)
xlabel('Time [s]')
ylabel('Z3 Temperature [°F]')
legend('T6','T8','T9')
axis([-0.5 8 0 500])
title('Spider Z3 Temperatures as a Function of Time')
figure
plot(t,P_PRECHAMBER)
xlabel('Time [s]')
ylabel('Pressure [psig]')
axis([-0.5 8 0 200])
title('Prechamber Pressure as a Function of Time')
```

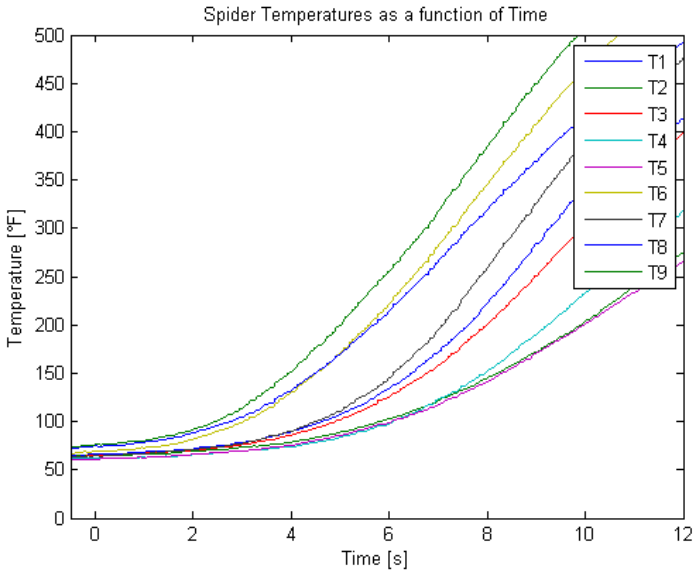

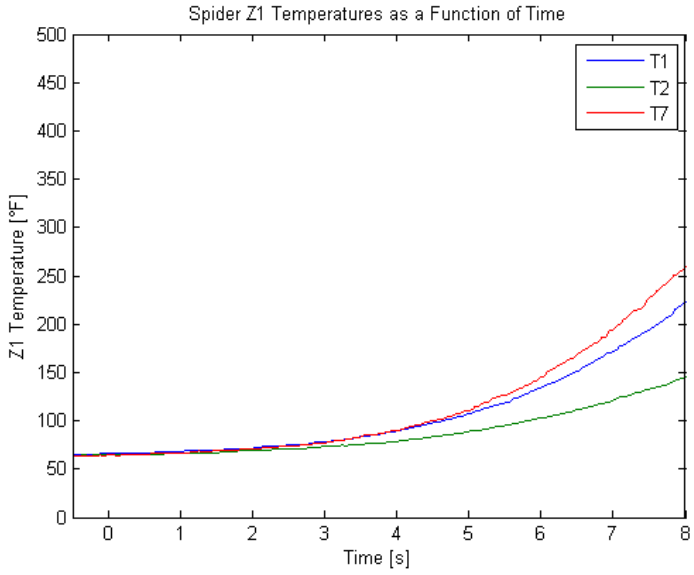
Spider Z1 Temperatures as a Function of Time
T1
T2
T7
Z1 Temperature [°F]
Time [s]
0
50
100
150
200
250
300
350
400
450
500
0
1
2
3
4
5
6
7
8

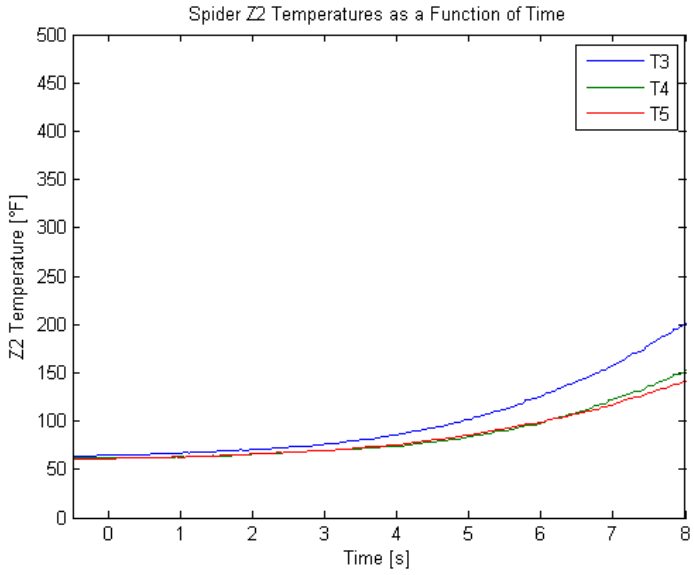
Spider Z2 Temperatures as a Function of Time
T3
T4
T5
Z2 Temperature [°F]
Time [s]
0
50
100
150
200
250
300
350
400
450
500
0
1
2
3
4
5
6
7
8

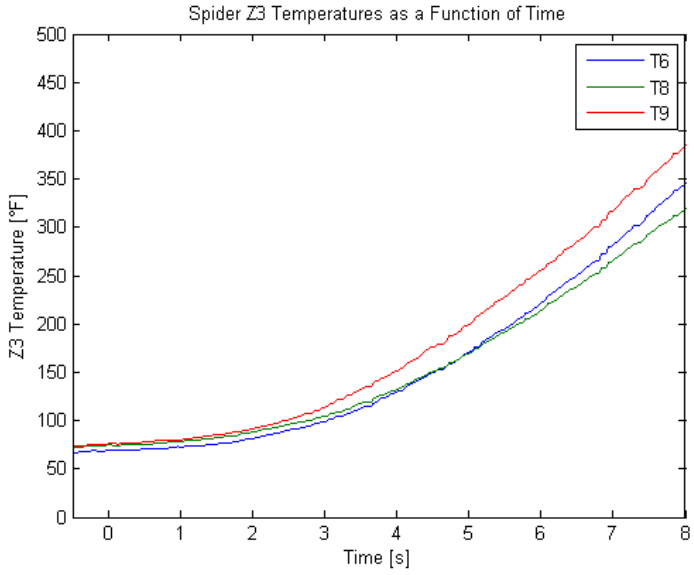

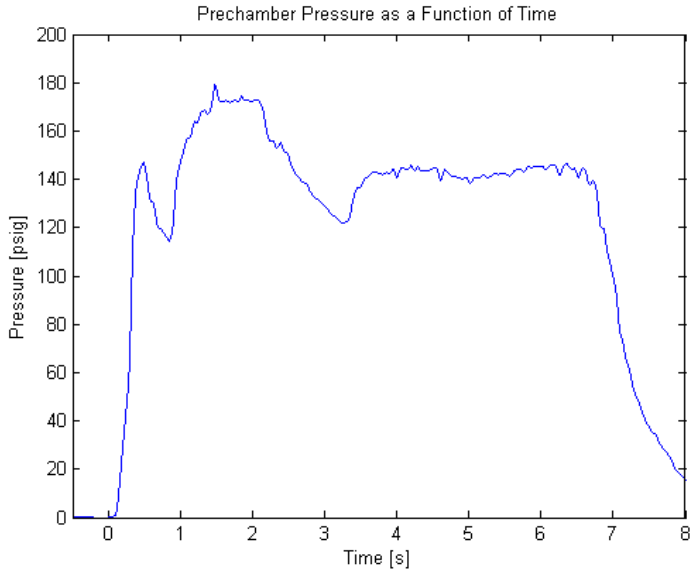

Published with MATLAB® R2013a

Parametric Study: Increase of Radius for Snub-Nose spider

This code summarizes the results of the Parametric Study performed in FLUENT to examine the variation of heat flux and film coefficients with spider geometry. The case mirrors the data presented for Run 91 using HTPB, with all numbers used in FLUENT pulled from NASA/CEA. The FLUENT files are available in the SnubPar# files.

Contents

Clearance

```
clc
clear all
close all
```

Data

```
r=[0.0625 0.125 0.25 0.375]; % [in], Nose Radius
Q=[3.68e5 5.04e5 7.07e5 9.23e5]/3.28/4; % [BTU/h], Calculated Heat Transfer rate to a 3-inch section
h=[1.35e3 1e3 .8e3 .75e3]; % [BTU/h-ft^2-R], Calculated Film Coeffecient
L=[0.375 0.5 0.5 0.5]; % [in], Exposed Length
A=pi*r+L; % [in], Cross Sectional Exposed Surface Area
V=pi.*r.^2+2.*(L.*r); % [in^2], Cross Sectional Volume
```

Plots

```
plot(r,Q)
title('Figure 1: Variation in Heat Flux with Radius.')
xlabel('Radius [in]')
ylabel('Total Heat Flux [BTU/h]')
figure
plot(r,h)
title('Figure 2: Variation in Max Film Coefficient with Radius.')
xlabel('Radius [in]')
ylabel('Max Film Coefficient [BTU/h-ft^2-R]')
figure
plot(A,Q)
title('Figure 3: Variation in Heat Flux with Surface Area.')
xlabel('Cross Section Surface Area [in]')
ylabel('Total Heat Transfer [BTU/h]')
figure
plot(V,Q)
title('Figure 4: Variation in Heat Flux with Volume.')
xlabel('Cross Sectional Volume [in^2]')
ylabel('Total Heat Transfer [BTU/h]')
```

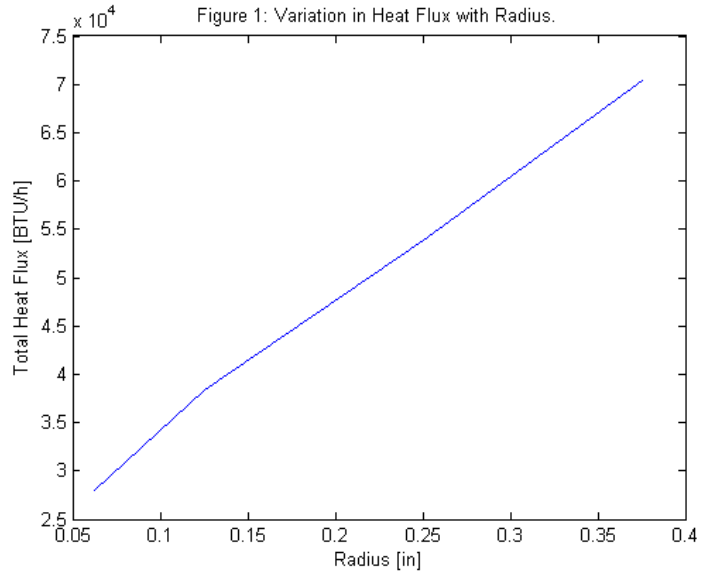

Figure 1: Variation in Heat Flux with Radius.

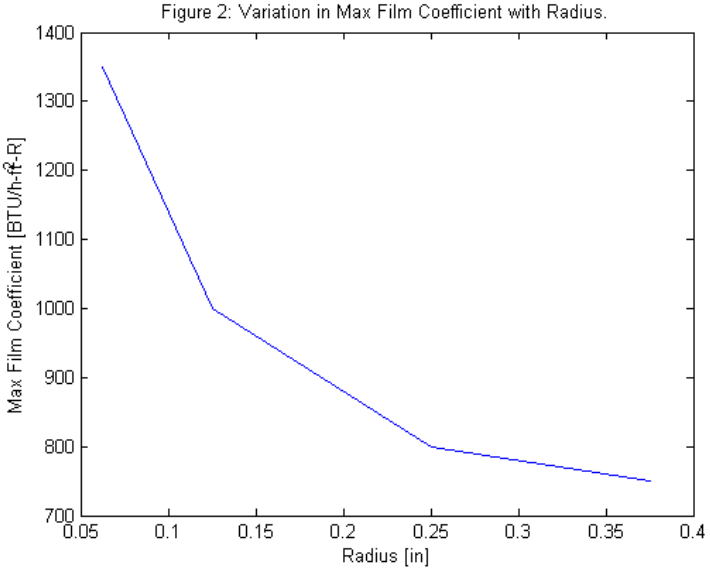

Figure 2: Variation in Max Film Coefficient with Radius.

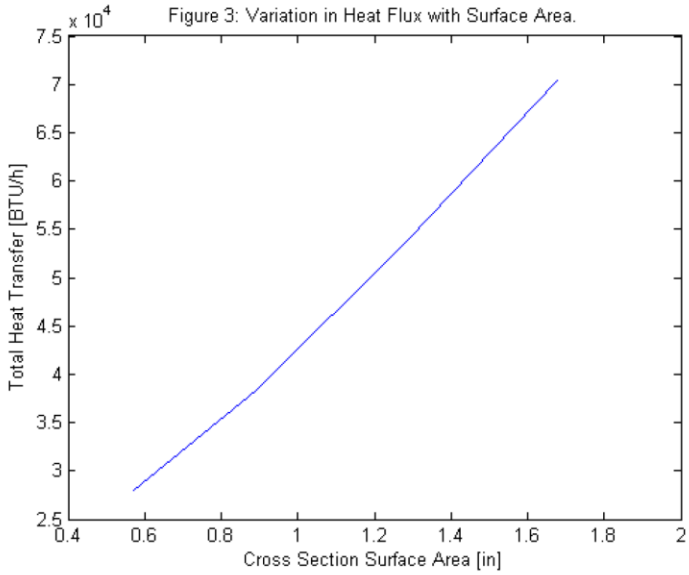

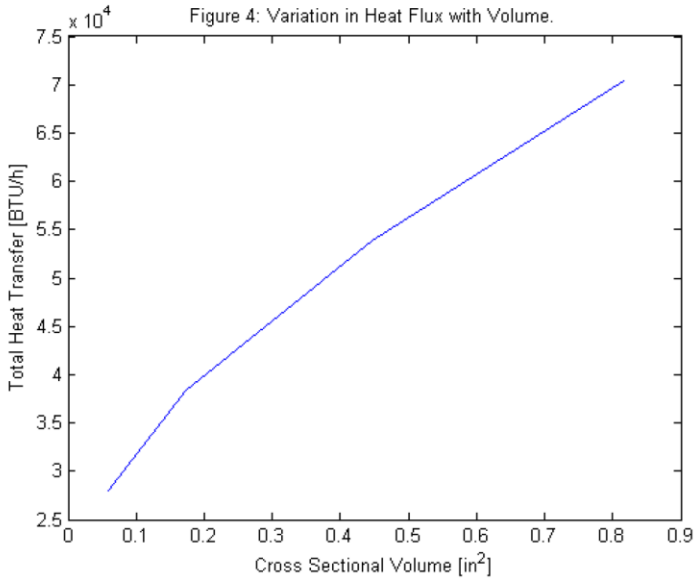

Slopes:

The values calculated here are the coefficients of best-fit polynomial lines; linear for the first three, and parabolic for the last.

```
P1=polyfit(r,Q,1)
```

```
P2=polyfit(A,Q,1)
P3=polyfit(V,Q,1)
P4=polyfit(r,h,2)
y1=@(x) P1(1)*x+P1(2);
y2=@(x) P2(1)*x+P2(2);
y3=@(x) P3(1)*x+P3(2);
y4=@(x) P4(1).*x.^3+P4(2).*x.^2+P4(3).*x+P4(4);
x1=min(r):0.001:max(r);
x2=min(A):0.001:max(A);
x3=min(V):0.001:max(V);
% plot(x2,y2(x2),A,Q)
% plot(x3,y3(x3),V,Q)
% plot(x1,y4(x1),r,h)
```

```
P1 =

   1.0e+05 *

    1.3315    0.2063


P2 =

   1.0e+04 *

    3.8440    0.5126


P3 =

   1.0e+04 *

    5.4409    2.7321


P4 =

   1.0e+03 *

    9.5357   -5.9548    1.6538
```

Published with MATLAB® R2013a

Abaqus Material Library MATLAB file

This file contains material data for use in the fully coupled thermomechanical finite element analysis of the structural webbing for the hybrid aerospike rocket motor. It takes the raw data (likely in SI units) and converts it to the appropriate consistent ABAQUS units via several acommpanying functions. Later iterations of this function will enable the user to input a property with given units and the function will produce a set of target units.

Contents

Material information required:

```
% Young's Modulus [psi]
% Poisson's ratio [no dim]
% Mass Density [Lbf-s^2/in^4]
% Thermal Conductivity [(in-lbf/sec)/(in-°R)]
% Film Coefficient [(in-lbf/sec)/(in^2-°R)]
% Specific heat capacity (Presumably C_p) [in-lbf/(lbf-sec^2/in-°R)
% Heat flux [in-lbf/sec]
% Coefficient of thermal expansion (in/in-°R)
```

Conversion factors

```
BTUtoINLBF=9331.8; % in-lbf/BTU
LBFtoLBMINSEC=386.4; % (lbm*in/sec^2)/lbf
LBMtoLBFINSEC=1/386.4; % (lbf-sec^2/in)/lbm
KGtoSLUG=0.0685217659; % slug/kg
JtoBTU=1/1055; % BTU/Joule
JKGKtoBTULBMR=2.389e-4; %J/kg-K to Btu/lbm-°R
CALCMSCtoBTUINHFT2R=2903; %Cal/cm-s-°C to BTU-in/h ft^2 °F
```

Material Database

Steel

Elasticity

```
E=31e6; % psi
% Poisson's ratio
nu=0.333; % no dim
% Coefficient of Thermal Expansions
alpha=9.7e-6; % in/in-°R
% Thermal Conductivity
k=105; % BTU-in/hr-ft^2-°F
k=k*BTUtoINLBF; % in^2-lbf/hr-ft^2-°R
k=k*(1/144)/3600; % (in-lbf/sec)/in-°R
% Specific heat capacity
```

```
C_p=0.114; % BTU/lb-°F
C_p=C_p*BTUtoINLBF; % in-lbf/lb-°R
C_p=C_p/LBMtoLBFINSEC; % in-lbf/(lbf-sec^2/in-°R)
% Mass density
rho=densitycon(7.85*1e6/1000);
% Film Coefficient
% h=1.3846e-4; % BTU/in^2-sec°R
h=0.0020; % BTU/in^2-sec°R
h=h*BTUtoINLBF;% (in-lbf/sec)/(in^2-°R)
```

Zirconium Carbide

Titanium Carbide

```
E=65e6; % psi
nu=0.185;
rho=densitycon(4.94*1e6/1000); %From g/cc to kg/m^3 to lbf-s^2/in^4
alpha=4.28e-6;
C_p = 565.16; % J/kg-K
T_cp=[300       33.86   565.15
    400   41.47 692.27
    500 45.18   754.11
    600 47.34   790.26
    700 48.78   814.27
    800 49.83   831.82
    900 50.66   845.60
    1000        51.35   857.05
    1100        51.94   866.98
    1200        52.47   875.87
    1300        52.96   884.02
    1400        53.42   891.65
    1500        53.85   898.88
    1600        54.27   905.81
    1700        54.67   912.51
    1800        55.06   919.03]; % Temperature dependent C_p
% Kelvin to Rankine
format long g
T_cp(:,1)*9/5;
T_cp(:,3)*JKGKtoBTULBMR*BTUtoINLBF/LBMtoLBFINSEC;
k=[.5*(.041+.074); .0135]*CALCMSCtoBTUINHFT2R;%cal/cm-sec-K to BTUstuff
k=[k*BTUtoINLBF/3600/144;
    530;
    (1000+273.15)*9/5];
% h=0.0020; % BTU/in^2-sec°R
h=1300; % BTU/ft^2-hr°R
h=600;
h=h/3600/144; % 1 hr/3600s 1ft^2/144in^2-> BTU/in^2-sec-R
h=h*BTUtoINLBF;% (in-lbf/sec)/(in^2-°R)
```

Published with MATLAB® R2013a

Thermal Contact Worksheet

A Brock, 1.2.15

This function evaluates the passive resistance network of the instrumented structural webbing and determines the effective orthotropic thermal conductivity, modified to account for the contact resistances.

Contents

Thermal Contact

```
function Thermal_Contact
```

```
clc
clear all
close all
```

Evaluate Line Contact

```
global Rcstar
% Properties:
D=1/8; % [in], cylinder diameter
w=0.7/2; % [in], half-length of cylinder
E=29e6; % [psi], 304 Elastic modulus
nu=0.3; % unitless, 304 Poisson's ratio
N=20; % [lbf], Press-Fit Load. Consider examining the effect of this, etc.
delta=(1-nu^2)/E; % [in^2/lbf], Combined Effective Elastic Modulus
Nstar=N*delta/(2*w*D); % Dimensionless Load Parameter
b=2*D*(Nstar/pi)^0.5; % [in], contact width
L=D/(2*b);
Rcstar=(log(1/Nstar)/pi)-0.7206;
```

Air and Steel Properties for Gap Resistance

```
air=dlmread('AirData.txt',' ',1,0);
T_air=air(:,1); % [K] Air Temp Data
K_air=air(:,6)*1e-3; % [W/m-K], Air Thermal Conductivity
Pr_air=air(:,8); % Prandtl Number Air
alpha=0.8; % Solid-Fluid Accomodation Coefficient
ks=10.67+(1.59e-2)*T_air; % [W/m-K], Harmonic Mean Thermal conductivity of 304 as a function of Temp
 in Kelvins. Since Kc=Kf, Ks=Ksteel.
kstar=K_air./ks; % Ratio of free-stream thermal conductivity to harmonic mean of solid thermal
conductivity.
gamma=1.4; % Dimensionless, specific heat ratio of air
Beta=2*gamma./(Pr_air.*(gamma+1));
lambda_inf=65e-9; % [m], Mean Free Path of Air at STP
T_inf=298.15; % [K], Temperature at STP
P_inf=100e3; % [Pa], Pressure at STP
lambda=lambda_inf*T_air/T_inf;
M=2.*alpha.*Beta.*lambda/(D*0.0254); % Dimensionless Fluid Property Parameter
```

Fluid Resistances:

DCM:

```
Rg1=1./((2.*kstar./L).*I1(L,M));
% HSM:
Rg2=1./((2.*kstar./L).*I2(L,M));
% PFTM:
Rg3=1./((2.*kstar./L).*I3(L,M,kstar));
% plot(T_air,Rg1,T_air,Rg2,T_air,Rg3);
```

Joint Resistances, Dimensionalized to K/W

```
R1=1./((1./Rg1)+(1./Rcstar))./(2*(w*0.0254).*ks);
R2=1./((1./Rg2)+(1./Rcstar))./(2*(w*0.0254).*ks);
R3=1./((1./Rg3)+(1./Rcstar))./(2*(w*0.0254).*ks);
% % plot(M,I1(L,M),M,I2(L,M),M,I3(L,M,kstar))
plot(T_air,R1,T_air,R2,T_air,R3);
xlabel('Temperature [K]')
ylabel('Joint Resistance K/W')
legend('DCM','HSM','PTFM')
title('Joint Resistances as a function of Temperature')
% Taking the PFTM to be the most accurate model, we find Joint R:
R=R3;
```

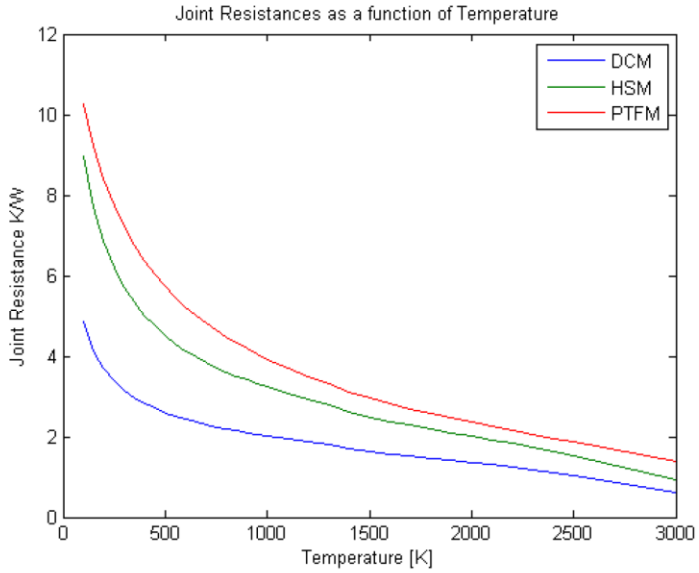

Now, finding the thermal resistances of each section of the Cartridge:.

```
%Y:
L_y1=0.1225; % [in], First Y Length, may need to reevaluate to see if this contains the round part
of the spider?;
L_y2=0.1220; % [in], Second Y Length
L_y3=0.1220; % [in], Third Y-Length
L_y_total=0.75; % [in], Total Length of Cartridge Section
A_y=2*w*.125; % [in^2], Y-Cross Sectional Area
R_y1=(L_y1*.0254)./( (A_y*(0.0254^2)).*ks); % [K/W], Thermal Resistance of First Steel Section in Y
R_y2=(L_y2*.0254)./( (A_y*(0.0254^2)).*ks); % [K/W], Thermal Resistance of First Section
R_y3=(L_y3*.0254)./( (A_y*(0.0254^2)).*ks); % [K/W], Thermal Resistance of First Section

% X:
L_x_big=0.125; % [in], Bigger X-Length
L_x_small=0.06; % [in], Smaller X-length
A_x_big=0.1250*0.7; % [in^2], Bigger X-Length Area
A_x_small=0.13*0.7; % [in^2], Smaller X-Length Area
R_x_big=(L_x_big*.0254)./( (A_x_big*(0.0254^2)).*ks); % [K/W], Thermal Resistance of Big X
R_x_small=(L_x_small*.0254)./( (A_x_small*(0.0254^2)).*ks); % [K/W], Thermal Resistance of First
Steel Section in Y
A_x=0.5844; % [in^2] Total A area at middle of probe
```

Thermal Resistance of the Probe:

```
R_cyl=(0.125*.0254)./( (A_y*(0.0254^2)).*(ks)); % [K/W], Thermal Resistance of First Steel Section
in Y
```

Finding the total resistances:

```
R_y=6*R+3*R_cyl+R_y1+R_y2+R_y3;
R_y_unmodified=(L_y_total*0.0254)./( (A_y*(0.0254^2)).*ks);
R_x=1./( (3./R_x_big)+(3./(R_x_small+R+0.5.*R_cyl)));
R_x_unmodified=(L_x_big*0.0254)./( (A_x*(0.0254^2)).*ks);
close all
% figure
% plot(T_air,R_x,T_air,R_x_unmodified);
% plot(T_air,R_x./R_x_unmodified)
% plot(T_air,R_y,T_air,R_y_unmodified)
% figure
plot(T_air,R_y./R_y_unmodified)
xlabel('T [K]')
title('Ratio of Thermal Resistances as a function of Temperature')
ylabel('Ratio of Thermal Resistances')
```

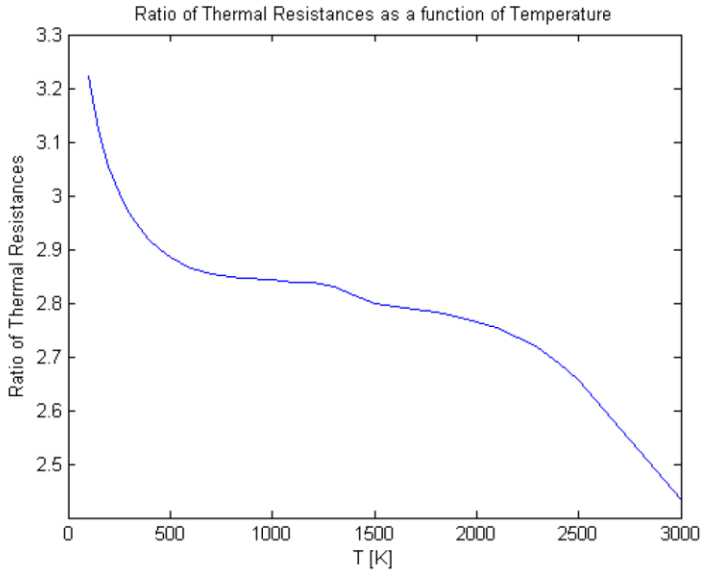

Finding the equivalent thermal capacitance:

```
% Y:
k_y=(L_y_total*0.0254)./(R_y.*(A_y.*(0.0254^2)));
figure
plot(T_air,ks,T_air,k_y)
ylabel('Thermal Conductivity [W/m-K]')
xlabel('Temperature [K]')
legend('Homogenous Solid','Including Contact Resistances')
title('Comparison of Unmodified and Modified Y-wise Thermal Conductivities')
figure
plot(T_air,ks./k_y);
xlabel('Temperature [K]')
title('Ratio of Modified to Unmodified Y-wise Thermal Conductivities as a function of Temperature')
ylabel('Ratio of Thermal Conductivities')

% X:
```

```
k_x=(L_x_big*0.0254)./(R_x.*(A_x.*(0.0254^2)));
figure
plot(T_air,ks,T_air,k_x)
ylabel('Thermal Conductivity [W/m-K]')
xlabel('Temperature [K]')
legend('Homogenous Solid','Including Contact Resistances')
title('Comparison of Unmodified and Modified X-wise Thermal Conductivities')
figure
plot(T_air,ks./k_x);
xlabel('Temperature [K]')
title('Ratio of Modified to Unmodified X-wise Thermal Conductivities as a function of Temperature')
ylabel('Ratio of Thermal Conductivities')

csvwrite('K_mod_New.csv',[T_air k_x k_y ks])
```

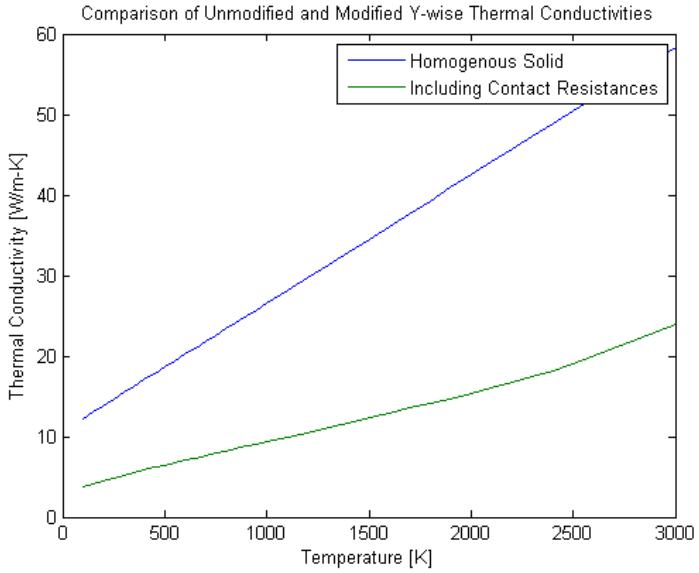

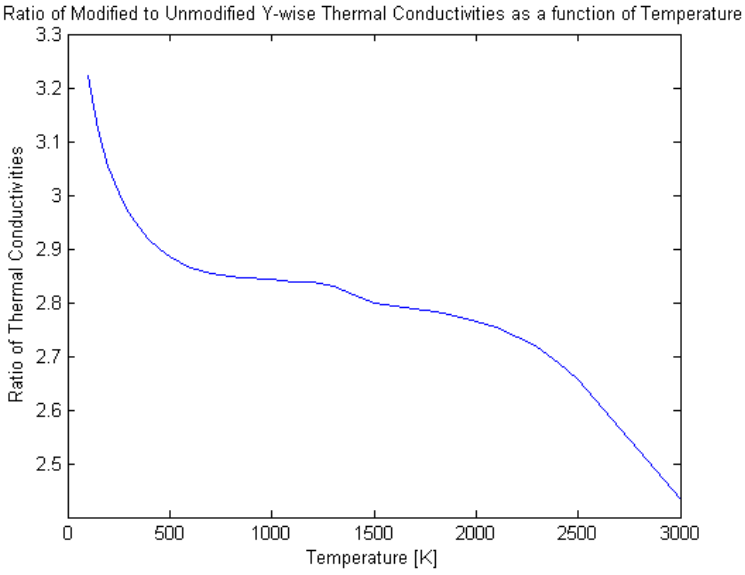
Ratio of Modified to Unmodified Y-wise Thermal Conductivities as a function of Temperature
Ratio of Thermal Conductivities
Temperature [K]
3.3
3.2
3.1
3
2.9
2.8
2.7
2.6
2.5
0
500
1000
1500
2000
2500
3000

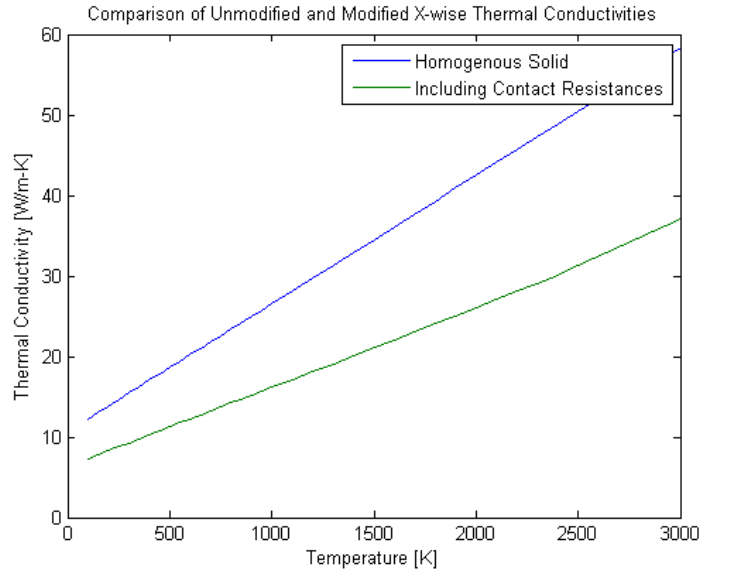
Comparison of Unmodified and Modified X-wise Thermal Conductivities
Homogenous Solid
Including Contact Resistances
Thermal Conductivity [W/m-K]
Temperature [K]
60
50
40
30
20
10
0
0
500
1000
1500
2000
2500
3000

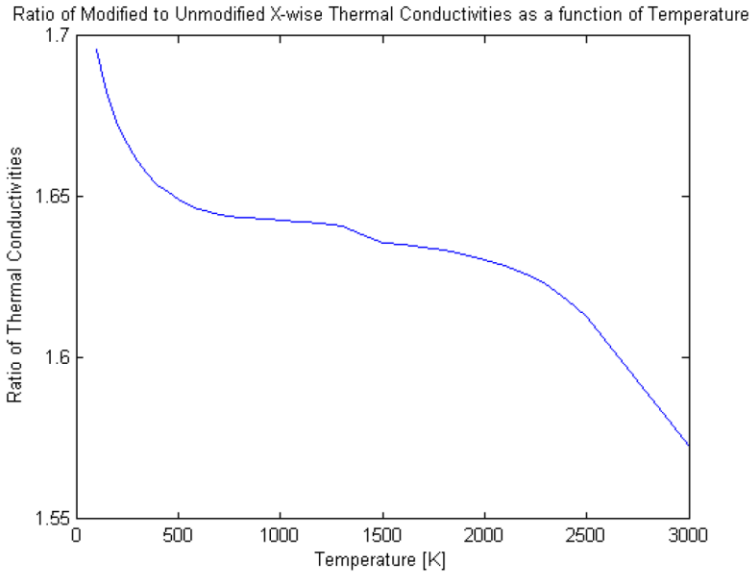


```
end
```

Decoupled Model Integral, Phi

```
function out=I1(L,M)
zeta=1:(L-1)/1000:L;
out=zeros(length(M),1);
for i=1:length(M);
    out(i)=trapz(zeta,1./(delstar(L,zeta)+M(i)));
end
% out=trapz(zeta,1./(delstar2(L,zeta)+M));
end
```

Half-Space Model Integral, Chi

```
function out=I2(L,M)
global Rcstar
zeta = 1:(L-1)/1000:L;
out=zeros(length(M),1);
for i=1:length(M)
    out(i)=trapz(zeta,2.*acosh(zeta)./(pi.*Rcstar.*(delstar(L,zeta)+M(i)))); % Need to figure out
what Rcstar really needs for its input
end
end
```

Parallel Flux-Tube Model Integral, Psi

```
function out=I3(L,M,kstar)
```

```
% Parameters:
zeta = 1:(L-1)/1000:L; % L=D/2b
delta_To=1;
delta_Tc=0.65*delta_To; % Assumed for now, may not be the case, try 0.65*Delta_to
k_s=1;
k_c=k_s;
out=zeros(length(M),1);
for i=1:length(out)
    out(i)=trapz(zeta,(delta_To/delta_Tc)./(delstar(L,zeta).*(1-
(kstar(i)*k_s/k_c))+2*kstar(i)+M(i)));
end
end
```

Gap-Thickness Function

```
function out=delstar(L,zeta)
out=sqrt(1-(1/L^2))-sqrt(1-( (zeta.^2)/(L^2) ))+(1/(2*L^2))*...
    (zeta.*sqrt((zeta.^2)-1)-((zeta.^2)-1)-acosh(zeta));
end
```

Published with MATLAB® R2013a

APPENDIX C: EXPERIMENTAL APPARATUS DRAWINGS

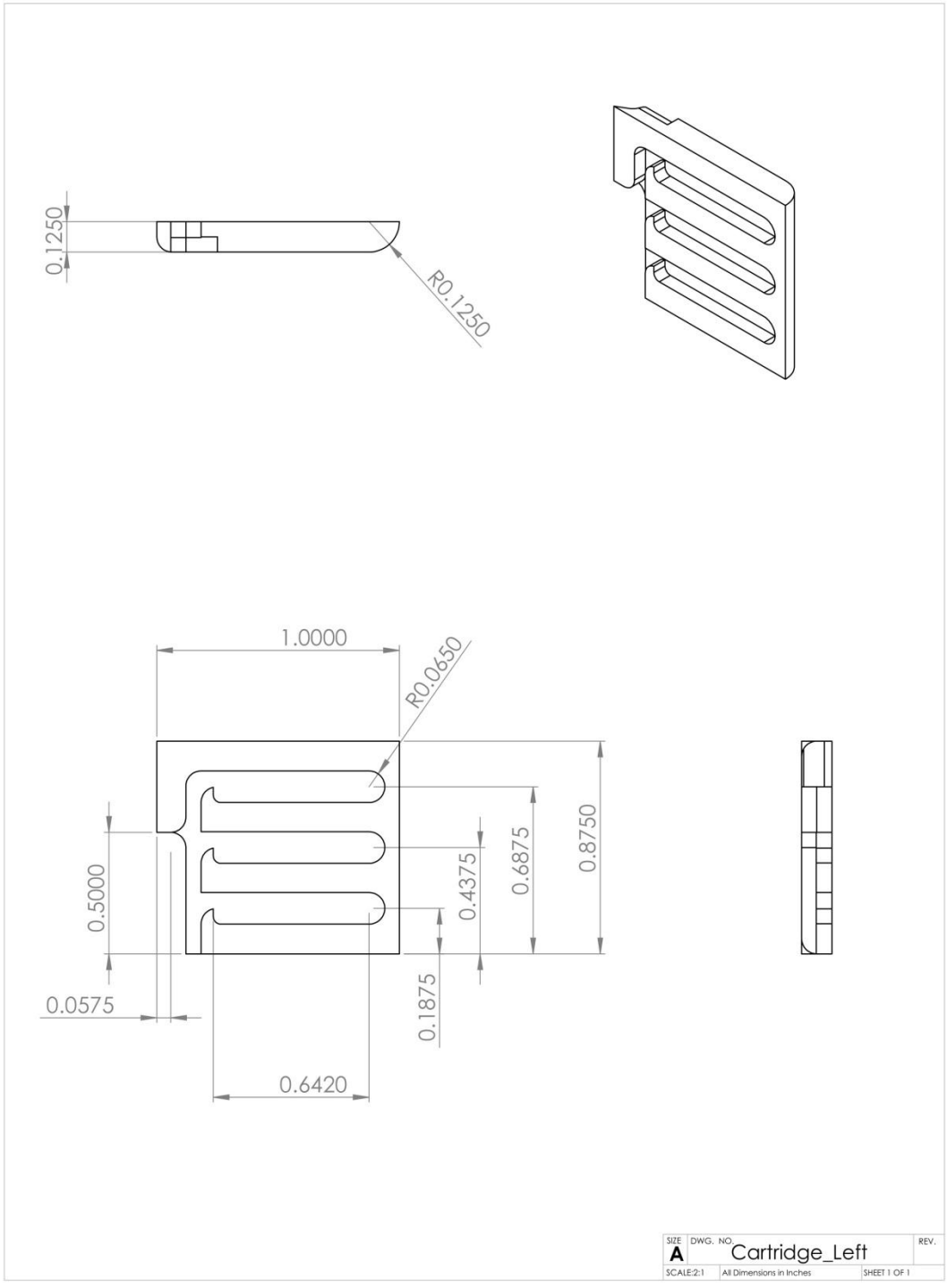
0.1250
R0.1250
1.0000
R0.0650
0.5000
0.4375
0.6875
0.8750
0.0575
0.1875
0.6420
SIZE
A
DWG. NO.
Cartridge_Left
REV.
SCALE:2:1
All Dimensions in Inches
SHEET 1 OF 1

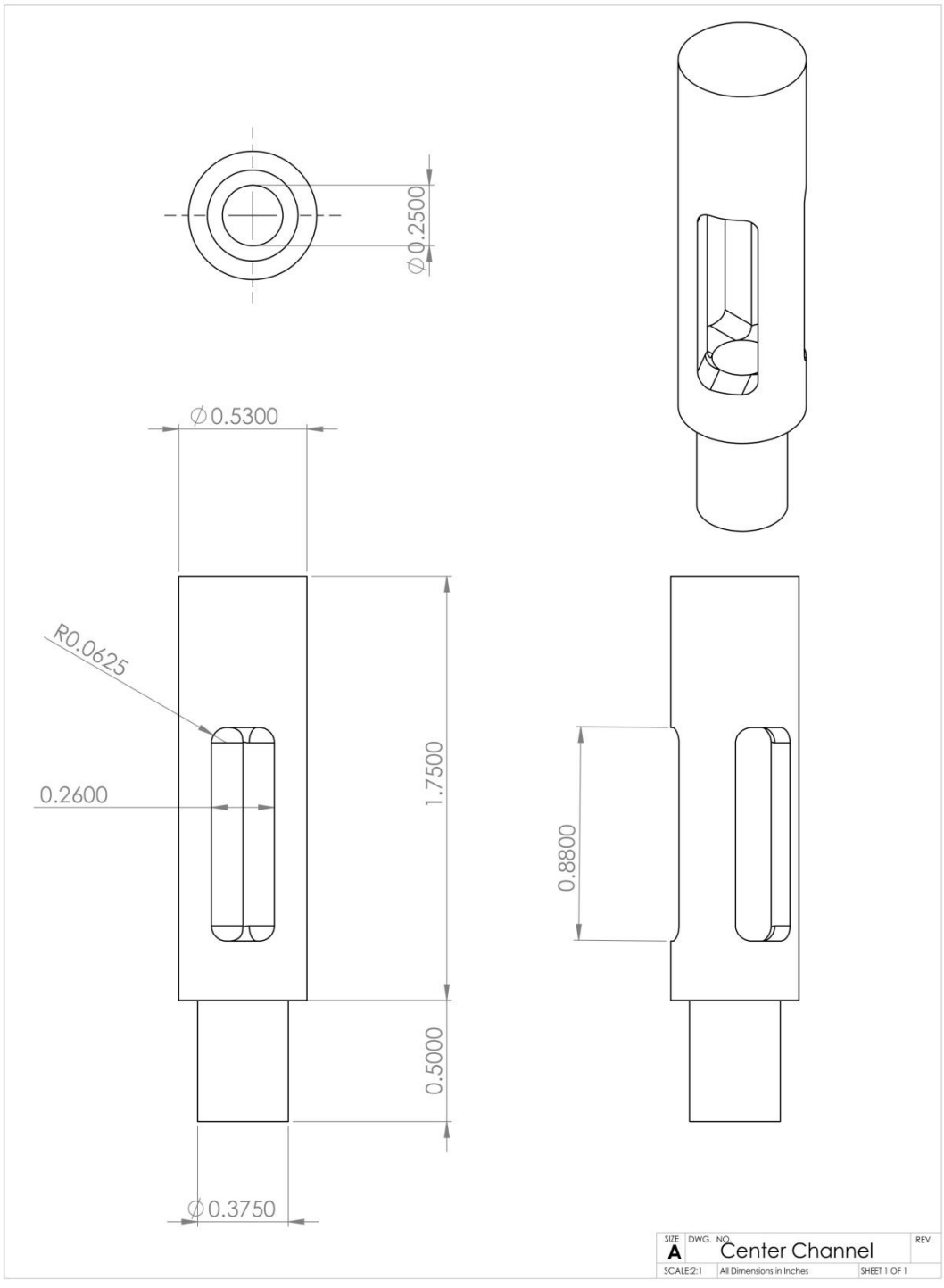
∅0.2500
∅0.5300
R0.0625
0.2600
1.7500
0.5000
∅0.3750
0.8800
SIZE A
DWG. NO.
Center Channel
REV.
SCALE:2:1
All Dimensions in Inches
SHEET 1 OF 1

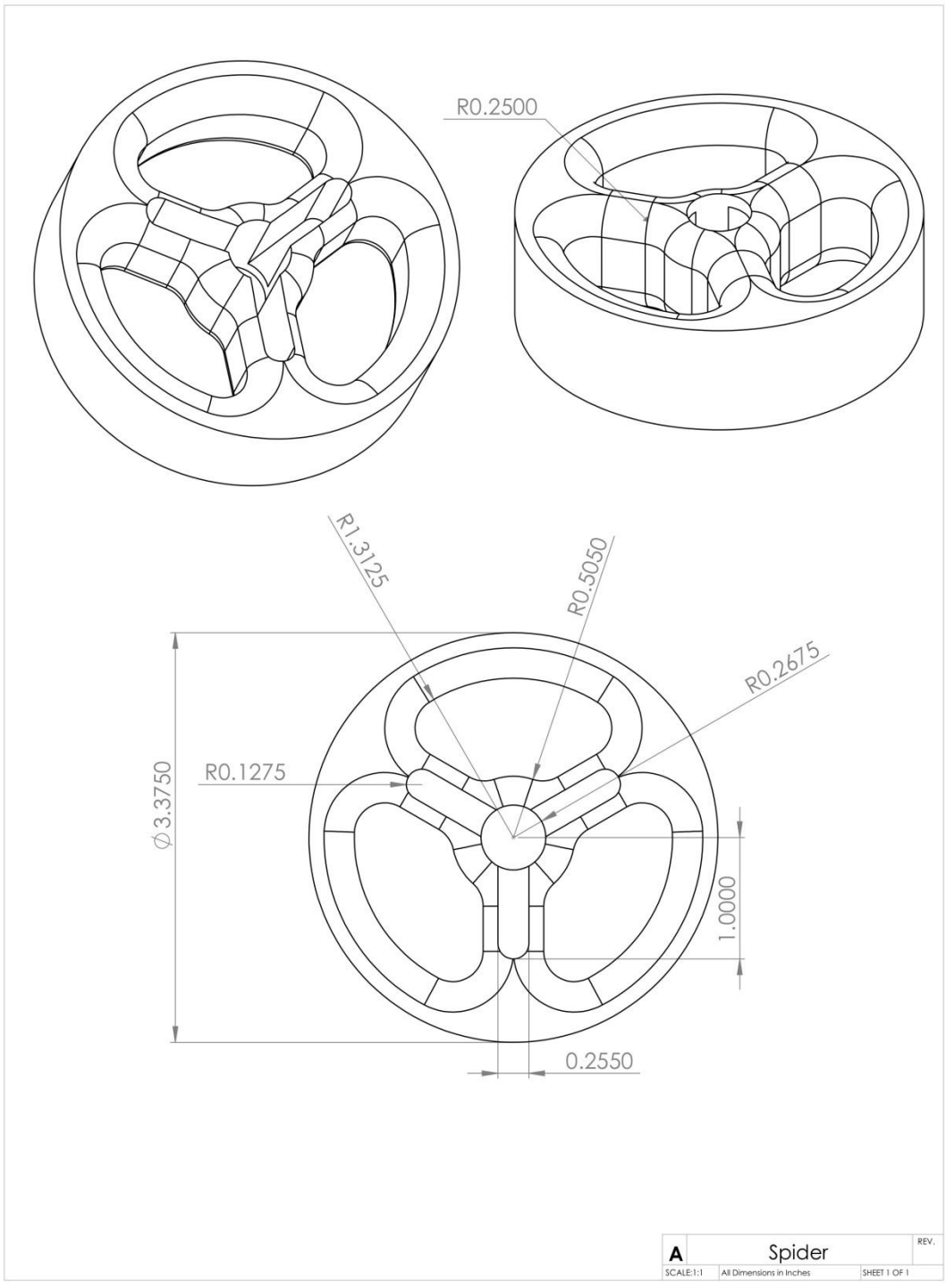
R0.2500
R1.3125
R0.5050
R0.2675
R0.1275
⌀3.3750
1.0000
0.2550
A
Spider
REV.
SCALE:1:1
All Dimensions in Inches
SHEET 1 OF 1